Evaluation ^{99m}Tc and ^{123}I Quantification using SPECT/CT

By

Modisenyane Simon Mongane

Submitted in fulfilment of the requirements in respect of the Master of Medical Science (M.Med.Sc.) degree qualification in the Department of Medical Physics in the Faculty of Health Sciences at the University of the Free State.

February 2015

Supervisor: Dr JA van Staden

Co-supervisor: Dr H du Raan

1. I, Modisenyane Simon Mongane declare that the Master research dissertation or publishable, interrelated articles that I herewith submit at the University of the Free State, is my independent work and that I have not previously submitted it for a qualification at another institution of higher education.
2. I, Modisenyane Simon Mongane hereby declare that I am aware that the copyright is vested in the University of the Free State.
3. I, Modisenyane Simon Mongane hereby declare that all royalties as regards intellectual property that was developed during the course of and/or in connection with the study at the University of the Free State, will accrue to the University.
4. I, Modisenyane Simon Mongane hereby declare that I am aware that the research may only be published with the dean's approval.

Modisenyane Simon Mongane

Acknowledgements

I would like to acknowledge the contribution my supervisor and co-supervisor Dr Johan van Staden and Dr Hanlie du Raan for their contribution during the initial stage and right through the final stages of the study and for their invaluable support.

I would like to thank Prof Rae and Prof Herbst for their contribution during the initial stage of this study.

I would also to thank my colleague Keamogetswe Ramonaheng for her continuous support throughout the duration of the study.

Lastly, I would to thank my family Ditlhare, Manda and my mother Mapitso for their support and encouragement throughout the duration of the study.

Evaluation ^{99m}Tc and ^{123}I Quantification using SPECT/CT

TABLE OF CONTENTS

Chapter 1 Introduction……...1-1

Chapter 2 Single photon emission computed tomography image quantification……..2-1

Chapter 3 Quantification of ^{99m}Tc SPECT images…….3-1

Chapter 4 Quantification of ^{123}I SPECT images……..4-1

Chapter 5 Conclusion……..5-1

Abstract

Opsomming

Glossary

Appendix

Chapter 1

Introduction to quantification in Nuclear Medicine

CHAPTER 1 1-1

1.1 NUCLEAR MEDICINE IMAGING 1-2
1.2 NUCLEAR MEDICINE QUANTIFICATION 1-3
1.3 MOTIVATION FOR THE CURRENT STUDY 1-5
1.4 THE AIM OF THE STUDY 1-5
1.5 REFERENCES 1-6

1.1 Nuclear medicine imaging

Nuclear Medicine (NM) started several decades ago. NM is a speciality studying the distribution of the administered radioactive substances in patients to assist in the diagnostic of diseases. Studying radioactive distribution within patients is accomplished by recording the emissions from the using detectors placed outside the patients. A gamma camera can be used to detect the administered radionuclide activity in the patient to obtain information with regards to the physiological processes within the patient. This gives NM physicians an opportunity to view the physiology of the internal organs for the diagnosis of certain diseases. Functional imaging is important since changes of function can occur long before any consequential changes in the morphology.

In the developmental stages of NM, the gamma camera used a single stationary detector to generate two dimensional planar images. These planar images gave intensity or counts that represented the radioactive uptake or distribution in the organs of interest. However, a problem was encountered when the organ of interest was in close proximity laterally to the other organs of high uptake or when the high uptake organs were overlying or underlying the organ of interest. Overlying or underlying organs resulted in difficulty in delineating the organ of interest in planar images without including a part of the non-target organs. The acquisition of additional planar images from different views partly solved the problem of high uptake non-target organs overlying or underlying the organ of interest.

The problem of accurately delineating organs of interest in the presence of overlying or underlying non-target organs was solved by the introduction of Single Photon Emission Computed Tomography (SPECT). During SPECT acquisition, the detector of a gamma camera is rotated around the patient to acquire planar images or projection views at a number of different angles around the patient. These projection views are reconstructed to obtain a three dimensional distribution of the radionuclide activity which is used for diagnostic purposes or planning for radionuclide therapy.

In order to reduce the imaging time gamma cameras were then manufactured with two and three detectors (these cameras are referred to as double and triple headed gamma cameras). The major advantage of double and triple headed gamma cameras is that two or three views can be acquired at the same time thus reducing the acquisition time (Cherry et al., 2012). The introduction of SPECT imaging improved contrast of NM images. The delineation of the organ of interest in close proximity to a high uptake organ depends on the resolution of the SPECT imaging system. The image resolution of a SPECT system is relatively poor compared to other imaging modalities like Positron Emission Tomography (PET) and Computed Tomography (CT).

The next developmental step in NM imaging equipment involved hybrid SPECT/CT systems. A CT scanner is used concurrently with a SPECT imaging system to reduce the problem of accurately delineating organs of interest when they are in close proximity to other organs. The higher resolution of the CT scanner enables the user to better define the boundaries of organs when the SPECT images are superimposed on the CT images. The attenuation map generated from the CT images of the patient can also be used to correct for the attenuated photons within the patient. Corrections for attenuation and scatter are necessary for accurate activity quantification in NM. However, a problem can arise when the NM uptake region is smaller than the region of anatomical information obtained from the CT image making the boundary definition of uptake region difficult.

1.2 Nuclear Medicine quantification

Conventional planar quantification was performed in NM patients where counts from conjugate views (anterior and posterior projection) were used to compute the activity in the organs. This process was complicated by the need to differentiate the activity contribution from overlapping organs, the need for background subtraction of counts from over or underlying organs, and the conjugate planar images also lacked the information in a depth dimension (Frey et al., 2012). These difficulties associated

with planar quantification can produce inaccurate quantification results (Song et al., 2010). Most of the shortcomings for planar quantification were overcome by using SPECT quantification. SPECT quantification imaging avoids the problems of organ and background overlap experienced by planar quantification imaging.

When accurate quantification is required, it is essential to minimize the image degradation which occurs as an integral part during the acquisition and reconstruction of SPECT images. During SPECT data acquisition some of the photons from uniformly distributed activity within the patient are attenuated and scattered before reaching the detectors resulting in incorrect data in the image. Therefore, the resulting reconstructed SPECT data will not represent the true activity distribution. The reconstruction algorithms such as filtered back projection (FBP) and iterative reconstruction algorithms have been used to improve image quality and quantification accuracy by applying image correction factors (attenuation, scatter, etc.). These correction factors can be applied pre- or post-reconstruction in case of FBP or incorporated as part of the iterative reconstruction method (Pereira et al., 2010). Factors that influence the quantification accuracy for both planar and SPECT studies include the sensitivity or calibration factor, photon attenuation, photon scatter, collimator-detector response and partial volume effects among others (Frey et al., 2012; Ritt et al., 2011). SPECT image complexities are realized when clinically realistic phantoms are used for quantification. The contributions of some of these effects to quantification accuracy are discussed individually in chapter 2.

SPECT/CT systems has renewed the interest in the absolute quantification because of the improvement in the corrections applied to acquired data for example the attenuation correction obtained from the CT scanner, the use of coregistered NM and CT images for delineation of the organ of interest, and the relative ease of incorporating the image degrading factors to the reconstruction algorithms. Absolute SPECT/CT quantification of radioactive uptake in NM is used in the estimation of organ doses, evaluation of new radiopharmaceuticals and lately the determination of treatment response (Ritt et al., 2011). Absolute quantification in NM refers to a process of recovering counts from the patient images and then converting these

counts to absolute radioactivity through the use of a calibration factor. The calibration factor is determined from the radionuclide dose calibrator and gamma camera measurements. It converts the counts from the gamma camera images to absolute activity.

In NM, ^{99m}Tc is used as the radionuclide of choice to quantify defects in clinical studies such as myocardial and lung perfusion studies (Fricke et al., 2004; Tamaki et al., 2001). On the other hand, quantification with ^{123}I/^{131}I is used in Metaiodobenzylguanidine (mIBG) studies for the selection of patients with high tumour tracer uptake for radionuclide treatment with ^{131}I (IAEA, 2008).

1.3 Motivation for the current study

Currently, verification of the accuracy of absolute SPECT image quantification has not been performed with the SPECT/CT gamma camera in the NM department at Universitas Hospital, Bloemfontein, South Africa. The SPECT/CT system in NM department is equipped with the manufacturer software for image acquisition and processing. A comprehensive Abdominal Phantom study was needed to evaluate the quantification accuracy for a given radionuclide, acquisition and reconstruction protocol under the conditions similar to patient studies. Since the beginning of SPECT quantification, there has been no standardized method for the acquisition and processing of SPECT data. This necessitates more data gathering from different centres in order to study SPECT quantification carefully which might lead to standardized protocols.

1.4 The aim of the study

The aim of this work was to evaluate the influence of the geometry of a radionuclide distribution on SPECT quantification accuracy for ^{99m}Tc and ^{123}I in an Abdominal Phantom.

1.5 References

Cherry, S.R., Sorenson, J.A., Phelps, M.E., 2012. chapter 16 - Tomographic Reconstruction in Nuclear Medicine, in: Phelps, S.R.C.A.S.E. (Ed.), Physics in Nuclear Medicine (Fourth Edition). W.B. Saunders, Philadelphia, pp. 253–277.

Frey, E.C., Humm, J.L., Ljungberg, M., 2012. Accuracy and precision of radioactivity quantification in nuclear medicine images. Semin. Nucl. Med. 42, 208–218.

Fricke, H., Fricke, E., Weise, R., Kammeier, A., Lindner, O., Burchert, W., 2004. A Method to Remove Artifacts in Attenuation-Corrected Myocardial Perfusion SPECT Introduced by Misalignment Between Emission Scan and CT-Derived Attenuation Maps. J. Nucl. Med. 45, 1619–1625.

IAEA, 2008. Clinical Applications of SPECT/CT: New Hybrid Nuclear Medicine Imaging System (IAEA-TECDOC-1597). Vienna, Austria.

Pereira, J.M., Stabin, M.G., Lima, F.R.A., Guimarães, M.I.C.C., Forrester, J.W., 2010. Image quantification for radiation dose calculations--limitations and uncertainties. Health Phys. 99, 688–701.

Ritt, P., Vija, H., Hornegger, J., Kuwert, T., 2011. Absolute quantification in SPECT. Eur. J. Nucl. Med. Mol. Imaging 38 Suppl 1, S69–77.

Song, N., He, B., Frey, E.C., 2010. The effect of volume-of-interest misregistration on quantitative planar activity and dose estimation. Phys. Med. Biol. 55, 5483–5497.

Tamaki, N., Kuge, Y., Tsukamoto, E., 2001. The Road to Quantitation of Regional Myocardial Uptake of Tracer. J. Nucl. Med. 42, 780–781.

Chapter 2

Single photon emission computed tomography image quantification

CHAPTER 2 2-1

2.1 INTRODUCTION 2-2
2.2 PHOTON INTERACTIONS IN A MEDIUM 2-2
2.2.1 Photoelectric absorption 2-3
2.2.2 Compton scattering 2-3
2.2.3 Pair production 2-5
2.3 THE GAMMA CAMERA 2-5
2.4 SINGLE PHOTON EMISSION COMPUTED TOMOGRAPHY IMAGING 2-8
2.5 RECONSTRUCTION OF SPECT IMAGES 2-8
2.5.1 Filtered Back Projection 2-10
2.5.2 Ordered Subset Expectation Maximization 2-11
2.5.2.1 OSEM mathematical background 2-12
2.6 CORRECTION OF SPECT DATA 2-15
2.6.1 Attenuation correction 2-15
2.6.1.1 Transmission measurements with a radionuclide 2-16
2.6.1.2 Transmission measurements with a CT scanner 2-17
2.6.2 Scatter correction 2-19
2.6.2.1 Dual Energy Window scatter correction technique 2-21
2.6.2.2 Triple Energy Window scatter correction technique 2-22
2.6.3 Collimator Detector Response 2-24
2.6.4 Partial Volume Effect 2-24
2.7 QUANTIFICATION OF RECONSTRUCTED SPECT DATA 2-26
2.7.1 SPECT calibration factor 2-26
2.7.2 Influence of Region of Interest on quantification 2-28
2.8 DISCUSSION 2-29
2.9 REFERENCES 2-32

2.1 Introduction

Quantification in NM has developed over the years as a valuable tool for clinicians. The evolvement of the gamma camera as well as processing software improved quantification accuracy in NM. Different quantification indices have been used in the past; these include relative quantification from count ratios, activity in a region as a percentage of the total injected activity, absolute activity and activity concentration. Other functional quantification indices commonly used in NM are ejection fraction, metabolically active tumour volumes and metabolism impaired volumes (IAEA, 2014; Ceriani et al., 2010).

In this chapter, photon interactions with matter will be explained briefly. An overview of the gamma camera design as well as the developments of SPECT reconstruction algorithms will be discussed. The importance of these developments for quantification will be highlighted. The most commonly used reconstruction algorithms in NM are the filtered back projection and the iterative reconstruction algorithms. The different corrections that can be incorporated during reconstruction to improve the image quality and quantification will also be discussed.

2.2 Photon interactions in a medium

The gamma photons emitted from the radionuclides interact with matter in a way that depends on their energy and the composition of the absorber. Gamma photons have different types of interactions with matter; elastic scattering, photoelectric absorption, inelastic (Compton) scattering, pair production and photonuclear reactions. Pair production and photonuclear reactions are however not of interest in single photon scintigraphy imaging since these interactions require higher photon energies than those produced by the radionuclides normally used in these types of studies.

2.2.1 Photoelectric absorption

In the photoelectric absorption interaction all of the incident photon energy is transferred to an electron, which is ejected from the atom. The photoelectric interaction occurs at low photon energies where the incident photon interacts with the orbital electron. The incident photon energy must be greater than or equal to the binding energy of the orbital electron, in order for the electron to be ejected. The excess energy of the incident photon gives the ejected electron kinetic energy. The liberated electron deposits its energy locally because of the relatively short range in a tissue medium. After the photoelectric process the atom is ionized with an inner shell electron vacancy. This vacancy is filled by an electron from a lower binding energy shell resulting in characteristic X-rays or Auger electrons. The probability of photoelectric absorption taking place is proportional to Z^3/E^3. (Z = atomic number of the absorbing material, E = energy of the incident photon). This implies that the photoelectric absorption is more prominent at low photon energies and in materials with high atomic numbers. The probability of photoelectric absorption in SPECT NM imaging in bone tissue is thus higher than in soft tissue.

2.2.2 Compton scattering

During Compton interaction the incident photon interacts most likely with an outer shell electron. After interaction, the photon is scattered through an angle of deflection (φ) with some loss of its initial energy and at the same time the electron is ejected from the atom. Thus, the probability of Compton scattering increases with an increase in energy of the incident photon. The energy of the scattered photon is calculated using equation 2-1 when the energy of the incident photon and scattering angle of the scattered photon are known:

$$hv' = \frac{hv}{1 + \frac{hv}{m_0 c^2}(1 - \cos\varphi)} \qquad 2\text{-}1$$

Where hv is the incident photon energy, hv' is the scattered photon energy, φ is the angle of the scattered photon, with $hv = {}^{hc}/_{\lambda}$ where h is Plank's constant, c is speed of light and λ is the wavelength ($\lambda = {}^{c}/_{v}$).

Equation 2-1 implies that for large scattering angles (φ) the lower the energy of the scattered photon which will contribute to the scatter region in the energy spectrum.

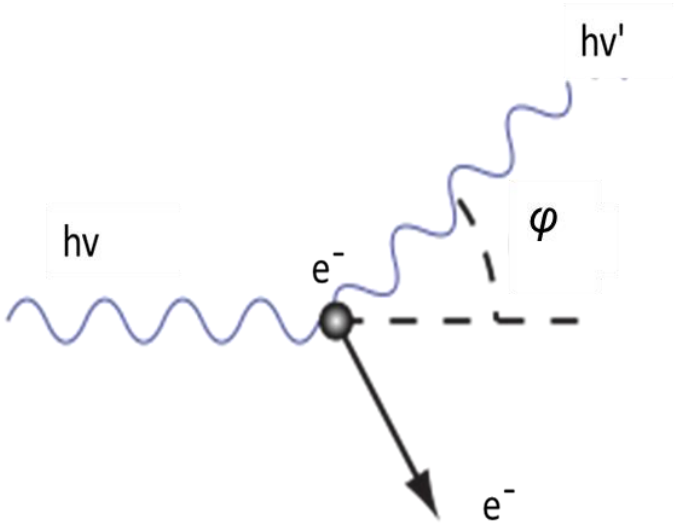

Figure 2-1*: The mechanisms of the Compton interaction processes that result in scattered photons within patients. The energy of the incident photon is indicated by hv, the energy of the scattered photon scattered with an angle φ, is hv' and e- indicates the recoil electron.*

Compton scatter thus entails directional change of a γ-ray with energy loss to a recoil electron resulting in loss of spatial information. The amount of energy loss by the γ-ray during Compton scatter depends on, amongst others, the scattering angle relative to its initial direction and the incident energy as seen from equation 2-1. It is important to note that Compton scatter is the predominant interaction of gamma rays in the energy range above 26 keV in soft tissue (Bushberg et al., 2011). It thus plays an important role in SPECT NM imaging.

2.2.3 Pair production

Pair production occurs when a high energy photon interacts with the nucleus of an atom and the photon is transformed into an electron-positron pair. Pair production happens at high incidence photon energy with a threshold of 1.022 MeV and with excess energy given to the electron-positron pair as kinetic energy. Pair production only becomes significant when the incident photon energy exceed the 1.022 MeV energy threshold. These energies are not encountered in the SPECT environment. Hence it is not a concern for SPECT.

2.3 The gamma camera

In the developmental stages of NM the rectilinear scanners were the principal imaging devices. Planar images of the patients were acquired point by point with the rectilinear scanner, which resulted in long imaging times. The gamma cameras (Figure 2-2) gain popularity because imaging was performed much faster than with rectilinear scanners and the bigger field of view resulted in multiple organs being viewed simultaneously during a single scan (Jaszczak, 2006).

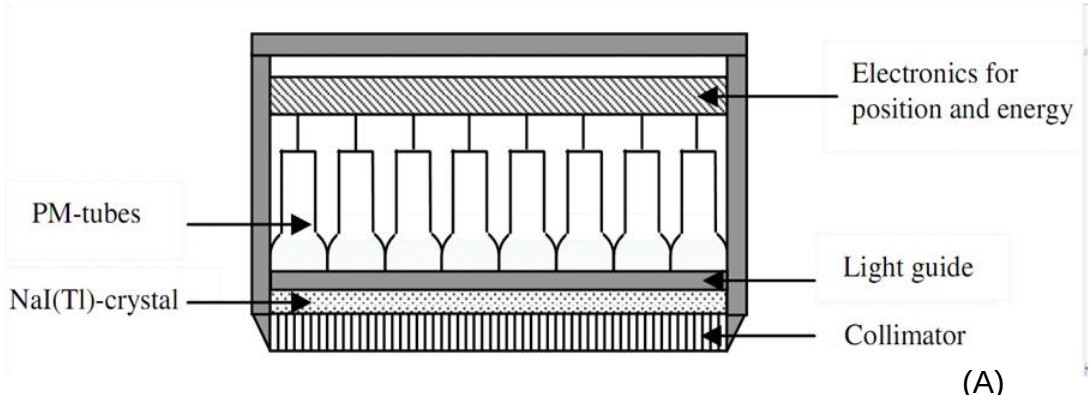

(A)

(B)

Figure 2-2: *(A) The different components of a gamma camera detector. (B) A dual head SPECT gamma camera mounted on a rotating gantry.*

The gamma camera detector used for scintigraphy imaging was developed in the late 1950's by Hal Anger (Hine, (1967); Mallard, (2003)). The basic components of the gamma camera today are in many cases the same as when it was invented, but its performance has improved over the years. The first component of a gamma camera that interacts with incident photons is the collimator. A collimator is made of a high atomic number material such as lead (Pb). The collimator consists of a large number of small holes drilled through the Pb plate. These holes can have different shapes, i.e. circular or hexagonal and the hole orientation can be parallel, slanted, diverging or converging. The collimator restrict photon rays from the radioactive source in that only rays traveling perpendicular to the crystal can pass through the holes of the collimator

and reach the scintillation crystal. On the other hand, incident photons not travelling parallel through the collimator holes are absorbed by the septa between the collimator holes. The parallel collimator illustrated in Figure 2-2(A) is most often used in the SPECT environment. The most commonly used scintillation crystal in a gamma camera detector is sodium iodide doped with thallium (NaI(Tl)). The crystal detects gamma rays when they interact with the crystal by the interaction processes explained in section 2.2 in particular photoelectric absorption. After gamma ray interaction in the crystal, the produced visible light is converted to photoelectrons at the photo cathodes of the photomultiplier tube (PMT) and these electrons are amplified through the dynodes of the PMTs. The PMT output is fed through the analogue to digital converter (ADC). The ADC converts the analogue pulse height signal to digital data which is stored in the acquisition computer. Improvements in recent designs of integrated circuits technology, stability of electronic components and PMTs signal digitization technology of individual PMTs combined with significant computer processing speed resulted in a new interest in image quantification. The improvement in these technologies meant that gamma camera performance characteristics such as count rate, intrinsic uniformity and resolution have also improved (Wernick and Aarsvold, (2004)).

The problem of accurately delineating organs of interest when overlying and/or underlying organs are present in planar NM imaging was solved by the introduction of SPECT. However, SPECT suffers from longer acquisition times which led to the introduction of dual and triple head gamma cameras. Longer acquisition times can lead to patient motion artefacts. SPECT also suffer from poor spatial resolution when compared to other modalities like computed tomography (CT) that is used for delineation of tumour boundaries and for providing attenuation coefficient information. Thus the delineation of the organ of interest in close proximity to a high uptake organ poses a challenge. A hybrid SPECT/CT system allows for better delineation of organs when the SPECT and CT images are superimposed onto each other. The hybrid system has also the advantage of generating attenuation maps from the CT images to correct for photon absorption. Another advantage of using such a hybrid SPECT/CT system is

that the mis-registration of the functional and anatomical images are minimized when SPECT and CT images are superimposed for delineating organs of interest.

2.4 Single Photon Emission Computed Tomography imaging

The acquired 2D planar projections obtained during SPECT imaging are used for the reconstruction of a 3D image volume, which ideally should correspond to the activity distribution in the patient. In most cases a “step and shoot” acquisition technique is used, with no data collected during the detector movements. The 2D projections are acquired in a circular or non-circular orbit around the patient using the auto contour facility of the gamma camera. The auto contour capability minimizes patient to collimator distance in SPECT when a non-circular orbit acquisition mode is used. The number of projections varies between 64 and 128, equally distributed in space. A complete SPECT acquisition measures projections over a 180 or 360 degree rotation arc.

2.5 Reconstruction of SPECT images

Reconstruction algorithms have been well investigated in the literature (Zaidi, 2005). There are assumptions made in the reconstruction process:

- The count in a voxel should be linearly proportional to the amount of activity contained in the tissue volume corresponding to the location of that voxel. This is however not true in practice due to assumptions made in reconstruction algorithms.
- The line of response for a collimator hole is an extended cylinder; however the actual response for a collimator hole resembles a diverging cone.
- Attenuation effect is ignored.

- Activity outside the line of response does not contribute to the signal for the projection element however, crosstalk between elements are present due to scatter.

A simple analytical reconstruction algorithm used in NM is filtered back projection which has been used widely. The wide spread use of FBP was due to its ease of implementation, practical reconstruction times and the lower space requirements on the computer memory which is now not applicable. However, there are limitations associated with FBP. These include radial distance from the source to the detector (linear sampling), the angular sampling (number of projections), sampling coverage, noise propagation and FBP cannot be modified to include the physical properties of the imaging system (Cherry et al., 2012). The inadequacy in both the linear and angular sampling results in reduced spatial resolution and can cause artefacts in the reconstructed images. FBP is prone to streak artefacts and noise because of the use of a ramp filter enhancing the high spatial frequencies (Zaidi, 2005).

There was also a need for reconstruction algorithms that takes into account the defective nature of the acquired SPECT data for image formation. Defective acquired SPECT data occurs when the object data is incomplete and when the dataset is of poor counting statistics or contains random noise (Cherry et al., 2012). The algorithms that can incorporate the corrections for the defective SPECT data during reconstruction are referred to as iterative reconstruction algorithms. The capability of iterative reconstruction algorithms to account for physical phenomena and a non-ideal imaging system is an advantage over the FBP (Bruyant, 2002). The FBP and OSEM reconstruction algorithms are briefly discussed in sections 2.5.1 and 2.5.2 respectively.

An alternative to the analytical reconstruction algorithm, are the iterative reconstruction methods, in particular statistically based iterative algorithms (Wallis and Miller, 1993).

The widespread use of iterative reconstruction is based on the ability to accurately model attenuation, scatter and collimator-detector response (CDR) in a clinically acceptable time (Römer et al., 2006). There are different kinds of iterative reconstruction methods such as Algebraic Reconstruction Technique, Simultaneous Iterative Reconstruction Technique, Iterative Least Square Technique and Maximum Likelihood Expectation Maximization (MLEM) (Shepp and Vardi, 1982). The MLEM has been widely investigated for application in NM images and its properties are well known (Vandenberghe et al., 2001; Miller and Wallis, 1992; Müller et al., 1990; Inouye et al., 1989).

A problem encountered with iterative reconstruction algorithms particularly MLEM is the convergence as a function of its reconstruction parameters. In a phantom study by Lazaro et al., (2005), the reconstruction parameters of the MLEM algorithm were optimized and the number of iterations that resulted in convergence was obtained. Regrettably, in the past MLEM convergence required too many iterations which resulted in longer processing times which was not practical to use in routine NM image reconstructions (Brambilla et al., 2005 ; Boellaard et al., 2001). Convergence is defined differently by various researchers. Tsui et al., (1994a) and Meikle et al., (1994) defined convergence using the mean square error (MSE) in their respective studies and regarded the iterative algorithm to have reached convergence when the MSE was a minimum.

2.5.1 Filtered Back Projection

A back projection method simply takes each of measured projection profiles and projects it uniformly over the image pixels that lie along the projection ray passing through the projection bin. The images reconstructed with back projection are blurred because the counts are placed outside boundaries of an object, making it difficult to segment edges. The blurring effect can be reduced by applying a deconvolution filter to

the projection data and then back projecting the filtered data to form an image. This is the basis of the filtered back projection reconstruction algorithm. The Ramp filter is used to remove blurring in FBP, because of its effect of filtering out low frequencies and passing high frequencies, with a linear behaviour in between. Thus with this filter, contrasting features (high-frequencies) are accentuated, while blurring (low-frequencies) is minimized.

As mentioned in section 2.5, the FBP has been widely used in NM departments. FBP has the advantage of reliable visual results in the absence of noisy data and is fast and easy to implement. The disadvantage of the FBP reconstruction method is the assumption made that no image degrading effects are present during the imaging process in addition to those described in section 2.5. Although scatter correction and attenuation correction (Chang's correction method) methods can be applied, they are included as pre- or post-reconstruction manipulations with varying degree of success (Cherry et al., 2012).

2.5.2 Ordered Subset Expectation Maximization

The Ordered Subset Expectation Maximization (OSEM) was proposed by Hudson and Larkin (1994). OSEM is related to the MLEM algorithm and has reduced the number of iterations needed to attain convergence. For OSEM the data is processed in blocks of projections called subsets with the results showing accelerated convergence compared to MLEM by a factor proportional to the number of subsets (Hutton et al., 1997). The superior performance of OSEM over FBP has been well established (Dickson et al., 2010; Stansfield et al., 2010; Gutman et al., 2003). The choice of which parameters (number of iterations and number of subsets) to employ during OSEM reconstruction is not entirely obvious (Brambilla et al., 2005). An increased number of iterations improve the resolution and contrast of the reconstructed image to better match the original image, but also increase the noise in the reconstructed images (Brambilla et al., 2005).

A high noise level can be avoided by stopping the reconstruction at an early iteration step or by the application of a post-reconstruction filter. Additionally, Hutton et al., (1997) recommend that the number of subsets should be as large as possible but not exceeding one-quarter of the number of projections.

2.5.2.1 OSEM mathematical background

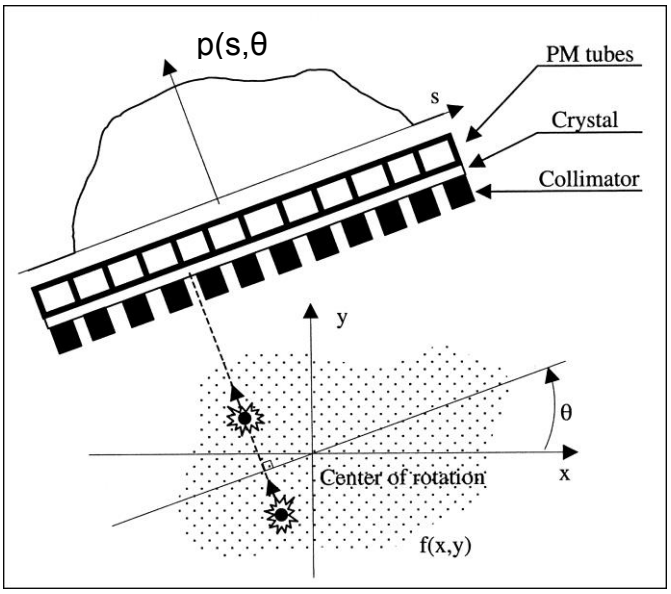

Figure 2-3**:** *A detector rotating around an object with activity distribution f(x,y) emitted to produce projection p(s,θ) at detector angle (θ) for scintillation events detected at position (s) in a detector (Bruyant, 2002).*

Consider a distribution of activity $f(x,y)$ in Figure 2-3 in a slice through an object. The measured set of projections from the corresponding slice is given by p(s,θ), where s represent the distance along a projection and θ represent the angle of acquisition. Let the number of photons emitted from voxel *j* be denoted by f_j, and the probability that a photon emitted from voxel *j* is detected in projection element *i* is given by equation 2-2 where p_i is the set of projection pixel values during forward projection and the relationship is described by the transition matrix a_{ij}, The transition matrix incorporates

the correction factors (i.e. detector geometry, attenuation and resolution among others) that degrades the resultant projections.

$$p_i = \sum_j a_{ij} f_j^n \qquad 2\text{-}2$$

Essentially equation 2-2 determines the expected projections based on the estimate activity distribution. According to (Zaidi, 2005), OSEM reconstruction is achieved by using subsets of projections denoted by S and iterations denoted by n in equation 2-3.

$$f_j^{n+1} = \frac{f_j^n}{\sum_{i \in Sn} a_{ij}} \sum_{i \in Sn} a_{ij} \frac{P_i}{\sum_k a_{ik} f_k^n} \qquad 2\text{-}3$$

The illustration of the OSEM reconstruction algorithm is shown in Figure 2-4, the process begins with an initial estimate of the object count distribution. The forward projection is then used to estimate the projection that would have arisen from the initial object. The estimated projection is then compared to the measured projection. If the estimated projections differ from the actual measured projections, the difference is used to modify the original estimate by using the ratio of the measured projection to the estimated projection and multiplying it at each point with the correction image through back projection. The adjusted object then becomes the starting point for the next iteration. The process is continued until a final solution is reached, usually after a predetermined number of iterations and subsets. The stopping point is chosen when there is a very small difference between the measured and the estimated projections.

The advantages of iterative reconstruction algorithms are that they can process inconsistent data (including missing data) and attempts to model noise with the result of improved noise property in the resultant object. They can handle complex image degrading effects like the attenuation, scatter and distance dependent resolution among

others. The streak artefacts associated with FBP is greatly reduced with the iterative reconstruction algorithm. The iterative reconstruction algorithms are better suited for quantitative accurate reconstruction, on condition that caution is used in the choice of reconstruction parameters (Zaidi, 2005; Müller et al., 1990).

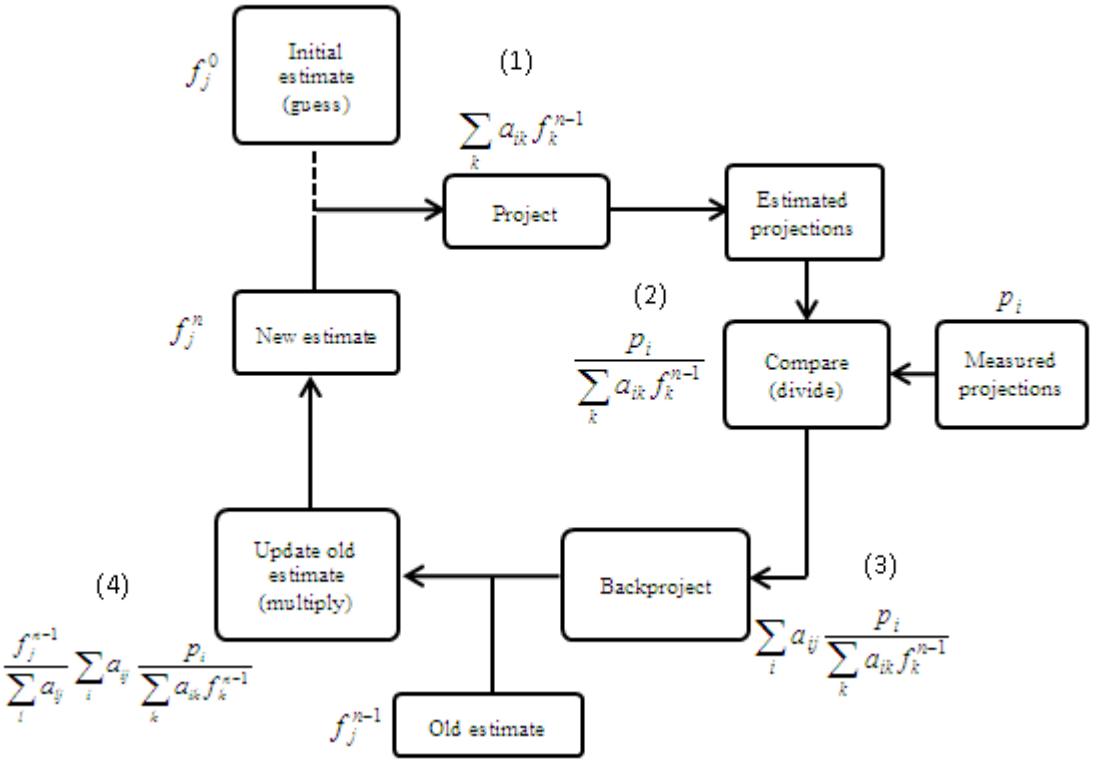

***Figure 2-4**: Flow diagram of OSEM algorithm: (1) an initial estimate f_j^0 is made. Based on this starting point an estimate of the projection is calculated using forward projection. (2)The estimated projection is then compared with the measured projection p_i by using the ratio of the measured projection to the estimated projection. (3) The comparison is used to modify the estimate by back projecting the ratio (4) and multiplying the initial estimate by the correction image. The process is repeated until convergence is reached i.e. when the difference reaches a pre-set level.*

2.6 Correction of SPECT data

2.6.1 Attenuation correction

Photon attenuation refers to photons that undergo photoelectric absorption and Compton scatter within the material/medium they are traversing. Photon attenuation affects the accuracy of SPECT activity quantification by decreasing the number of detected counts. Consider a number of photons (N_0) incident onto a homogenous material of thickness (x). The number of transmitted photons (N) detected is given by:

$$N = N_0 e^{-\mu x} \qquad 2\text{-}4$$

Where μ is the linear attenuation coefficient for a medium which depends on the photon energy, thickness and density of the medium (Tsui et al, 1994b). According to equation 2-4, the number of photons reaching the detector is reduced to N, in other words, there has been a decrease in the number of photons available for image formation, thus causing inaccurate activity quantification. The underestimation in quantified activity can be corrected by applying a patient specific attenuation map (distribution of attenuation coefficients) to correct for attenuated photons in a nonhomogeneous medium as recommendation by Flux et al., (2006).

There are several methods that can be used to obtain the distribution of attenuation coefficients in a medium. The commonly used uniform attenuation correction is described by Chang, (1978). It assumes homogeneous attenuation throughout an object and requires a known body contour to obtain an estimate of the attenuation path length for all projection. It has the advantage of fast processing times when incorporated in the iterative reconstruction process and the disadvantage of producing images of varying image quality with the number of iterations (Tsui et al., 1994b). Nonetheless, this method have been widely used in liver and brain SPECT imaging (Warwick et al., 2011; Tamaki et al., 2001). The disadvantage of Chang's attenuation correction method on

activity quantification is that the human body does not comprise of a uniform attenuating medium (Ritt et al., 2011). The Chang's method corrects for both attenuated and scattered photons simultaneously implying that the scatter correction component is stationary. A more sophisticated method is necessary to overcome the shortcomings of Chang's method in a heterogeneous medium for patient specific attenuation correction.

2.6.1.1 Transmission measurements with a radionuclide

A more accurate attenuation correction can be applied by measuring the true attenuation distribution by using radionuclide transmission scans. This requires the acquisition of a transmission scan without a patient or phantom ("blank scan" (N_{blank})) followed by the acquisition of a transmission scan (N_{trans}) of the patient or phantom. The natural logarithm of the exponential relationship (equation 2-4) is obtained to calculate the linear attenuation coefficient (μ) (equation 2-5):

$$\ln\left(N_{blank}/N_{trans}\right)=\mu x \qquad 2\text{-}5$$

The projection profiles thus represent the sum of the attenuation coefficients along each line of response (equation 2-5).

$$\mu x=\sum_i \mu_i \Delta x_i \qquad 2\text{-}6$$

Where μ_i is the linear attenuation coefficient for i^{th} pixel and Δx_i is the path length of the line of response through the i^{th} pixel.

The transmission and emission scans can be obtained with the same radionuclide, thus gaining the advantage of eliminating the need for the transformation of the calculated attenuation coefficient to the appropriate emission energy. However, the use of a radionuclide with a different energy as the emission energy has an advantage of simultaneous imaging, but the disadvantage of the need to transform the attenuation coefficient as described previously. The radionuclide transmission scans suffer from poor quality due to statistical noise, limited spatial resolution, contamination of the attenuation map (cross talk) and long acquisition times among other factors (Fricke et al., 2004; Kinahan et al., 2003, 1998; Ritt et al., 2011). Contamination of the attenuation map (crosstalk) can arise from the “spill-over” of radionuclide emission photons into the radionuclide transmission scan when the two scans are acquired simultaneously. An alternative method to obtain attenuation coefficient maps is discussed in the following section.

2.6.1.2 Transmission measurements with a CT scanner

A method to obtain accurate attenuation coefficient information in a relatively short acquisition time is the use of an X-ray transmission source. The X-ray transmission scans are superior to radionuclide transmission scans in that the acquired data have lower statistical noise, and data can be acquired post injection without risk of contamination (crosstalk) of the emission data (Zaidi and Hasegawa, 2003). There are however problems associated with CT generated attenuation maps, for example metal prosthesis and respiratory motion in patients introduce artefacts (Frey et al., 2012; Kinahan et al., 2003) but also other factors that will be discussed.

As mentioned in Chapter 1, a CT scanner uses an X-ray source which forms an integral part of the hybrid SPECT/CT gamma camera in NM to obtain anatomical information. This information can be used to provide attenuation coefficients in order to compensate for attenuated photons during reconstruction of the activity distribution. The

reconstructed CT images are expressed in Hounsfield units (or CT numbers) by employing equation 2-7, to standardize the data and to have sufficient grey scale values for image display (Patton and Turkington, 2008).

$$CT\ number = \left[\left(\mu_{tissue} - \mu_{water}\right)/\mu_{water}\right] \times 1000 \qquad 2\text{-}7$$

Where μ_{water} and μ_{tissue} are the attenuation coefficients for water and tissue at the effective energy of the CT scanner respectively. From equation 2-7 it can be shown that the CT number of water is selected to be 0 and that of air is equal to –1000.

The output of the CT tube provides a wide spectrum of X-ray energies (polyenergetic), which necessitates a large amount of beam filtration to reduce low energy photons and increase the effective energy of the beam (beam hardening). The method to determine the effective CT energy was discussed in details by Kinahan et al (1998). The linear attenuation coefficients at the effective energy of the CT have to be converted to an attenuation map with the appropriate photon energy of the imaging radionuclide (Ritt et al., 2011). The conversion method used routinely is a bilinear model (Brown et al., 2008; Kinahan et al., 2003). For CT numbers of less than 0, the measured tissue is assumed to be a combination of air and water; the attenuation coefficient at the desired energy can be calculated using equation 2-8 which is the first component of the model.

$$\mu_{tissue,nkeV} = \frac{CT\# \times \left(\mu_{water,nkeV} - \mu_{air,nkeV}\right)}{1000} \qquad 2\text{-}8$$

Where $\mu_{tissue,nkeV}$, $\mu_{water,nkeV}$ and $\mu_{air,nkeV}$ are attenuation coefficients of tissue, water and air respectively at specified radionuclide energy (nkeV) and CT# is the Hounsfield unit for tissue.

The second component of the bilinear model is for CT numbers greater than 0, which is a combination of water and bone. Therefore, the attenuation correction at the desired energy is calculated by using equation 2-9.

$$\mu_{tissue,nkeV} = \mu_{water,nkeV} + \frac{CT\# \times \mu_{water,keVeff} \times \left(\mu_{boner,nkeV} - \mu_{water,nkeV}\right)}{1000 \times \left(\mu_{tissue,keVeff} - \mu_{water,keVeff}\right)} \qquad 2\text{-}9$$

Where $\mu_{bone,nkeV}$ is the attenuation coefficient of bone at a specified radionuclide energy (nkeV), and $\mu_{water,\ keVeff}$, $\mu_{tissue,\ keVeff}$ are the attenuation coefficients of water and tissue respectively at the effective energy of the acquiring CT scanner .

2.6.2 Scatter correction

As explained earlier in section 2.2, Compton scattered photons also contribute to image formation because some of the scattered photons are detected in the photo peak. This causes image degradation, particularly in the relationship between image intensity and the measured activity (Willowson et al., 2008). The limited energy resolution of the NaI(Tl) crystal makes it difficult to remove all the Compton scattered photons from the photo peak based on the photon energy difference (Axelsson et al., 1984).

Several scatter corrections methods are available and discussed in the literature (Buvat et al., 1994; Ljungberg et al., 1994; Pretorius et al., 1993b). A number of these scatter corrections methods were compared amongst each other (Buvat et al., 1995; Ljungberg et al., 1994). The outcome of the study by Buvat et al., (1995) was that scatter correction methods employing only the photo peak window cannot be used for quantification, while scatter correction methods using two or more energy windows that include the photo peak window give more accurate quantification results. While Ljungberg et al., (1994) found that the differences in the estimated scatter from different scatter correction methods did not have a significant improvement on the final

quantification. Only window based scatter correction methods will be discussed. The other group of scatter correction methods are model based techniques that includes the convolution technique by Axelsson et al., (1984) and the computationally intensive Monte Carlo simulations (Riauka et al., 1996). Hutton et al., (2011) reported that there has been limited use of the model based scatter correction for routine clinical implementation with the exception of one vendor who implemented the effective scatter source estimation (ESSE) developed by Frey and Tsui, (1996). The limited use of model based scatter correction techniques is because of the difficulty in isolating the impact of correcting for scatter in a specific experimental design.

Window based scatter correction methods include for example the convolution subtraction method that uses transmission measurements in estimating the scatter fraction for each projection pixel (Smith and Jaszczak, 1994). The channel ratio method proposed by Pretorius et al., (1993b) is based on two symmetric adjacent energy windows spanning the photo peak to determine the scatter contribution in the two energy windows. The disadvantage of this method is that calibration is required for a specific gamma camera and photon energy, and is not valid for radionuclides with multiple photon emissions. The method also requires a stable photo peak position of the gamma camera during SPECT acquisition.

The Dual Energy Window (DEW) (Jaszczak et al., 1984), and the Triple Energy Window (TEW) (Ogawa et al., 1991) scatter correction techniques are simple to apply and measure scatter directly. These scatter correction methods have been proven to improve quantification accuracy under a particular geometry and ideal experimental conditions (Buvat et al., 1995).

2.6.2.1 Dual Energy Window scatter correction technique

The DEW approach that was proposed by Jaszczak et al. (1984), assumes that a window immediately below the photo peak window (Figure 2-5) monitors the number of scattered counts contributing to the total counts within the photo peak window. The DEW scatter correction method use two energy windows: the lower scatter window and the photo peak window in Figure 2-5. This method further assumes that the spatial distribution of scattered photons detected in the photo peak window can be estimated by the spatial distribution of photons detected in a secondary window. The spatial distribution of these two windows was assumed to differ quantitatively by a fixed ratio k. The value for the ratio was originally determined from the ratio between the scatter in the photo peak window and the scatter in the lower scatter energy window of a line source as shown by equation 2-10:

$$P_p = P_0 - \left[k \cdot P_s\right] \qquad 2\text{-}10$$

Where P_p represent the photo peak photons only.

P_0 the photo peak photons and scattered photons

P_s the scattered photons only and

k is a constant

The disadvantage of the DEW scatter correction method is in its inability to properly correct for scatter when multiple emission radionuclides are used. The studies done by Koral et al., 1990 and Ljungberg et al., 1990 respectively, showed that the k value need to be recalculated for different geometries especially for quantification. Ljungberg et al. (1994) reported that this method predicted more scatter than was present in a true scatter image. Additionally, Buvat et al., (1995) reported that scatter window subtraction

results in an overcorrection far from the source location as well as an under-correction near the source which resulted in enhanced contrast which made relative quantification misleading.

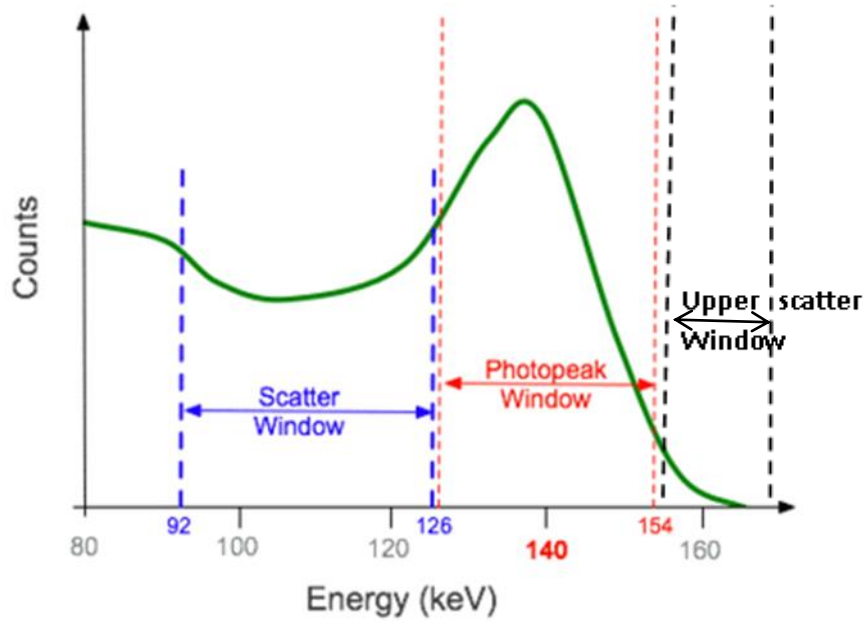

***Figure 2-5**: The window selection for the dual energy window (DEW) and modified triple energy window (TEW) scatter correction technique displayed for the ^{99m}Tc spectrum. The lower scatter window (indicated in blue) and the photo peak window (indicated in red) are selected for the DEW scatter correction, while all three displayed windows are selected for the modified TEW scatter correction.*

2.6.2.2 Triple Energy Window scatter correction technique

Ogawa et al. (1991) proposed a TEW scatter correction method that utilizes three energy windows of the energy spectra generated by photons escaping from the imaged object (Figure 2-5). Two narrow 3 keV scatter energy windows are selected on either side of the primary photo peak (Ogawa et al., 1991). The information in these scatter windows is used to estimate the amount of scatter in the primary window. The estimated scattered (equation 2-11) data is then subtracted from the primary photo peak data for each pixel (equation 2-12).

$$C_{scat} \cong \left(\frac{C_{left}}{W_s} + \frac{C_{right}}{W_s} \right) \frac{W_m}{2} \qquad 2\text{-}11$$

$$C_{prim} = C_{total} - C_{scat} \qquad 2\text{-}12$$

Where, C_{left} counts in lower scattered rejection window.

C_{right} counts in upper scatter rejection window

C_{total} counts in photo peak window

C_{scat} counts of scattered photons mixed in photo peak window

C_{prim} counts of non-scattered photons in photo peak window

W_s width of scatter rejection window

W_m width of photo peak window

The TEW method is used mainly for multiple emission radionuclides to correct for down scatter from higher energy emissions. In the case of a single emission radionuclide like ^{99m}Tc the upper energy window is eliminated as mentioned previously. The disadvantage of the TEW scatter correction method is the excessive noise if the two monitoring scatter windows are too narrow due to low count statistics (Ouyang et al., 2008; Zaidi, 2005). On the other hand the use of wider scatter windows (modified TEW) results in a poor trapezoidal approximation that have a direct influence on the scatter correction while reducing excessive noise (Frey et al., 2012). The advantage of TEW method is that a system calibration is not needed as in the case of DEW method (Dewaraja et al., 1997). The TEW scatter correction method has been accepted as a standard method for correcting for scatter due to its simplicity and effectiveness in complex geometry encountered clinically (Hutton et al., 2011). The modified TEW

scatter correction (TEW method with increased scatter window widths) is used commercially for example by Siemens gamma cameras.

2.6.3 Collimator Detector Response

The Collimator-Detector Response (CDR) function (also termed geometric blurring effect) of SPECT refers to an image formed from a point source of radioactivity. The shape of the CDR is the main factor that determines the image resolution in SPECT. According to Zaidi, (2005), the CDR for SPECT is determined by the following factors: intrinsic camera response due to uncertainty in position and scatter within the crystal, collimator characteristics such as septal penetration and septal scatter, and the geometric response. Ideally, a CDR with a delta function is desirable but because of the factors mentioned above the resulting CDR is a wider tailed function.

The CDR of parallel-hole collimators in SPECT imaging is a source of error in the reconstructed images. The OSEM reconstruction algorithm (section 2.5.2) corporates correction for CDR in the transition matrix in both the transverse and axial direction during the image formation process. Incorporation of the depth-dependent resolution in OSEM which is isotropically recovered means the final reconstruction should have resolution recovery. Flash 3D (Siemens medical solutions, Inc.) is an example of such a resolution recovery reconstruction algorithm (Vija et al., 2003; Hutton et al., 1997). Flash 3D models CDR in both the transverse and axial directions therefore small lesions will be reconstructed with more counts in the correct volume, hence improving image contrast (Vija et al., 2003).

2.6.4 Partial Volume Effect

Partial Volume Effect (PVE) refers to loss of signal due to the limited extent of the object with respect to the spatial resolution or FWHM of the imaging system and to the contamination of activity from neighbouring tissue also known as the spillover effect

(Boussion et al., 2009; Pretorius and King, 2009; Rousset et al., 1998). The PVE is particularly pronounced in regions that are less than 3 times the FWHM of the imaging system (Seo et al., 2010). The partial volume effect arise from the reconstructed images that result in pixel/voxel values at the edges that are mixtures of different tissues activities, which is known as tissue-fraction effect (Le Pogam et al., 2011).

Several studies have investigated methods to decrease the impact of PVE. A well-established method to correct for PVE is the application of Recovery Coefficients (RC) through predetermined measurements (Zeintl et al., 2010). It involves a series of measurements of different object sizes with activity and the generation of a calibration curve. The drawback of this method is that in most cases the size of the object of interest is unknown (Chen et al., 1999). The model based PVE correction was investigated to eliminate the need for object specific calibration curves. Nuyts et al., (1996) used an explicit region of interest (ROI) for the left ventricular wall (in myocardial perfusion imaging study) and a convolution model for the gamma camera point response function to determine the RC and spillover coefficient. Tang et al., (1997) used a similar method, termed “template-projection reconstruction” where RC was determined voxel-by-voxel from the coregistered CT images. The template-projection was adapted by Pretorius and King, (2009), with modifications, where an additional parameter, voxel filling fraction, was introduced. The application of these techniques are limited in SPECT due to the need for additional high resolution imaging modalities like CT or MRI (Chen et al., 1999).. However, with the use of hybrid SPECT/CT systems both of these limitations are solved. Shcherbinin et al., (2012) used a larger ROI that was expanded by four pixels in all directions than the organ of interest and considered this to correct for PVE as most of the spill-out activity was included in the enlarged ROI.

2.7 Quantification of reconstructed SPECT data

There are a number of literature studies showing the influence of activity distribution, acquisition parameters, camera performance characteristics, reconstruction algorithms, photon attenuation correction and scatter corrections on the quantification accuracy of the volume and activity distribution. In order to study these different phenomena it is necessary to have varying object sizes and positions inside a phantom relative to other organs. This was achieved in different ways. An example, is the simulation study done by Dewaraja et al., (2000) with ^{131}I. In this study an elliptical phantom was used which contained spherical tumours positioned at different locations in relation to the centre position of the phantom. Shcherbinin et al., (2012) used a small 70 ml bottle suspended inside the cylindrical Jaszczak phantom at an off-centre position. Vandervoort et al., (2007) used an elliptical thorax phantom with inserts representing the lungs, heart and spine. In some studies the authors used real patients like the quantification studies done by Willowson et al., (2010) and Zeintl et al., (2010) respectively. The advantages of a variety of phantoms used are discussed under section 2.8. The disadvantage of using different phantoms is that the results are not necessarily applicable to a different experimental setup.

The method in which the SPECT calibration factor is determined can have an influence on the quantification accuracy. Similarly the way of selecting the ROI for obtaining the counts in the organ of interest will have an influence on the quantification accuracy. Therefore it is important to include discussion on these two phenomena.

2.7.1 SPECT calibration factor

Gamma camera sensitivity is defined as the number of counts per seconds that the system obtains for each unit of activity being viewed. This quantity is dependent on the

geometrical efficiency of the collimator, the crystal and the width of the set energy window. The SPECT calibration factor is used to convert image counts in the ROI from the reconstructed images to absolute activity. The calibration factor is radionuclide and gamma camera specific, thus it must be determined for each radionuclide and gamma camera combination (Ritt et al., 2011). Different methods for obtaining the calibration factor have been proposed in literature. These include: a radioactive source in air (Vanhove et al., 2009; Shcherbinin et al., 2008;Koral et al., 1990), using one of the tumours from a phantom study to obtain the calibration factor (Dewaraja et al., 2000), and the use of a large cylindrical phantom to obtain a calibration factor (Zeintl et al., 2010; Soret et al., 2003) The use of a large cylindrical phantom to obtain a calibration factor reduces the PVE mentioned previously. The use of a calibration phantom which is the same size as the tumour results in good accuracy (< 6.5%) as reported by Dewaraja et al., (2000), but this method of obtaining the calibration factor is biased towards quantification accuracy of other tumour sizes. The acquisition and processing parameters for obtaining the calibration factor must be the same as that used for the activity quantification of the organs of interest

Zeintl et al., (2010) proposed a method to determine the SPECT calibration factor, which involved the drawing of a volume of interest (VOI) on the reconstructed images of a large cylindrical phantom and calculating the decay corrected counting rate ($\dot{R}$) in units of counts per minute (cpm) using equation 2-13 (NEMA, 2007):

$$\dot{R} = R\left(\frac{T_0 - T_{cal}}{T_{1/2}}\ln 2\right)\left(\frac{T_{acq}}{T_{1/2}}\ln 2\right)\left(1 - e^{\left(\frac{T_{acq}}{T_{1/2}}\ln 2\right)}\right)^{-1} \qquad \text{2-13}$$

Where R is the counting rate derived from the reconstruction image, T_0 is the start time of the acquisition, T_{cal} is the time of the activity calibration, $T_{1/2}$ is the half-life of the isotope and T_{acq} is the time duration of the acquisition.

The system volume sensitivity (S_{vol}) (in this text referred to as the calibration factor) in units of counts per minute (cpm)/kBq is given by:

$$S_{vol} = \frac{\dot{R} / V_{vol}}{c_A} \qquad 2\text{-}14$$

Where V_{vol} is the volume of the drawn VOI in ml,

c_A is the actual activity concentration in the phantom in units of kBq/ml.

The calculated absolute activity concentration for a specified object size is given by:

$$c_A(j) = \frac{\dot{R}(j) / V_{vol}}{S_{vol} C_E(j,i)} \qquad 2\text{-}15$$

Where $C_E(j,i)$ is the recovery coefficient to correct for the PVE. Equation 2-15 was used by Zeintl et al., (2010) where they measured recovery coefficients for each sphere that was used to represent a tumour.

2.7.2 Influence of Region of Interest on quantification

The counts from the reconstructed images can be obtained by delineating a ROI. The delineation of the ROI can be obtained by drawing the ROI manually on a high resolution fused CT image. Alternatively a threshold method as applied by Shcherbinin et al., (2008) and Vandervoort et al., (2007) can be used, or ROIs can be drawn visually on the reconstructed SPECT images (Brandt et al., 2012) without the aid of the

fused CT image. Pretorius et al., (1993a) has pointed out the limitation of the threshold method in that it is dependent on the organ volume and the pre-processing conditions of the acquired data when used on clinical images. The effects of using a fixed size ROI (i.e. ROI with fixed dimensions be number of pixels or voxels) on quantification accuracy has been studied by Sattarivand et al., (2013) in their tumour response therapy study. This study led them to believe that significant uncertainties in tumour response assessment can be expected.

Other investigators like Bai et al., (2005) have overcome the problem of inter-observer variability of ROI placement by using automatic and objective software in their ROI analysis study. Dewaraja et al., (2000) identified and assessed several factors that affect VOI quantification that includes tissue-background activity, tumour location, radius of rotation and tumour size. They have found that background activity increases VOI counts more in smaller tumours and that there is a slight dependence of VOI counts on the tumour location.

2.8 Discussion

When accurate quantitative SPECT information is required, it is essential to minimize the image degradation which occurs as an integral part of the acquisition and reconstruction of SPECT imaging. Image degrading effects which play an important role in the accuracy of quantitative SPECT include factors such as photon attenuation, photon scatter and partial volume effects (Bailey and Willowson, 2013; Pereira et al., 2010; Tsui et al., 1994a). SPECT image complexities are increased when clinically realistic source distributions are encountered (Ljungberg et al., 1994). The contributions of these effects to quantification accuracy were discussed individually in sections 2.6 and 2.7

Investigations of absolute quantification using either or both phantoms and patients have been carried out by different groups. Zeintl et al., (2010) used standard acquisition protocols to perform ^{99m}Tc SPECT quantification in phantom and patients studies. The authors obtained a mean accuracy of 3.6% (SE, 8.0%) and 1.1% (SE, 8.4%), while Willowson et al., (2008) found an average accuracy of -1% with a range of $\pm$7% between true and measured activity in patient studies done with ^{99m}Tc-MAA. Shcherbinin et al., (2008) reported absolute errors between 3% and 5% in a torso phantom study for the isotopes ^{99m}Tc, ^{123}I, ^{131}I and ^{111}In. The phantom studies done by Shcherbinin et al. were corrected for scatter, attenuation, septal penetration and detector response. In a simulated ^{131}I phantom study done by Dewaraja et al., (2000) an average difference of 3% was obtained when the tumour size and location was changed by the simulation. Koral et al., (1990) studied the effects of variable background activity and close proximity of high organ uptake on the accuracy of tumour quantification. These studies by different groups of researchers showed various levels of accuracy. The accuracies of these studies were dependent on different levels of activity, different shapes and sizes, and different definition of volume of interest on tumour images (Pereira et al., 2010). Lastly it was demonstrated in a multicentre study carried out by Hapdey et al., (2004) that the processing protocols influence the level of quantification accuracy.

These studies mentioned above indicate that more data is needed to increase the credibility of SPECT quantification in NM clinics. It is clear from these studies that evaluation of the specific quantification protocols is necessary for each clinic. The focus of this study will be limited to the application of attenuation correction, scatter correction, detector response correction, iterative reconstruction algorithm parameters and tumour geometry on the quantification accuracy of ^{99m}Tc and ^{123}I. A standard protocol will be used in the evaluation of the quantification accuracy for ^{99m}Tc and ^{123}I in this study.

The aim of this work was to evaluate the influence of the geometry of a radionuclide distribution on SPECT quantification accuracy for ^{99m}Tc and ^{123}I isotopes in an Abdominal Phantom. In order to achieve the aim, the following steps were taken: The preparatory phase of the study was to design and construct an Abdominal Phantom, to verify the accuracy of the attenuation coefficients obtained with the CT scanner, to determine the accuracy of the source calibrator used in this study and to obtain a SPECT calibration factor in order to convert image counts to activity. During the quantification phase the SPECT data was acquired, the influence of not applying scatter correction explicitly was evaluated and the final quantification was performed using a standard reconstruction protocol without post-reconstruction filtering. The influence of different tumour sizes and locations in the Abdominal Phantom relative to a high uptake organ on the quantification accuracy was evaluated. Finally, parameters in the OSEM reconstruction protocol were altered in order to investigate the influence of the selected parameters on the quantified data.

2.9 References

Axelsson, B., Msaki, P., Israelsson, A., 1984. Subtraction of Compton-scattered photons in single-photon emission computerized tomography. J. Nucl. Med. 25, 490–494.

Bai, J., Hashimoto, J., Ogawa, K., Kubo, A., Fukunaga, A., Onozuka, S., Uchida, K., 2005. Influence of photon scattering and attenuation on ROI analysis in brain perfusion single-photon emission tomographic imaging of normal subjects. Annals of Nuclear Medicine 19, 567–572.

Bailey, D.L., Willowson, K.P., 2013. An Evidence-Based Review of Quantitative SPECT Imaging and Potential Clinical Applications. J Nucl Med 54, 83–89.

Boellaard, R., Lingen, A. van, Lammertsma, A.A., 2001. Experimental and Clinical Evaluation of Iterative Reconstruction (OSEM) in Dynamic PET: Quantitative Characteristics and Effects on Kinetic Modeling. J Nucl Med 42, 808–817.

Boussion, N., Cheze Le Rest, C., Hatt, M., Visvikis, D., 2009. Incorporation of wavelet-based denoising in iterative deconvolution for partial volume correction in whole-body PET imaging. European Journal of Nuclear Medicine and Molecular Imaging 36, 1064–1075.

Brambilla, M., Cannillo, B., Dominietto, M., Leva, L., Secco, C., Inglese, E., 2005. Characterization of ordered-subsets expectation maximization with 3D post-reconstruction Gauss filtering and comparison with filtered backprojection in 99mTc SPECT. Ann Nucl Med 19, 75–82.

Brandt, M.P., Kloos, R.T., Shen, D.H., Zhang, X., Liu, Y.-Y., Jhiang, S.M., 2012. Micro-single-photon emission computed tomography image acquisition and quantification of sodium-iodide symporter-mediated radionuclide accumulation in mouse thyroid and salivary glands. Thyroid 22, 617–624.

Brown, S., Bailey, D.L., Willowson, K., Baldock, C., 2008. Investigation of the relationship between linear attenuation coefficients and CT Hounsfield units using radionuclides for SPECT. Applied Radiation and Isotopes 66, 1206–1212.

Bruyant, P.P., 2002. Analytic and Iterative Reconstruction Algorithms in SPECT. J Nucl Med 43, 1343–1358.

Bushberg, J.T., Seibert, J.A., Leidholdt, E.M., Boone, J.M., 2011. The Essential Physics of Medical Imaging. Lippincott Williams & Wilkins.

Buvat, I., Benali, H., Todd-Pokropek, A., Di Paola, R., 1994. Scatter correction in scintigraphy: the state of the art. Eur J Nucl Med 21, 675–694.

Buvat, I., Rodriguez-Villafuerte, M., Todd-Pokropek, A., Benali, H., Paola, R.D., 1995. Comparative Assessment of Nine Scatter Correction Methods Based on Spectral Analysis Using Monte Carlo Simulations. J Nucl Med 36, 1476–1488.

Ceriani, L., Ruberto, T., Delaloye, A.B., Prior, J.O., Giovanella, L., 2010. Three-dimensional ordered-subset expectation maximization iterative protocol for evaluation of left ventricular volumes and function by quantitative gated SPECT: a dynamic phantom study. J Nucl Med Technol 38, 18–23.

Chang, L.-T., 1978. A Method for Attenuation Correction in Radionuclide Computed Tomography. IEEE Transactions on Nuclear Science 25, 638–643.

Chen, C.-H., Muzic, R.F., Nelson, A.D., Adler, L.P., 1999. Simultaneous Recovery of Size and Radioactivity Concentration of Small Spheroids with PET Data. J Nucl Med 40, 118–130.

Cherry, S.R., Sorenson, J.A., Phelps, M.E., 2012. chapter 16 - Tomographic Reconstruction in Nuclear Medicine, in: Phelps, S.R.C.A.S.E. (Ed.), Physics in Nuclear Medicine (Fourth Edition). W.B. Saunders, Philadelphia, pp. 253–277.

Dewaraja, Y.K., Ljungberg, M., Koral, K.F., 2000. Accuracy of 131I Tumor Quantification in Radioimmunotherapy Using SPECT Imaging with an Ultra-High-Energy Collimator: Monte Carlo Study. J Nucl Med 41, 1760–1767.

Dewaraja, Y., Li, J., Koral, K., 1997. Quantitative 131I SPECT with triple energy window Compton scatter correction, in: IEEE Nuclear Science Symposium, 1997. Presented at the IEEE Nuclear Science Symposium, 1997, pp. 1644–1648 vol.2.

Dickson, J., Tossici-Bolt, L., Sera, T., Erlandsson, K., Varrone, A., Tatsch, K., Hutton, B., 2010. The impact of reconstruction method on the quantification of DaTSCAN images. European Journal of Nuclear Medicine and Molecular Imaging 37, 23–35.

Flux, G., Bardies, M., Monsieurs, M., Savolainen, S., Strands, S.-E., Lassmann, M., EANM Dosimetry Committee, 2006. The impact of PET and SPECT on dosimetry for targeted radionuclide therapy. Z Med Phys 16, 47–59.

Frey, E.C., Humm, J.L., Ljungberg, M., 2012. Accuracy and precision of radioactivity quantification in nuclear medicine images. Semin Nucl Med 42, 208–218.

Frey, E.C., Tsui, B.M.W., 1996. A new method for modeling the spatially-variant, object-dependent scatter response function in SPECT, in: , 1996 IEEE Nuclear Science Symposium, 1996. Conference Record. Presented at the , 1996 IEEE Nuclear Science Symposium, 1996. Conference Record, pp. 1082–1086 vol.2.

Fricke, H., Fricke, E., Weise, R., Kammeier, A., Lindner, O., Burchert, W., 2004. A Method to Remove Artifacts in Attenuation-Corrected Myocardial Perfusion SPECT Introduced by Misalignment Between Emission Scan and CT-Derived Attenuation Maps. J Nucl Med 45, 1619–1625.

Gutman, F., Gardin, I., Delahaye, N., Rakotonirina, H., Hitzel, A., Manrique, A., Guludec, D., Véra, P., 2003. Optimisation of the OS-EM algorithm and comparison with FBP for image reconstruction on a dual-head camera: a phantom and a clinical ¹⁸F-FDG study. European Journal of Nuclear Medicine and Molecular Imaging 30, 1510–1519.

Hapdey, S., Soret, M., Ferrer, L., Koulibaly, P.M., Henriques, J., Gardin, I., Darcourt, J., Buvat, I., 2004. Quantification in SPECT: myth or reality? A multi-centric study, in: Nuclear Science Symposium Conference Record, 2004 IEEE. pp. 3170 – 3173 Vol. 5.

Hine GJ, 1967. Instrumentation in Nuclear Medicine. Academic Press inc, New York.

Hudson, H.M., Larkin, R.S., 1994. Accelerated image reconstruction using ordered subsets of projection data. Medical Imaging, IEEE Transactions on 13, 601 –609.

Hutton, B.F., Buvat, I., Beekman, F.J., 2011. Review and current status of SPECT scatter correction. Phys Med Biol 56, R85–112.

Hutton, B.F., Hudson, H.M., Beekman, F.J., 1997. A clinical perspective of accelerated statistical reconstruction. Eur J Nucl Med 24, 797–808.

IAEA, 2014. Quantitative Nuclear Medicine Imaging:Concepts, Requirement and Methods (No. 9), IAEA Human Health. IAEA, Vienna.

Inouye, T., Kose, K., Hasegawa, A., 1989. Image reconstruction algorithm for single-photon-emission computed tomography with uniform attenuation. Phys Med Biol 34, 299–304.

Jaszczak, R.J., 2006. The early years of single photon emission computed tomography (SPECT): an anthology of selected reminiscences. Phys. Med. Biol. 51, R99.

Jaszczak, R.J., Greer, K.L., Floyd, C.E., Harris, C.C., Coleman, R.E., 1984. Improved SPECT Quantification Using Compensation for Scattered Photons. J Nucl Med 25, 893–900.

Kinahan, P.E., Hasegawa, B.H., Beyer, T., 2003. X-ray-based attenuation correction for positron emission tomography/computed tomography scanners. Seminars in Nuclear Medicine 33, 166–179.

Kinahan, P.E., Townsend, D.W., Beyer, T., Sashin, D., 1998. Attenuation correction for a combined 3D PET/CT scanner. Med Phys 25, 2046–2053.

Koral, K.F., Swailem, F.M., Buchbinder, S., Clinthorne, N.H., Rogers, W.L., Tsui, B.M., 1990. SPECT dual-energy-window Compton correction: scatter multiplier required for quantification. J. Nucl. Med. 31, 90–98.

Lazaro, D., El Bitar, Z., Breton, V., Hill, D., Buvat, I., 2005. Fully 3D Monte Carlo reconstruction in SPECT: a feasibility study. Phys Med Biol 50, 3739–3754.

Le Pogam, A., Hatt, M., Descourt, P., Boussion, N., Tsoumpas, C., Turkheimer, F.E., Prunier-Aesch, C., Baulieu, J.-L., Guilloteau, D., Visvikis, D., 2011. Evaluation of a 3D local multiresolution algorithm for the correction of partial volume effects in positron emission tomography. Medical Physics 38, 4920.

Ljungberg, M., King, M.A., Hademenos, G.J., Strand, S.-E., 1994. Comparison of Four Scatter Correction Methods Using Monte Carlo Simulated Source Distributions. J Nucl Med 35, 143–151.

Ljungberg, M., Msaki, P., Strand, S.-E., 1990. Comparison of dual-window and convolution scatter correction techniques using the Monte Carlo method. Phys. Med. Biol. 35, 1099.

Mallard, J.R., 2003. The evolution of medical imaging: from Geiger counters to MRI--a personal saga. Perspect. Biol. Med. 46, 349–370.

Meikle, S.R., Hutton, B.F., Bailey, D.L., Hooper, P.K., Fulham, M.J., 1994. Accelerated EM reconstruction in total-body PET: potential for improving tumour detectability. Phys Med Biol 39, 1689–1704.

Miller, T.R., Wallis, J.W., 1992. Fast Maximum-Likelihood Reconstruction. J Nucl Med 33, 1710–1711.

Müller, S.P., Kijewski, M.F., Moore, S.C., Holman, B.L., 1990. Maximum-likelihood estimation: a mathematical model for quantitation in nuclear medicine. J. Nucl. Med. 31, 1693–1701.

NEMA, 2007. National Electrical Manufacturers Association NU 1 :Perfomance Measurements of Gamma Cameras.

Nuyts, J., Maes, A., Vrolix, M., Schiepers, C., Schelbert, H., Kuhle, W., Bormans, G., Poppe, G., Buxton, D., Suetens, P., Geest, H.D., Mortelmans, L., 1996. Three-Dimensional Correction for Spillover and Recovery of Myocardial PET Images. J Nucl Med 37, 767–774.

Ogawa, K., Harata, Y., Ichihara, T., Kubo, A., Hashimoto, S., 1991. A practical method for position-dependent Compton-scatter correction in single photon emission CT. IEEE Trans Med Imaging 10, 408–412.

Ouyang, J., El Fakhri, G., Moore, S.C., 2008. Improved activity estimation with MC-JOSEM versus TEW-JOSEM in 111In SPECT. Med Phys 35, 2029–2040.

Patton, J.A., Turkington, T.G., 2008. SPECT/CT Physical Principles and Attenuation Correction. J. Nucl. Med. Technol. 36, 1–10.

Pereira, J.M., Stabin, M.G., Lima, F.R.A., Guimarães, M.I.C.C., Forrester, J.W., 2010. Image quantification for radiation dose calculations--limitations and uncertainties. Health Phys 99, 688–701.

Pretorius, P.H., King, M.A., 2009. Diminishing the impact of the partial volume effect in cardiac SPECT perfusion imaging. Med Phys 36, 105–115.

Pretorius, P.H., van Aswegen, A., Lötter, M.G., Herbst, C.P., Nel, M.G., Otto, A.C., 1993a. Verification of a varying threshold edge detection SPECT technique for spleen volume: a comparison with computed tomography volumes. J. Nucl. Med. 34, 963–967.

Pretorius, P.H., van Rensburg, A.J., van Aswegen, A., Lötter, M.G., Serfontein, D.E., Herbst, C.P., 1993b. The channel ratio method of scatter correction for radionuclide image quantitation. J. Nucl. Med. 34, 330–335.

Riauka, T.A., Hooper, H.R., Gortel, Z.W., 1996. Experimental and numerical investigation of the 3D SPECT photon detection kernel for non-uniform attenuating media. Phys Med Biol 41, 1167–1189.

Ritt, P., Vija, H., Hornegger, J., Kuwert, T., 2011. Absolute quantification in SPECT. Eur. J. Nucl. Med. Mol. Imaging 38 Suppl 1, S69–77.

Römer, W., Reichel, N., Vija, H.A., Nickel, I., Hornegger, J., Bautz, W., Kuwert, T., 2006. Isotropic Reconstruction of SPECT Data Using OSEM3D: Correlation with CT. Academic Radiology 13, 496–502.

Rousset, O.G., Ma, Y., Evans, A.C., 1998. Correction for Partial Volume Effects in PET: Principle and Validation. J Nucl Med 39, 904–911.

Sattarivand, M., Caldwell, C., Poon, I., Soliman, H., Mah, K., 2013. Effects of ROI Placement on PET-Based Assessment of Tumor Response to Therapy. International Journal of Molecular Imaging 1–9.

Seo, Y., Aparici, C.M., Cooperberg, M.R., Konety, B.R., Hawkins, R.A., 2010. In vivo tumor grading of prostate cancer using quantitative 111In-capromab pendetide SPECT/CT. J. Nucl. Med. 51, 31–36.

Shcherbinin, S., Celler, A., Belhocine, T., Vanderwerf, R., Driedger, A., 2008. Accuracy of quantitative reconstructions in SPECT/CT imaging. Phys Med Biol 53, 4595–4604.

Shcherbinin, S., Piwowarska-Bilska, H., Celler, A., Birkenfeld, B., 2012. Quantitative SPECT/CT reconstruction for ^{177}Lu and ^{177}Lu/^{90}Y targeted radionuclide therapies. Physics in Medicine and Biology 57, 5733–5747.

Shepp, L.A., Vardi, Y., 1982. Maximum Likelihood Reconstruction for Emission Tomography. IEEE Transactions on Medical Imaging 1, 113–122.

Smith, M.F., Jaszczak, R.J., 1994. Generalized dual-energy-window scatter compensation in spatially varying media for SPECT. Phys Med Biol 39, 531–546.

Soret, M., Koulibaly, P.M., Darcourt, J., Hapdey, S., Buvat, I., 2003. Quantitative accuracy of dopaminergic neurotransmission imaging with (123)I SPECT. J. Nucl. Med. 44, 1184–1193.

Stansfield, E.C., Sheehy, N., Zurakowski, D., Vija, A.H., Fahey, F.H., Treves, S.T., 2010. Pediatric 99mTc-MDP bone SPECT with ordered subset expectation maximization iterative reconstruction with isotropic 3D resolution recovery. Radiology 257, 793–801.

Tamaki, N., Kuge, Y., Tsukamoto, E., 2001. The Road to Quantitation of Regional Myocardial Uptake of Tracer. J Nucl Med 42, 780–781.

Tang, H.R., Brown, J.K., Hasegawa, B.H., 1997. Use of X-ray CT-defined regions of interest for the determination of SPECT recovery coefficients. IEEE Transactions on Nuclear Science 44, 1594–1599.

Tsui, B.M., Frey, E.C., Zhao, X., Lalush, D.S., Johnston, R.E., McCartney, W.H., 1994a. The importance and implementation of accurate 3D compensation methods for quantitative SPECT. Phys Med Biol 39, 509–530.

Tsui, B.M., Zhao, X., Frey, E.C., McCartney, W.H., 1994b. Quantitative single-photon emission computed tomography: basics and clinical considerations. Semin Nucl Med 24, 38–65.

Vandenberghe, S., D'Asseler, Y., Van de Walle, R., Kauppinen, T., Koole, M., Bouwens, L., Van Laere, K., Lemahieu, I., Dierckx, R.A., 2001. Iterative reconstruction algorithms in nuclear medicine. Comput Med Imaging Graph 25, 105–111.

Vandervoort, E., Celler, A., Harrop, R., 2007. Implementation of an iterative scatter correction, the influence of attenuation map quality and their effect on absolute quantitation in SPECT. Phys Med Biol 52, 1527–1545.

Vanhove, C., Defrise, M., Bossuyt, A., Lahoutte, T., 2009. Improved quantification in single-pinhole and multiple-pinhole SPECT using micro-CT information. European Journal of Nuclear Medicine and Molecular Imaging 36, 1049–1063.

Vija, A.H., Hawman, E.G., Engdahl, J.C., 2003. Analysis of a SPECT OSEM reconstruction method with 3D beam modeling and optional attenuation correction: phantom studies, in: Nuclear Science Symposium Conference Record, 2003 IEEE. pp. 2662 – 2666 Vol.4.

Wallis, J.W., Miller, T.R., 1993. Rapidly Converging Iterative Reconstruction Algorithms in Single-Photon Emission Computed Tomography. J Nucl Med 34, 1793–1800.

Warwick, J.M., Rubow, S., du Toit, M., Beetge, E., Carey, P., Dupont, P., 2011. The Role of CT-Based Attenuation Correction and Collimator Blurring Correction in Striatal Spect Quantification. International Journal of Molecular Imaging 2011, 1–9.

Wernick, M.N., Aarsvold, J.N., 2004. Emission Tomography: The Fundamentals of PET and SPECT. Academic Press.

Willowson, K., Bailey, D.L., Bailey, E.A., Baldock, C., Roach, P.J., 2010. In vivo validation of quantitative SPECT in the heart. Clinical Physiology and Functional Imaging 30, 214–219.

Willowson, K., Bailey, D.L., Baldock, C., 2008. Quantitative SPECT reconstruction using CT-derived corrections. Physics in Medicine and Biology 53, 3099–3112.

Zaidi, H. (Ed.), 2005. Quantitative Analysis in Nuclear Medicine Imaging, 1st ed. Springer.

Zaidi, H., Hasegawa, B., 2003. Determination of the attenuation map in emission tomography. J. Nucl. Med. 44, 291–315.

Zeintl, J., Vija, A.H., Yahil, A., Hornegger, J., Kuwert, T., 2010. Quantitative Accuracy of Clinical 99mTc SPECT/CT Using Ordered-Subset Expectation Maximization with 3-Dimensional Resolution Recovery, Attenuation, and Scatter Correction. J Nucl Med 51, 921–928.

Chapter 3

Quantification of ^{99m}Tc SPECT images

CHAPTER 3 3-1

3.1 INTRODUCTION 3-2
3.2 ABDOMINAL PHANTOM DESIGN 3-3
3.3 VERIFICATION OF ATTENUATION COEFFICIENT VALUES OBTAINED FROM CT IMAGES 3-5
3.4 SPECT DATA ACQUISITION 3-8
3.4.1 Acquisition parameters 3-8
3.4.2 Determination of SPECT calibration factor 3-9
3.4.2.1 Evaluation of isotope calibrator accuracy 3-10
3.4.2.2 SPECT calibration factor 3-11
3.4.3 Different tumour sizes and locations 3-12
3.4.4 Matrix size 3-12
3.4.5 Background activity 3-13
3.5 SPECT DATA PROCESSING AND ACTIVITY QUANTIFICATION 3-14
3.5.1 SPECT data reconstruction 3-14
3.5.2 Region of interest selection 3-15
3.5.3 Quantification of the reconstructed SPECT data 3-16
3.5.4 Investigation of selected Flash 3D reconstruction parameters 3-17
3.6 RESULTS 3-19
3.6.1 Verification of attenuation coefficients values obtained from the CT images 3-19
3.6.2 Determination of SPECT calibration factor 3-20
3.6.2.1 Evaluation of isotope calibrator accuracy 3-20
3.6.2.2 SPECT calibration factor 3-20
3.6.3 SPECT quantification for different tumour sizes and locations 3-21
3.6.3.1 Reconstructed SPECT images 3-21
3.6.3.2 Influence of ROI selection on quantification 3-22
3.6.3.3 Influence of matrix size selection on quantification 3-24
3.6.3.4 Influence of scatter and attenuation correction on SPECT quantification 3-25
3.6.3.5 Influence of background activity on SPECT quantification 3-28
3.6.3.6 Influence of Flash 3D reconstruction parameters on quantification 3-29
3.7 DISCUSSION 3-31
3.7.1 Attenuation coefficients values obtained from the CT images 3-31
3.7.2 SPECT Calibration factor 3-31
3.7.3 SPECT quantification for different tumour sizes and locations 3-32
3.7.3.1 Influence of ROI selection and added background on quantification 3-32
3.7.3.2 Influence of matrix size selection on quantification 3-32
3.7.3.3 Influence of scatter and attenuation corrections on SPECT quantification 3-33
3.7.3.4 Effects of Flash-3D reconstruction parameters on quantification 3-34
3.8 CONCLUSION 3-35
3.9 REFERENCES 3-36

3.1 Introduction

In NM, ^{99m}Tc labelled to different pharmaceuticals is used for imaging of various diseases. ^{99m}Tc is readily available at a relatively low cost in the form of a ^{99}Mo (molybdenum-99) generator produced locally by South Africa Nuclear Energy Corporation (NECSA) in Pretoria, South Africa. The usefulness of ^{99m}Tc is attributed to its main γ-ray energy of 140.5 keV (98.6%) which is ideal for imaging using a gamma camera equipped with a NaI(Tl) crystal. The fact that its physical half-life (6.02 hours) is relatively short, leads to fast clearing from the body after the imaging process. This allows for imaging of patients in NM and keeps radiation exposure to patients at relatively low levels.

In this chapter, the proposed standard SPECT quantification procedure is evaluated using ^{99m}Tc. This will be followed by the quantification of ^{123}I SPECT images which will be discussed in chapter 4. ^{99m}Tc was used to perform SPECT activity quantification by using an in-house build Abdominal Phantom to assess the accuracy and reproducibility of the SPECT quantification procedure. SPECT quantification accuracy was determined after correction for the following image degrading factors: photon attenuation, photon scatter and collimator-detector response.

The design of the Abdominal Phantom, verification of the CT attenuation coefficient values as well as the accuracy of the isotope calibrator is discussed in this chapter. A systematic approach was taken to investigate some of the factors affecting tumour quantification. These factors include tumour size, the presence of high activity uptake in a nearby organ, the influence of image matrix size and additional background activity. Likewise, the influence of processing parameters namely: reconstruction algorithm parameters and region of interest (ROI) definition on ^{99m}Tc SPECT quantification accuracy was assessed.

The project was carried out in the NM department, Universitas Academic Hospital, Bloemfontein, South Africa. The Symbia T SPECT/CT (Siemens Medical Solutions Hoffman Estates, IL USA, Inc.) dual head gamma camera with a single slice CT scanner was used for image acquisition. Image processing was performed using the SYNGO software (Siemens Medical Solutions USA, Inc.).

3.2 Abdominal Phantom design

The cylindrical Abdominal Phantom (Figure 3-1), used in this study was designed and built in-house from polyvinyl chloride (PVC) with a wall thickness of 0.5 cm. The phantom had an inner diameter of 30 cm and length of 26 cm. A PVC rod with a diameter of 2 cm that represented a spine like structure was attached on the posterior side in the Abdominal Phantom as shown in Figure 3-1(B) & (C). A hollow fillable structure made out of Perspex was shaped to represent the liver and it was suspended inside the phantom.

Four different sized tumours (Figure 3-2) were made from different sized cylindrical Perspex tubes, each with a filling hole in one end and screw threads on the bottom end. These tumours were defined as tumour I (6.2 cm), tumour II (4.3 cm), tumour III (2.7 cm) and tumour IV (2.2 cm) with their respective diameter values indicated in brackets. These tumours were attached one at a time onto a Perspex rod that protrudes from the base plate of the Abdominal Phantom as shown in Figure 3-1(D). The position of the tumours relative to the liver referred to as tumour-liver distance was varied by sliding the protruding Perspex rod of the Abdominal Phantom in the axial direction. The Abdominal Phantom was filled or drained through the two screw holes in the base plate. The suspended liver insert was filled or drained from the outside of the phantom via two filling tubes.

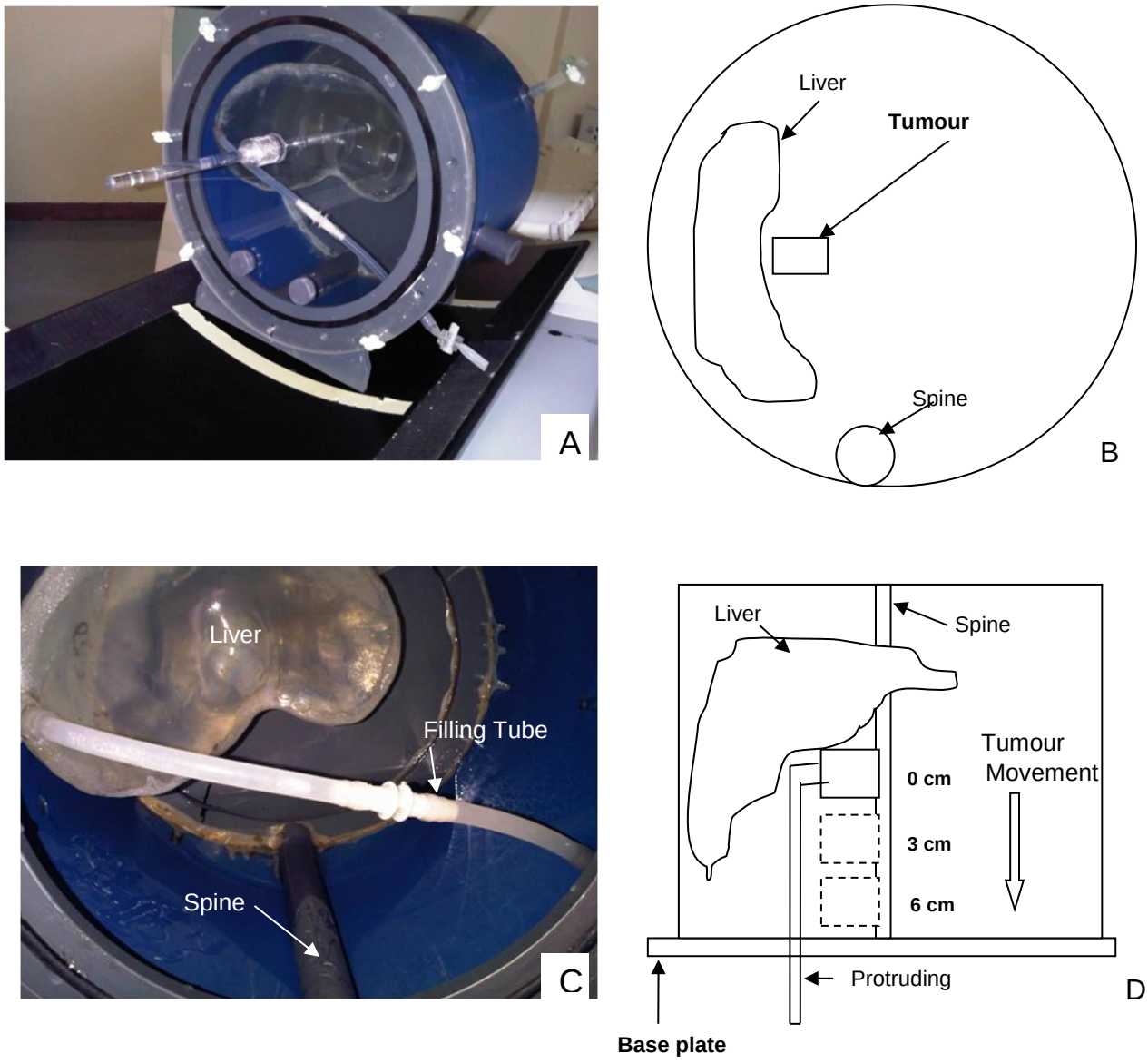

Figure 3-1: *Photograph and sketches of the cylindrical Abdominal Phantom. (A) Abdominal Phantom placed on top of the SPECT/CT couch. (B) A transverse view of the Abdominal Phantom with spine, liver and tumour. (C) The PVC rod representing the spine and the filling tube for the liver. (D) The anterior view of the Abdominal Phantom showing the protruding rod, tumour-liver distances, base plate, liver and spine.*

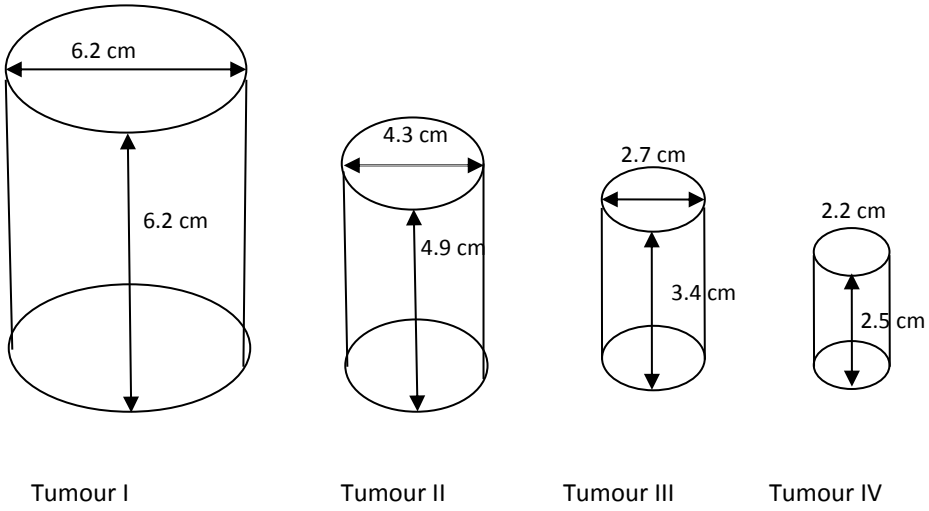

***Figure 3-2**: The four different sized cylinders and their respective inner dimensions representing four tumours.*

3.3 Verification of attenuation coefficient values obtained from CT images

As mentioned in section 2.2, photon attenuation refers to photons that are absorbed or scattered within the medium they are traversing. Photon attenuation affects the accuracy of SPECT activity quantification by decreasing the number of recorded counts. In order to compensate for photon attenuation in this study, an attenuation map was derived from the reconstructed CT images.

It is essential that the Hounsfield units of the reconstructed CT images be transformed to attenuation coefficients of appropriate energy of the radionuclide being used for the SPECT study. This conversion was performed using a bilinear model as explained in section 2.6.1.2.

The Density Phantom (Figure 3-3(A)**)** was used to evaluate the accuracy of the attenuation coefficient values obtained using the CT scanner. The large cylinder of the Deluxe Data Spectrum phantom (Data Spectrum Corporation, Chapel Hill, North Carolina) shown in Figure 3-3(B) was used without the quality assurance inserts (further referred to as the Cylindrical Phantom) as the basis for the Density Phantom. The Cylindrical Phantom has an inner diameter of 21.6 cm, length of 18.7 cm and measured volume of 6852 ml. The Density Phantom consisted of five hollow Perspex cylinders placed inside the Cylindrical Phantom. The five cylinders of the Density Phantom with diameters and lengths of 6.0 cm and 18.6 cm respectively, were filled with different density compounds to simulate soft tissue, lung, and different bone densities. Cylinder 1 was filled with distilled water (simulating soft tissue), while cylinder 2 was filled with Polystyrene (simulating lung tissue). The remaining three cylinders were filled with a mixture of distilled water and di-potassium-hydrogen-phosphate (K_2HPO_4) using the method suggested by White (1977), to formulate three different bone equivalent materials. The different bone densities were simulated by mixing distilled water and K_2HPO_4 in mass ratios of 5:1 (low density bone), 1:1 (medium density bone), and 5:8 (high density bone).

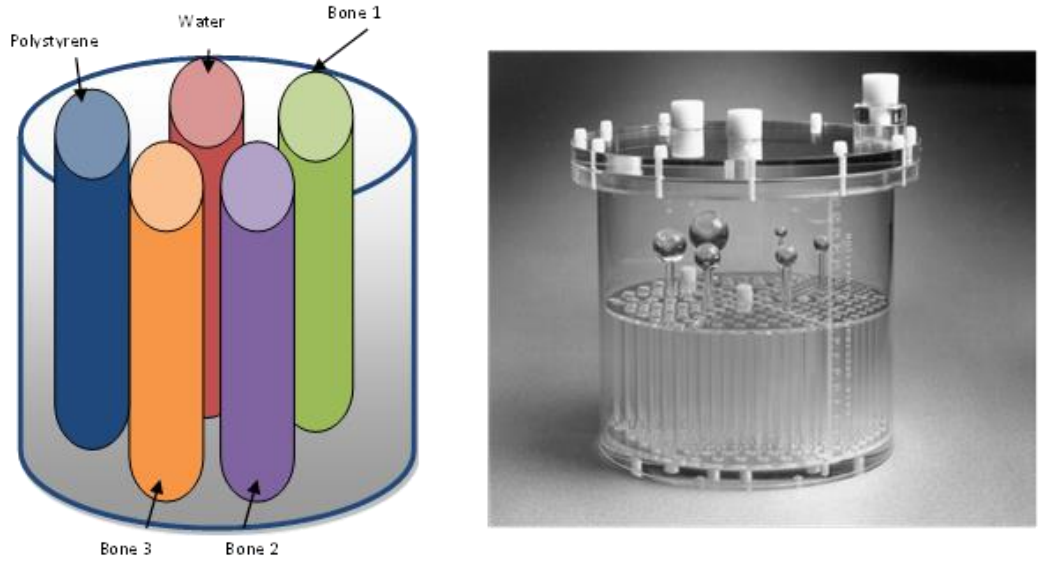

Figure 3-3*: (A) Schematic of the Density Phantom. (B) Data Spectrum Deluxe phantom shown with quality assurance inserts.*

After preparing the five equivalent substitutes (compounds), their corresponding attenuation coefficient values (μ) were calculated by multiplying the measured (or calculated) density and theoretical mass attenuation coefficient for each compound as shown in Table 3-1. It should be noted that the density of polystyrene in Table 3-1 of this study was different from the density of polystyrene published by Hubbell (1982). The density of polystyrene varies widely depending of the particles size used ("MSDS G 605 Gypsum plasters Rhinolite Natural Plus," n.d.). The theoretical mass attenuation coefficient (μ/ρ) of each compound was calculated from the elemental constituents using equation 3-1

$$\mu/\rho = \sum_i w_i (\mu/\rho)_i \qquad 3\text{-}1$$

Where w_i is the proportion by molecular weight and $(\mu/\rho)_i$ is the mass attenuation coefficient of the i^{th} element respectively. The elemental mass attenuation coefficient values $(\mu/\rho)_i$ were derived from published tables (Hubbell, 1982) by plotting a graph of photon energy against mass attenuation coefficient of compound. The straight-line equation was used to interpolate the $(\mu/\rho)_i$ value for ^{99m}Tc energy.

***Table 3-1**: Calculated density and theoretical attenuation coefficient values (μ) for ^{99m}Tc and the different compounds in the Density Phantom.*

Compound	Density ρ (kg.m^{-3})	Theoretical attenuation coefficient values μ (cm^{-1})
Polystyrene	31	4.595 x 10^{-3}
Water	1000	1.555 x 10^{-1}
Bone 1	1153	1.802 x 10^{-1}
Bone 2	1548	2.442 x 10^{-1}
Bone 3	1718	2.720 x 10^{-1}

The Density Phantom filled with the different density compounds was placed on the imaging couch of the SPECT/CT system in order to verify the CT derived attenuation coefficients. CT images of the phantom were acquired using the following imaging parameters: 130 kV, 17 mAs, 512 x 512 matrix sizes and a slice thickness of 5 mm. The acquired CT images (512 x 512 matrix size) were reconstructed with a smoothing kernel to match the resolution of the ^{99m}Tc SPECT images (Shirmohammad et al., 2008). These CT images were down sampled to 128 x 128 image matrix size and the CT Hounsfield numbers were converted to attenuation coefficients of the energy of ^{99m}Tc. As mentioned above a bilinear model was used to scale the reconstructed CT attenuation map to the radionuclide energy of ^{99m}Tc. Circular ROIs were drawn manually on the axial CT slices for each insert of the reconstructed Density Phantom image using the edge visible on the CT image as a guide. The mean attenuation coefficient values and standard deviations were recorded within each ROI. The CT images of the Density Phantom were acquired three times at three different days to assess the accuracy and reproducibility of the CT attenuation coefficients. The data was analysed by comparing the percentage (%) difference (equation 3-2) between the mean measured attenuation coefficient values (m) and the theoretical attenuation coefficient values (c) for each of the five compounds.

$$\%difference = \frac{m-c}{c} \times 100 \qquad 3\text{-}2$$

3.4 SPECT data acquisition

3.4.1 Acquisition parameters

SPECT data was acquired by rotating each of the two gamma camera detectors through 180^0 acquiring 60 projections per detector for all the studies. A step and shoot acquisition mode was used to acquire the SPECT data in a noncircular orbit to improve image resolution and reduce partial volume effects (Frey et al., 2012). The SPECT acquisition parameters are summarized in Table 3-2

***Table 3-2**: SPECT data acquisition parameter used for ^{99m}Tc.*

Radionuclide	^{99m}Tc
Pixel size	0.48 cm
Matrix size	128 x 128
Zoom	1
Acquisition time per projection (s)	20
Parallel hole collimators	Low Energy High Resolution
Scatter correction method	Dual Energy Window
Photo peak	140 keV
Photo peak window width (15%)	129.5 - 150.5 keV
Lower scatter window width (15%)	108.5 - 129.5 keV

A Siemens Dual Energy Window (DEW) scatter correction was applied to the ^{99m}Tc SPECT data. The DEW scatter correction along with the attenuation correction (DEW-CT) was incorporated in the Flash 3D reconstruction algorithm using the CT-derived attenuation map. Routine quality control (QC) of the gamma camera was assessed and the results are shown in Appendix A.

3.4.2 Determination of SPECT calibration factor

In order to assess the accuracy of the absolute activity quantification of the reconstructed SPECT images, a calibration factor is required to convert image counts obtained with the gamma camera to injected activity measured with the isotope calibrator. All the reconstructed SPECT images were corrected for activity decay, photon scatter, photon attenuation and collimator-detector response.

3.4.2.1 Evaluation of isotope calibrator accuracy

The isotope calibrator is utilized to measure the administered activity of radionuclides used for patients undergoing NM studies or radionuclide therapy. It is also used to measure the reference radioactivity during absolute SPECT activity quantification. The accuracy of the isotope calibrator is therefore essential for absolute SPECT activity quantification. The accuracy of the isotope calibrator (Capintec CRC-15R) used in this study was determined as part of an inter hospital isotope calibrator comparison study (Appendix B for detailed methods and results).

As part of the inter hospital comparison study different radionuclide solutions (^{99m}Tc, ^{123}I, ^{131}I, and ^{67}Ga) were placed separately in pre-weighted 5 ml thin walled glass ampoules (Only the results obtained for ^{99m}Tc and ^{123}I are relevant for this investigation). The mass of each solution was determined by weighing the ampoule after filling it to determine the volume of the solution. Each flame-sealed ampoule was measured in the isotope calibrator and the time of each measurement was recorded to determine the activity and activity concentration for each radionuclide sample. All activity measurements were repeated three times and background corrected.

The different radionuclide samples mentioned above were sent to the National Metrology Institute of South Africa (NMISA) for traceable calibration. The accuracy of the isotope calibrator was checked by comparing the decay corrected activity results of NMISA with the isotope calibrator measurements obtained in the clinics. The percentage difference between the activities measured with the dose calibrators and the activities measured by NMISA was utilized for determining the accuracy of the dose calibrators. The accuracy test acceptance limit recommended by the IAEA is ±5%, (IAEA, 2006) The long-lived isotope ^{137}Cs was used to determine the constancy of the isotope calibrator (Appendix C).

3.4.2.2 SPECT calibration factor

The protocol followed for the determination of the SPECT calibration factor was that proposed by Zeintl et al., (2010) as mentioned in section 2.7.1. The Cylindrical Phantom (Figure 3-3) also served as the SPECT calibration phantom. The Cylindrical Phantom was filled with water and the ^{99m}Tc activity (see Table 3-3) was measured with the isotope calibrator (Capintec CRC-15R). The phantom contents were mixed thoroughly to attain a uniform activity concentration throughout the phantom. The lasers of the CT system were used to position the Cylindrical Phantom on the SPECT/CT couch with the centreline of the phantom coinciding with the centre of rotation of the CT. The parameters used for SPECT and CT acquisition were those mentioned in sections 3.3 and 3.4.1. A SPECT calibration factor was determined for each data set for the duration of the study. The SPECT data sets were reconstructed with the Flash 3D iterative reconstruction algorithm employing the standard processing protocol (16 iterations and 8 subsets) with DEW-CT corrections incorporated. No post filtering was applied.

The following times were recorded: time of activity measured in the dose calibrator, the acquisition start time, and the duration of the acquisition. These times were used for decay correction of the SPECT measured counts to the time of isotope calibrator activity measurements.

The reconstructed SPECT and CT images of the Cylindrical Phantom were fused. A ROI was drawn manually to obtain counts from the SPECT image by using the CT image boundaries of the Cylindrical Phantom as a guide. The method of drawing the ROI will be discussed in detail in section 3.5.2 as part of the SPECT quantification process. The SPECT calibration factor S_{vol} (cpm/kBq) was calculated using equation 2-14.

3.4.3 Different tumour sizes and locations

The investigation of the effects of tumour size and location (tumour-liver distance) on quantification was carried out by filling the four different size tumours described in section 3.2, with activities shown in Table 3-3. For this part of the study, no background activity was added to the water in the Abdominal Phantom. The tumours were placed one at a time onto the end of the sliding rod into the water filled Abdominal Phantom. The tumours to liver activity ratios ranged from 1:5 to 1:16, and were based on ratios obtained from clinical ^{123}I-mIBG images in the NM department at Universitas Hospital. The liver activity used for all measurements was 185.0 MBq of ^{99m}Tc. The three different tumour-liver distances as shown in Figure 3-1, were used for each tumour size. The acquisition parameters used were those as described in section 3.4.1. Three data sets were acquired on different days for each tumour size and the three different tumour-liver distances to assess reproducibility.

3.4.4 Matrix size

The effect of matrix size on quantification accuracy was evaluated based on recommendation by Sjörgreen et al., (1996). The authors recommended the use of a larger image matrix size (i.e. smaller pixel size) to improve the accuracy of the quantification results due to improved ROI definition. Furthermore, He and Frey, (2010) has shown that ROI misdefinition (reproducibility of ROI placement onto an image) directly affect the number of pixels included in an object (i.e. number of counts inside an object), and therefore SPECT quantification accuracy relies on counts in each pixel inside a ROI. The assumption was that smaller pixels would have more reproducible and accurate activity quantification than larger pixels for a given ROI. The influence of matrix size on quantification accuracy was assessed by acquiring the SPECT data of the Abdominal Phantom in matrix sizes of 128 and 256 respectively with the same total counts in each case. The acquisitions for the two matrix sizes were done for tumour III (18.5 MBq) at a tumour-liver distance of 0 cm with no liver activity and background

activity. Tumour III was chosen because of its size (diameter 2.7 cm) that was subjected to partial volume effects because its diameter is close to 3 times FWHM of the SPECT spatial resolution (Frey et al., 2012). The acquisition parameters were similar to those described in section 3.4.1. The tumour-liver distance (0 cm) was kept fixed inside the Abdominal Phantom. The Abdominal Phantom was shifted in the axial direction to obtain two different positions (A and B) relative to the gamma camera detectors as indicated in Figure 3-4. These two different positions simulate migration of the ROI through pixels to assess the effect of matrix size on ROI definition.

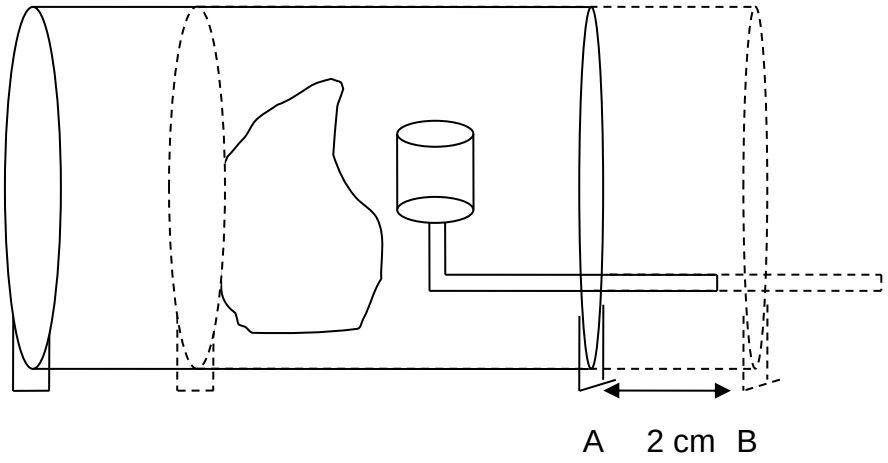

Figure 3-4*: The Abdominal Phantom was moved by 2 cm in the axial direction with respect to the detector from position A to position B, while the tumour inside the Abdominal Phantom was stationary relative to the Abdominal Phantom.*

3.4.5 Background activity

The effect of background activity on the quantification accuracy was assessed by using tumour II. Due to the diameter of tumour II (4.3 cm), it was assumed that partial volume effect would be minimal on the quantification accuracy of tumour II because its diameter is greater than 3 times the FWHM of the SPECT spatial resolution (Frey et al., 2012). The tumour and liver were filled with activities shown in Table 3-3 respectively. Activities

were selected to mimic clinical studies. The two different background activity settings (background 1 and background 2) resulted in percentage activity concentrations of 0.5% and 0.9% of the tumour II activity concentration. The tumour-liver distances used for the acquisition were 0 cm and 6 cm respectively. Acquisition parameters mentioned in section 3.4.1 were used.

***Table 3-3**: ^{99m}Tc activity, activity concentration and organ to background ratio used for the different phantoms.*

Phantom	Activity (MBq)	Concentration (MBq/ml)	Ratio BKG 1	Ratio BKG 2
Cylindrical Phantom	185.0	0.03		
Tumour I	37.0	0.16	16	80
Tumour II	37.0	0.46	46	20
Tumour III	18.5	0.80	80	230
Tumour IV	11.1	0.97	97	485
Liver	185.0	0.15	15	75
Matrix size	18.5	0.80		
Abdominal Phantom-background 1	185.0	0.01		
Abdominal Phantom-background 2	37.0	0.002		

3.5 SPECT data processing and activity quantification

3.5.1 SPECT data reconstruction

The acquired SPECT data in section 3.4.3 was processed using the Flash 3D reconstruction algorithm and two different scenarios. Firstly, the SPECT data was reconstructed using the Flash 3D iterative reconstruction algorithm using only a broad beam Chang attenuation correction referred to as Chang correction. Secondly, the SPECT data was reconstructed with Flash 3D with the DEW-CT correction. This meant that the scatter was corrected for implicitly by the broad beam attenuation correction. This was done to evaluate the influence of the CT attenuation correction along with the DEW scatter correction technique with the standard reconstruction parameters.

The CT attenuation correction and DEW scatter correction are used routinely in the NM department. No post filtering was applied to reconstructed data.

3.5.2 Region of interest selection

The tumours' orientation inside the Abdominal Phantom necessitated the investigation of two different ROI shapes to obtain counts from the reconstructed SPECT data. The two respective ROI shapes (rectangular and circular) were evaluated in the transverse and sagittal views respectively for all the tumours as shown in Figure 3-5. These ROIs were referred to as ROI-R (rectangular) and ROI-C (circular). The delineation around the tumours was done by using the drawing analysis tools of the Syngo workstation as shown in Figure 3-5.

The edges of the reconstructed CT image (Figure 3-5(C) and (D)) were used as a guide to delineate the tumours. The ROI drawn on the central CT slice (axial slice through the largest part of the tumour) was used for delineating the tumours on the reconstructed SPECT images. The fixed size ROI on the central slice was copied to the entire tumour volume for both ROI-R and ROI-C. The activity in each tumour was obtained from the counts within the corresponding ROIs which were converted to activity as discussed in section 3.5.3. It must be noted that data was reconstructed with Flash 3D and DEW-CT correction for obtaining counts from both ROI-R and ROI-C. The suitability of a specific ROI was assessed based on the accuracy of the quantified activity and reproducibility of the results. Based on the results, a specific ROI was chosen for further analysis of the quantification results.

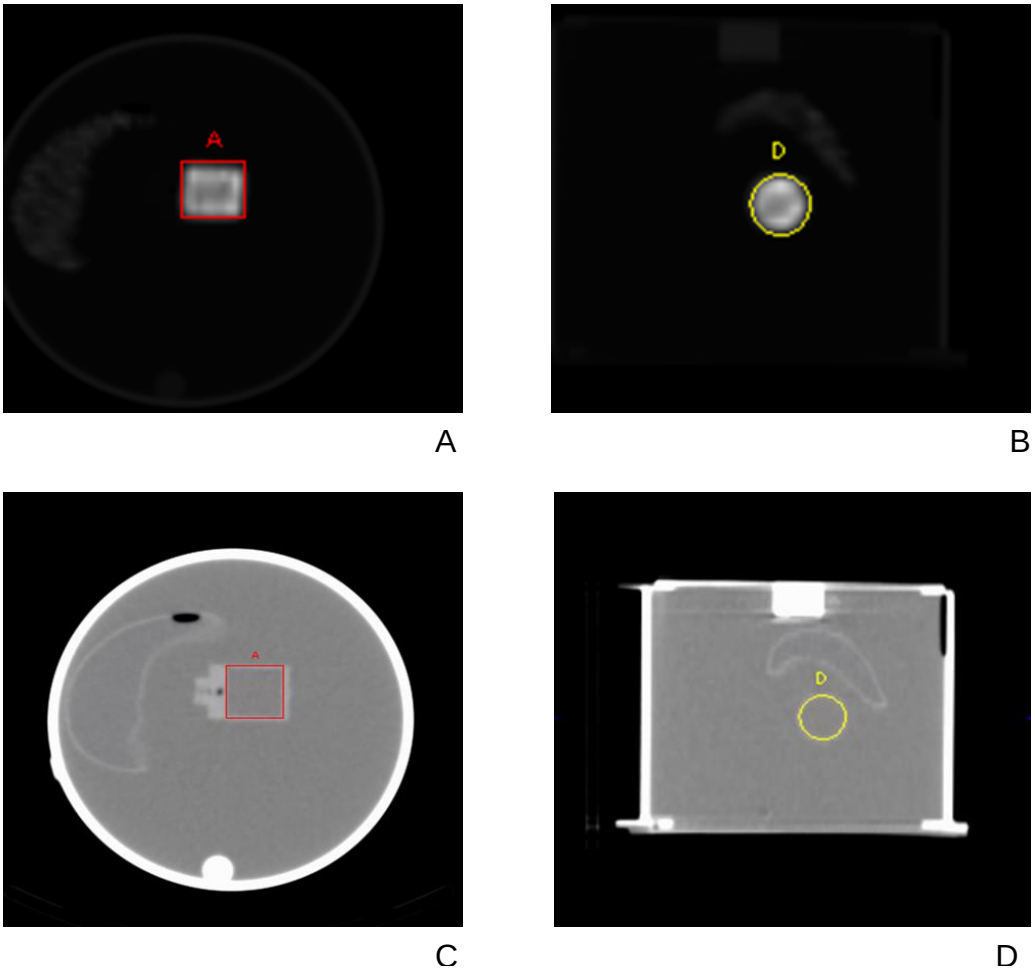

***Figure 3-5**: Two regions of interest used for ROI selection in order to derive counts from the reconstructed SPECT images. (A) Transverse slice of the SPECT image showing the Rectangular ROI (ROI-R). (B) Sagittal slice of the SPECT image showing the Circular ROI (ROI-C). The corresponding CT images used as a guide for drawing ROIs are shown in (C) and (D) for ROI-R and ROI-C respectively*

3.5.3 Quantification of the reconstructed SPECT data

Tumour counts were obtained from the reconstructed SPECT images using ROI-R and ROI-C respectively. The image counts within the ROIs of the different images for each tumour size and tumour-liver distance were converted to activity by using the predetermined SPECT calibration factor. The data was analysed by calculating the percentage (%) difference (equation 3-3) between the quantified activity value (Q) and the true activity value (T). The mean values of the % differences together with the

standard deviations (SD) were reported. The statistical analysis was performed using Windows Microsoft Excel 2010 (Microsoft Corporation, USA) data analysis tool. The statistical significance of the mean % difference as a function of tumour-liver distance was tested using the paired two-tailed t-test (p-value) and the 6 cm tumour-liver distance was used as a reference point for comparison. The statistical significance of the mean % difference as a function of tumour size was tested using the unpaired two tailed t-test. In both cases the statistical significance was accepted at $p < 0.05$ and was rejected at $p > 0.05$.

$$\%difference = \frac{Q - T}{T} \times 100 \qquad 3\text{-}3$$

3.5.4 Investigation of selected Flash 3D reconstruction parameters

In order to evaluate the effect of different reconstruction parameters on the quantification of the tumours, some of the reconstructions in sections 3.4.3 and 3.4.5 were repeated with varying reconstruction Flash 3D parameters and the DEW-CT correction method. These reconstruction parameters were varied according to the number of subsets and iterations used in the reconstruction as shown in Table 3-4. The combination of iterations and subsets was determined by using the number of subsets (S) multiplied with the number of iterations (I) which is referred to as the number of MLEM equivalent iterations (section 2.5.2). A total of seven different MLEM equivalent numbers of iterations was used. The SPECT projection data obtained for tumour IV and II were used for this investigation. These tumours were used for this investigation because they represent a small (influenced by PVE) and a large sized object (not influenced by PVE). SPECT projection data for tumour II were reconstructed with and without added background activity (section 3.4.5), while tumour IV data were only reconstructed without added background activity. All three tumour-liver distances were assessed except where 0.9% background activity was present for tumour II (0 cm and 6 cm).

***Table 3-4**: Number of MLEM equivalent iterations for Flash 3D optimization.*

Subsets (S)	Iterations (I)	MLEM equivalent iterations (S) x (I)
1	8	8
4	4	16
4	8	32
8	8	64
8	16	128
8	20	160
15	30	450

After reconstruction of the SPECT data with the MLEM equivalent iterations in Table 3-4, the appropriate ROI was drawn on the reconstructed sagittal slices as discussed in section 3.5.2 to obtain image counts. The ^{99m}Tc SPECT calibration factor determined in section 3.4.2.2 was used to convert the image counts in the reconstructed sagittal slices to activity. Optimum Flash 3D parameters were determined by calculating the percentage difference between the quantified activity and the true activity according to equation 3.3 and when convergence was attained. Convergence was defined when the quantification difference between two successive iterations was less than 2%. Summary of parameters used in section 3.5 is given in Table 3-5.

***Table 3-5:** Summary for all SPECT data acquisitions and processing procedures for ^{99m}Tc.*

SPECT Acquisition	Phantom	Tumour	Tumour-liver distance
Calibration factor	Cylindrical	-	-
Tumour size & locations	Abdominal	I, II, III & IV	0 cm, 3 cm & 6 cm
Matrix size	Abdominal	III	0 cm
Background activity	Abdominal	II	0 cm & 6 cm

Data processing	Tumour	Reconstruction algorithm	ROI Type
Selection of ROI	I, II, III & IV	Flash 3D	ROI-R & ROI-C
DEW-CT	I, II, III & IV	Flash 3D	ROI-R
Chang correction	I, II, III & IV	Flash 3D	ROI-R
Flash 3D	II & IV	Flash 3D	ROI-R

3.6 Results

3.6.1 Verification of attenuation coefficients values obtained from the CT images

The mean measured and theoretical CT attenuation coefficient values along with the % difference for ^{99m}Tc are shown in Table 3-6. The results indicated that the mean measured attenuation coefficient values were on average lower than the theoretical values except for the values obtained for Polystyrene.

***Table 3-6**: Measured CT attenuation coefficient values (μ) as well as theoretical attenuation coefficient values (μ) are listed for ^{99m}Tc. The percentage differences between these values are also given.*

Compound	Measured attenuation coefficient values (cm^{-1})	Theoretical attenuation coefficient values (cm^{-1})	Percentage difference
Polystyrene	$7.100 \times 10^{-3} \pm 8.9\%$	4.595×10^{-3}	85%
Water	$1.540 \times 10^{-1} \pm 0.2\%$	1.555×10^{-1}	-1.0%
Bone 1	$1.793 \times 10^{-1} \pm 0.3\%$	1.802×10^{-1}	-0.5%
Bone 2	$2.402 \times 10^{-1} \pm 0.3\%$	2.442×10^{-1}	-1.7%
Bone 3	$2.651 \times 10^{-1} \pm 0.5\%$	2.720×10^{-1}	-2.5%

The highest % difference (85%) between the measured and theoretical CT attenuation coefficient values was obtained for Polystyrene which was assumed to represent lung tissue. This large % difference was due to the variable density of commercially available Polystyrene ("density of expanded polystyrene," n.d.). The variable density of commercially available Polystyrene resulted in an uncertainty in the accuracy of calculation of the theoretical attenuation coefficient. All the other measured attenuation coefficient values were within 3% of the theoretical attenuation coefficient values. The small standard deviations (ranging from 0.2% to 0.5%) indicated that the measured attenuation coefficient values obtained with the CT system were stable except for the higher standard deviation value of 8.9% obtained for Polystyrene.

3.6.2 Determination of SPECT calibration factor

3.6.2.1 Evaluation of isotope calibrator accuracy

The results of the survey on accuracy of activity measurements performed with isotope calibrators utilizing ^{99m}Tc, ^{123}I, ^{131}I, and ^{67}Ga are shown in appendix B. For all the measurements, the % difference between the activities measured with the isotope calibrators and the activity values of NMISA was < 0.4%. This was well within the acceptable uncertainty limit of ±5% (IAEA, 2006). The daily constancy check of the isotope calibrator showed an average variation of 0.8% when using a ^{137}Cs source measured at the ^{99m}Tc settings indicating stable functioning of the system. The accuracy and stability of the isotope calibrator ensures that no additional correction factor needs to be introduced in the quantification protocol.

3.6.2.2 SPECT calibration factor

The results for the SPECT calibration factor for ^{99m}Tc are shown in Figure 3-6. These SPECT calibration factor measurements were done over the duration of the study to assess the accuracy and the stability of the gamma camera calibration factor for absolute activity quantification. The average SPECT calibration factor for ^{99m}Tc was 11.0 $\pm$ 0.13 cpm/kBq. The relative SD of 1.2% indicated that the SPECT calibration factor measurements were reproducible.

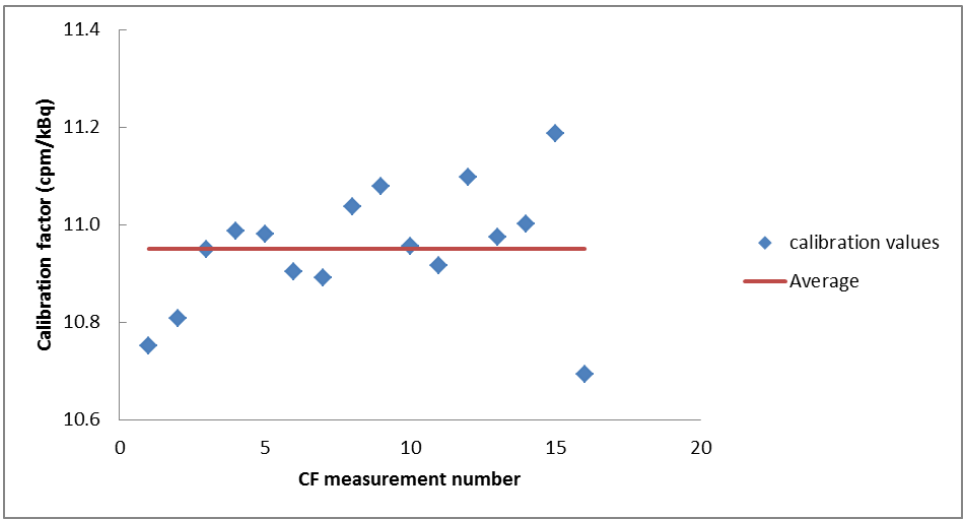

***Figure 3-6**: The variation of the SPECT calibration factor for ^{99m}Tc, measured with the Cylindrical Phantom.*

3.6.3 SPECT quantification for different tumour sizes and locations

3.6.3.1 Reconstructed SPECT images

Figure 3-7 show SPECT images reconstructed with Flash 3D using 16 iteration and 8 subsets. The correction used was the DEW-CT and no post filtering was applied. The images in Figure 3-7 show artifacts in images (A) and (B) that present themselves as unevenness that is due to lack of smoothing/filtering and the edge artifact which is the hot edge and a cold centre. It should be noted that the edge artifact in Figure 3-7(A) and (B) might be due to the impossibility to recover frequencies whose amplitude are too low, therefore the frequency content of the image is incomplete as was observed in a study by Seret et al., (2012). The images (C) and (D) did not show the mentioned artifact due to their size which is close to the gamma camera resolution.

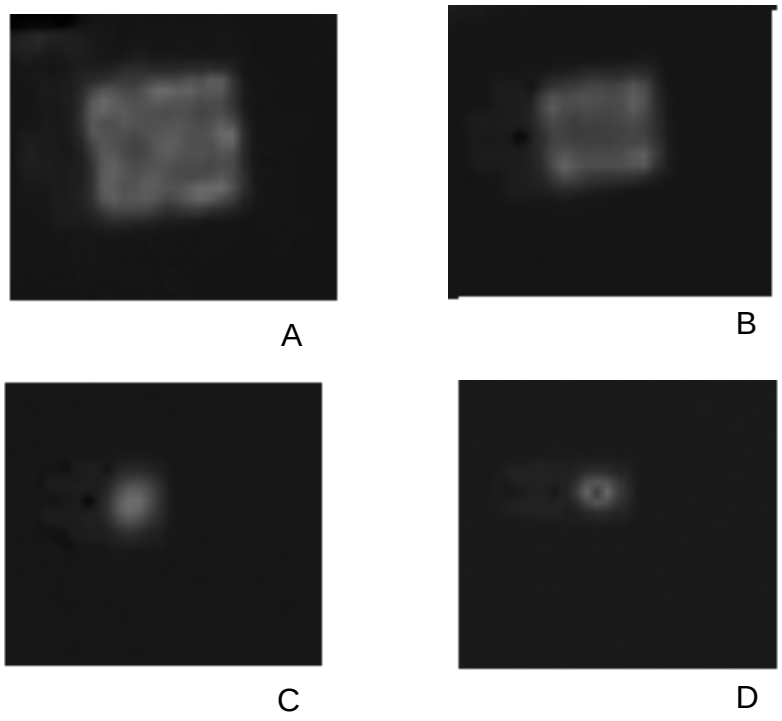

Figure 3-7*: Reconstructed SPECT images obtained with Flash 3D and DEW-CT correction method, (A) Tumour I, (B) Tumour II, (C) Tumour III and (D) tumour IV.*

3.6.3.2 Influence of ROI selection on quantification

The percentage difference between the quantified and true activity values as a function of tumour size and tumour-liver distance for ROI-R and ROI-C were calculated according to equation 3.3 and are shown in Figure 3-8. Figure 3-8(A) shows the results obtained using ROI-R with a mean % difference ranging between -3.1% and 9.4% for all tumour sizes and tumour-liver distances (Appendix D, Table D-2). In contrast, differences between the quantified and the true activity values as obtained with ROI-C (Figure 3-8(B)), resulted in a larger % difference ranging between -13.8% and 3.9% for all tumours sizes and tumour-liver distances (Appendix D, Table D-3).

The smaller tumour sizes III and IV were underestimating the true activity when ROI-C was used. This under estimation of the true activity was not observed when ROI-C was utilized for the larger tumours I and II. This occurrence was consistent with literature when using the CT image to define the tumour ROI. However, when ROI-R was used the quantification accuracy of the smaller tumours III and IV were better than the larger tumours I and II which overestimated the true activity. The mean % difference between the measured and true activity values obtained for ROI-R for large tumour sizes I and II overestimated the measured activity for all tumour-liver distances. For ROI-C only tumour I was overestimating the quantified activity. The smaller tumours sizes III and IV accurately estimated the quantified activity for ROI-R for all tumour-liver distances, while tumours II, III and IV underestimated the quantified activity for ROI-C. The SD values obtained with ROI-C ranged from 0.5% to 6.8% for all the tumour sizes and tumour-liver distances. The corresponding values for ROI-R resulted in SD values ranging from 0.6% to 2.1% for the same tumour sizes and tumour-liver distances. The larger SD values obtained for ROI-C were due to positional variation of the tumour area inside the ROI, which may be partly excluded from the ROI in some instances. Since ROI-R was always bigger than the tumour area, no exclusion was present. The effect of slightly bigger ROI i.e. ROI-R can be seen for smaller tumours III and IV in Figure 3-8(A) with the quantified activity value close to the true activity value (mean % difference being close to zero) as compared to ROI-C (Figure 3-8(B)). It can be seen in Figure 3-8(A) that the quantification results obtained for tumour III and IV using ROI-C have a similar trend as for ROI-R but with a different quantification accuracy.

The choice between ROI-R and ROI-C for this study was based on the accuracy and reproducibility of the SPECT quantification values obtained. ROI–R was chosen due to better overall quantification accuracy and smaller SDs (0.6% to 2.1%). ROI-R was less affected by the spill-out effect due to PVE than ROI-C because most of the spill-out activity was included in ROI-R. Shcherbinin et al., (2012) reported a similar phenomenon in their study when the ROI was expanded by four pixels in all directions to include the majority of spill-out activity.

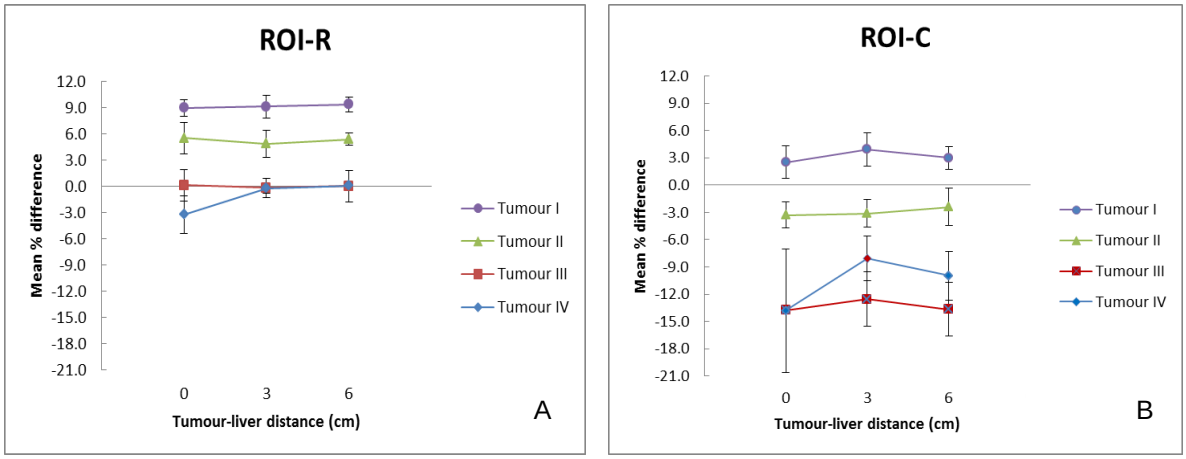

***Figure 3-8**: The mean percentage difference for activity quantification as a function of tumour size, tumour-liver distance and ROI types. (A) Rectangular region of interest (ROI-R). (B) Circular region of interest (ROI-C).*

3.6.3.3 Influence of matrix size selection on quantification

The results for the quantified data for the matrix size and ROI selection obtained for tumour III are shown in Figure 3-9. From the results, it was evident that ROI-R resulted in an overestimation of the true activity by 5% and 7% for the 256 and 128 matrix sizes respectively. On the other hand, ROI-C resulted in an underestimation of 5% and 11% for the 256 and 128 matrix sizes respectively. It can also be seen from Figure 3-9 that there was a modest improvement in the quantification accuracy when using a 256 matrix size (average of 5%) for both ROIs as compared to a 128 matrix size (average of 9%) (Appendix D, Table D-4). This improvement of quantification can be attributed to a more accurate ROI delineation for the 256 imaging matrix than the 128 matrix size (section 3.4.4).

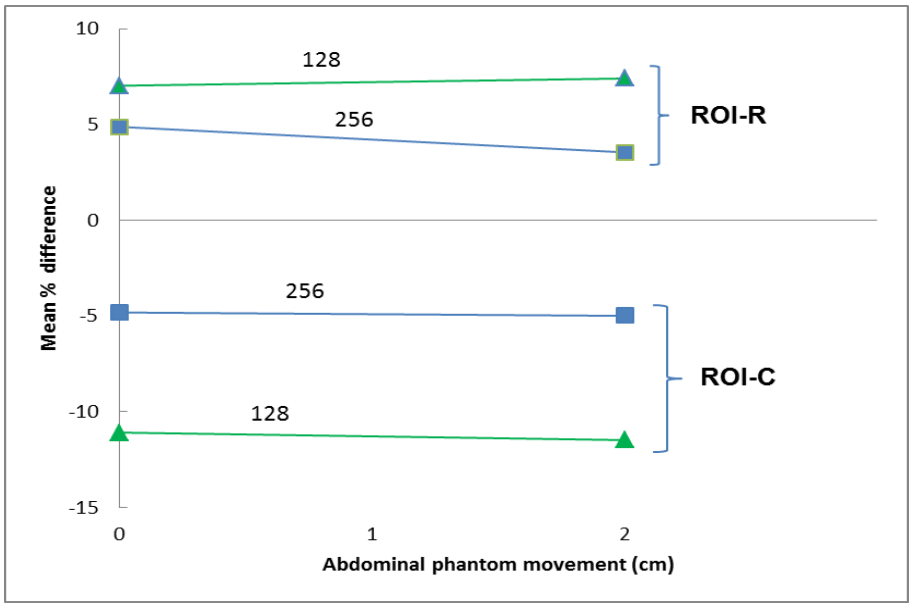

***Figure 3-9**: The mean percentage difference for quantified activity as a function of Abdominal Phantom displacement relative to the detector for tumour III using a 128 x 128 and a 256 x 256 imaging matrix for data acquisition. The data was analysed using the circular (ROI-C) as well as the rectangular (ROI-R) region of interest.*

Although ROI-R overestimated the activity measurement, the difference between the activity values determined with the 128 and 256 imaging matrices respectively was small (2%). On the other hand, values obtained with ROI–C underestimated the activity values due to the PVE (section 3.5.2). It was evident from the results that there was a difference between the results obtained using a 128 and 256 imaging matrices (6% *vs* 2%). This 6% difference obtained when using ROI-C implied that it was better to use a larger imaging matrix (256 x 256) during data acquisition.

3.6.3.4 Influence of scatter and attenuation correction on SPECT quantification

Figure 3-10 shows the results obtained for SPECT activity quantification using the Chang correction and DEW-CT correction respectively.

SPECT activity quantification using the Chang correction

The mean % difference values obtained using the Chang corrections ranged from 30.7% to 14.3% (Appendix D, Table D-1). The Chang correction resulted in an underestimation of the true activity. From these results it was evident that the use of fixed attenuation coefficient values as applied in the Chang correction during the reconstruction of SPECT data resulted in a large underestimation of the true activity for all tumour sizes. This was due to an overestimation of the scatter contribution. The paired two tailed t-test (Appendix E, Table E-1) indicated that there was no significant difference ($p > 0.05$) between the mean % difference value obtained at a tumour-liver distances of 0 cm and 6 cm for tumours I, III and IV with exception of tumour II were there was a significant difference. No significant differences ($p > 0.05$) were obtained between the mean % difference at tumour-liver distances of 3 cm and 6 cm for all tumour sizes.

The unpaired two tailed t-test was used to evaluate the influence of tumour size on the quantification accuracy (Appendix E, Table E-2). A significant difference ($p > 0.05$) was observed in the mean % difference at a tumour-liver distance of 0 cm between tumours I and II, and no significant difference ($p < 0.05$) between tumours II & III and III & IV. There was a significant difference ($p < 0.05$) between the mean % difference of tumour I & II at a tumour-liver distance of 3 cm, while there was no significant difference ($p > 0.05$) for tumours II & III and III & IV. There was no significant difference ($p > 0.05$) in the mean % difference found at a tumour-liver distance of 6 cm between all tumour pairs (i.e. I &II, II & III, III & IV). In general there was no clear pattern of quantification accuracy as function of tumour size.

The largest SD values for the four different sized tumours as a function of tumour-liver distance obtained for the data processed using the Chang correction were 1.9%

(tumour I, 0 cm position), 1.5% (tumour II, 3 cm), 3.4% (tumour III, 3 cm) and 0.6% (tumour IV, 6 cm) respectively (Appendix D, Table D-1).

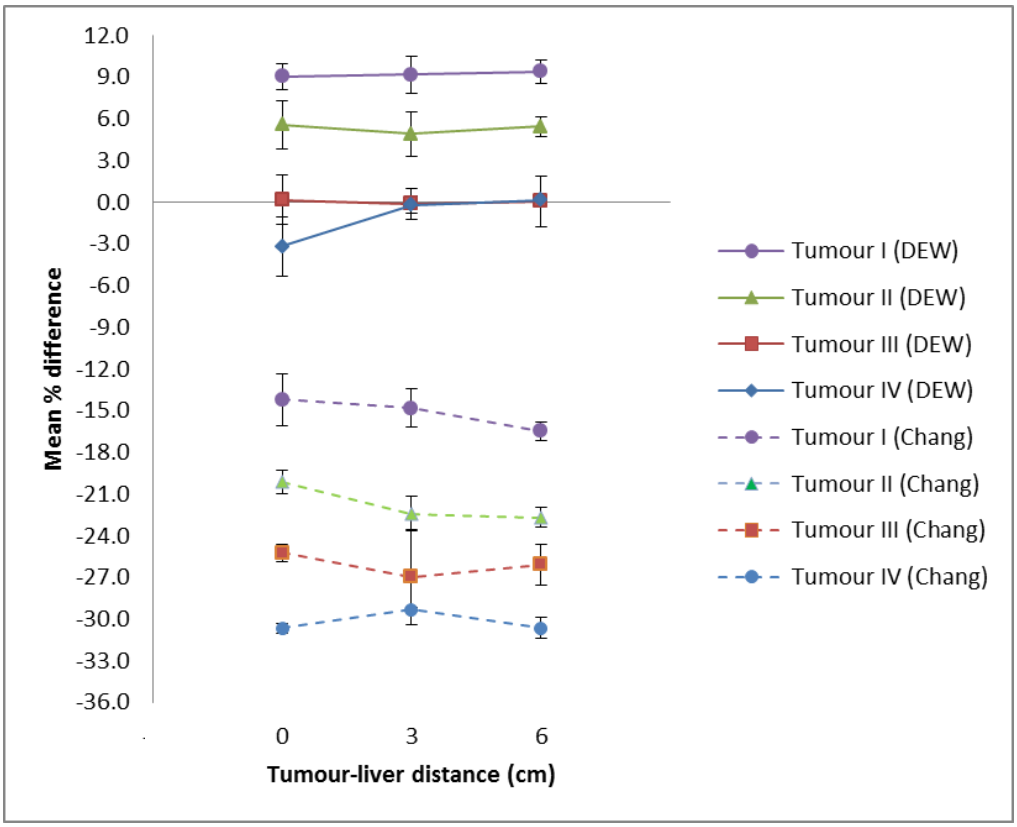

Figure 3-10: *The mean percentage difference between the quantified and true activity values as a function of tumour-liver distance for different tumour sizes. The results are shown for the broad beam attenuation correction (Chang correction) data and DEW scatter and CT narrow beam attenuation corrections (DEW-CT) data. ROI-R was used to obtain the counts from the reconstructed images.*

SPECT activity quantification using the DEW-CT correction

The mean % difference (Figure 3-10) between the quantified and true activity values calculated using the DEW-CT correction ranged from -3.1% to 9.4% (Appendix D, Table D-2). There was no significant difference ($p > 0.05$) in the mean % difference value for each tumour size between the following tumour-liver distances: 0 cm *vs* 6 cm; and

3 cm *vs* 6 cm (Appendix E, Table E-1). It was found that the mean % difference for DEW-CT as a function of tumour size showed a significant difference ($p < 0.05$) between tumour pairs I & II, and II & III for all tumour-liver distances (Appendix E, Table E-2). There was no significant difference ($p > 0.05$) between the mean % differences of tumour size III and IV for all tumour-liver distances.

It can also be seen that the largest SD values for DEW-CT correction for different tumour sizes were 1.3% (tumour I, 3 cm), 2.0% (tumour II, 0 cm), 1.8% (tumour III, 6 cm) and 2.1% (tumour IV, 0 cm) (Appendix D, Table D-2).

Although there was an improvement in the quantified activity values when the DEW-CT correction was used as shown in Figure 3-10, the associated SD values were in the same order as compared to the Chang correction values. However, larger SD might also be due to ROI placement on the tumour that resulted in added counts originating from the liver.

3.6.3.5 Influence of background activity on SPECT quantification

The mean percentage difference between the quantified and true activity for tumour II as a function of tumour-liver distance for different concentrations of background activity in the phantom is shown in Figure 3-11. The results for the 0.5% background activity obtained for tumour II, resulted in mean % differences of 5.3% (0 cm) and 5.1% (6 cm) (Appendix D, Table D-5) as a function of tumour-liver distances of 0 cm and 6 cm respectively. While 0.9% added background resulted in mean % differences for 0 cm and 6 cm tumour-liver distances of 4.1% and 4.2% respectively for tumour II. The results showed a decrease in the mean % difference for both the added background activities as compared to no background activity (5.9% and 5.4% for 0 cm and 6 cm respectively). The statistical analysis however showed that there was no

significant difference p > 0.05 between the mean % difference when no background was added and when 0.5% and 0.9% backgrounds was added respectively (Appendix E, Table E-3). The relative SD values were 0.4% and 1.2% for 0.5% background, while for 0.9% background resulted in relative SD values of 1.3% and 1.1% for tumour-liver distances of 0 cm and 6 cm.

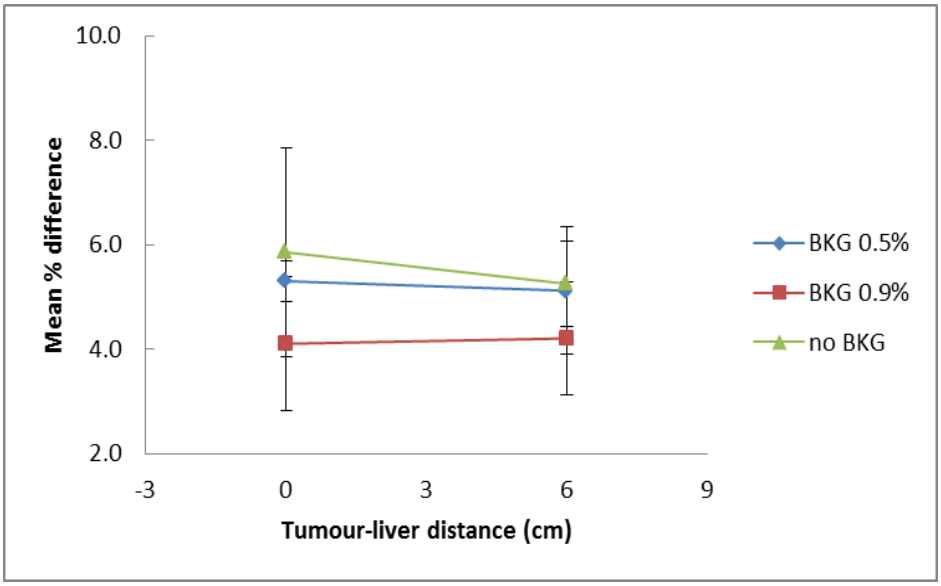

***Figure 3-11**: The mean percentage difference between the quantified and true activity values for tumour II as a function of tumour-liver distance and added background (BKG) activity in the Abdominal Phantom.*

3.6.3.6 Influence of Flash 3D reconstruction parameters on quantification

The mean % difference between the quantified and true activity values for tumour II and IV are plotted as a function of the number of MLEM equivalent iterations (Figure 3-12). From the graph it is evident that increasing the number of MLEM equivalent iterations improved the accuracy of the activity quantification at all three tumour-liver distances for the different tumours (Figure 3-12 (A), (B) and (C)).

The largest underestimation 7% and 27% respectively for tumour II and IV of the quantified activity with no background added activity was at a tumour-liver distance of 0 cm. The convergence of Flash 3D was reach at 64 MLEM equivalent iterations for tumour II and at 128 for the same tumour when added background was present. Convergence for tumour IV was attained at 128 MLEM equivalent iterations (Appendix D, Table D-6, D-7 and D-8).

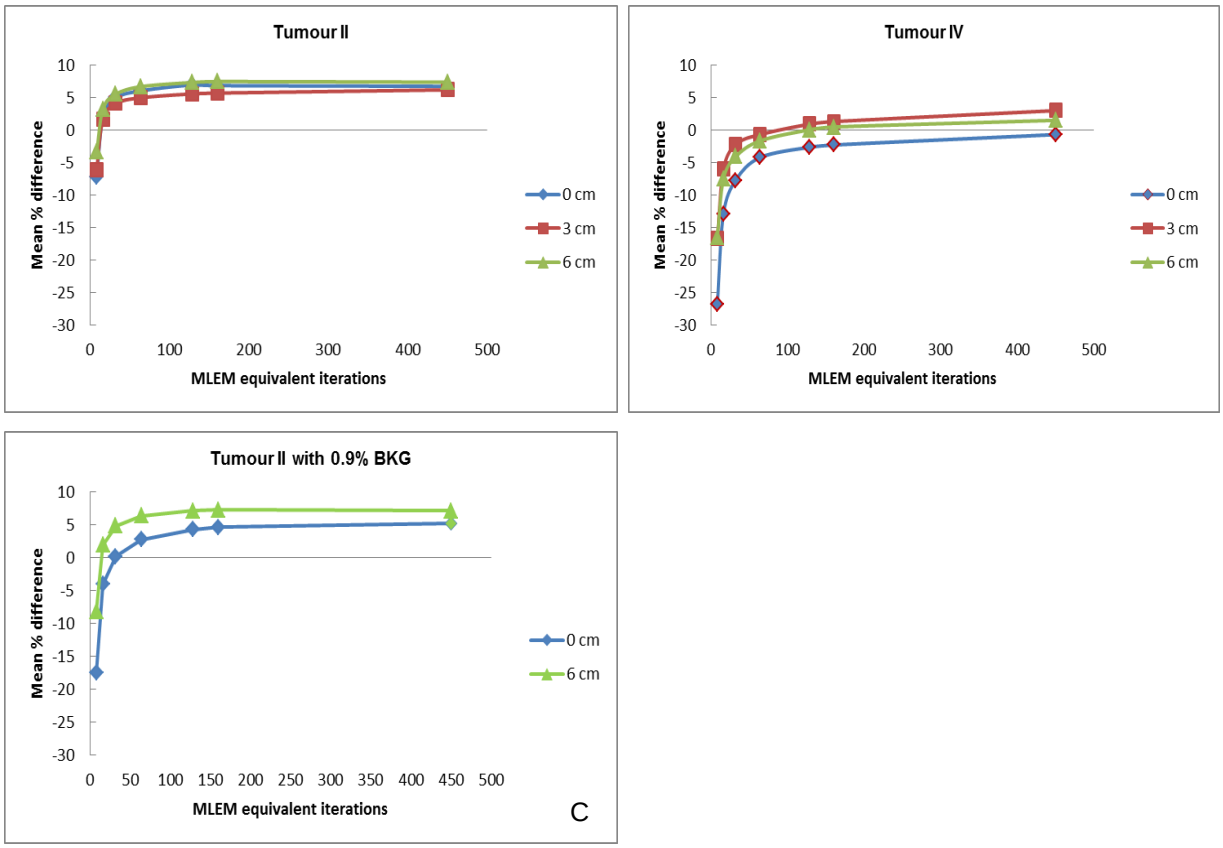

***Figure 3-12**: The mean % difference between the quantified and true activity as a function of the MLEM equivalent iterations at the different tumour-liver distances. No background was added to the Abdominal Phantom for (A) tumour II and (B) tumour IV. (C) Similar data for Tumour II with 0.9% added background (BKG) activity*

3.7 Discussion

3.7.1 Attenuation coefficients values obtained from the CT images

The CT attenuation coefficient results (Table 3-6), for all materials except for Polystyrene showed the mean % differences between the quantified and the theoretical values to be less than 3%. This implies that the conversions from Hounsfield units to attenuation coefficients were done correctly. A large % difference (85%) was observed between the measured and the theoretical attenuation coefficient values for Polystyrene. The reason for this large % difference can be attributed to the large difference between the density values used to calculate the attenuation coefficients for Polystyrene in this project (30.8 kg/m^3) and that used by Hubbell, (1977) (1060 kg/m^3).

Another factor that should be considered is that CT X-rays do not have a mono-energetic beam. The X-ray beam from a CT tube possess a poly-chromatic beam that is hardened as it traverses the attenuation medium and the attenuation coefficient value needs scaling to the radionuclide energy used as mentioned in section 2.6.1.2. NIST values were obtained using a monochromatic X-ray beam (Hubbell, 1982). This can lead to an increase in the errors in the calibration curve (Hasegawa et al., 2002). Shirmohammad et al., (2008) reported in their PET/CT study with the same K_2HPO_4 materials as in this study a bilinear scaling error of 9.1% (bone 1), 3.5% (bone 2) and 2.7% (bone 3) that they attributed to the high effective atomic numbers that result in an increased contribution of the photoelectric interaction process. However, in our study the highest % difference observed for all high density bone equivalent materials was 2.5% (bone 3).

3.7.2 SPECT Calibration factor

The calibration factor obtained, compared well with values reported by Zeintl et al., (2010) who used a similar setup with the same SPECT/CT system. The small relative

SD of 1.2%, which was obtained from the different data sets in our study, indicated that a single calibration factor value could be used if the stability of the gamma camera and isotope calibrator is monitored.

3.7.3 SPECT quantification for different tumour sizes and locations

3.7.3.1 Influence of ROI selection and added background on quantification

It was shown (Figure 3-8) that the shape of the ROI plays an important role in the accuracy of absolute SPECT quantification. The rectangular ROI (ROI-R) that was drawn on the central CT slice of the cylindrical tumour and copied to the reconstructed SPECT data included most of the spill-out image counts. This ROI selection method improved the SPECT activity quantification in the absence of background activity. A SPECT quantification study that used a larger ROI than the object size done by Shcherbinin et al., (2012) obtained similar results. A drawback of using a large ROI is that in the presence of background activity it can result in an overestimation of activity quantification (Sjörgreen et al., 1996). However, as indicated in section 3.6.3.5 of this study, the influence of background activity on quantification did not show significant increase in the quantification value. There are other methods used to correct for partial volume effect in the presence of background activity as discussed by Hofheinz et al., (2012) which is beyond the scope of this study.

3.7.3.2 Influence of matrix size selection on quantification

It was found that the matrix size had a small influence on quantification accuracy (2% in the case of ROI-R) of SPECT studies. The matrix size contributed to the reproducibility of the ROI placement as was observed in section 3.6.3.3. The effect of matrix size on the quantification accuracy is particularly important for small tumours in SPECT imaging

because of the difficulty in delineating the ROI. A larger matrix size (smaller pixel elements) enables the user to define the edges of the tumours more accurate than with a smaller matrix size (larger pixel elements). The disadvantage of using a large matrix size is that the count statistics will be poorer especially in clinical studies, resulting in longer patient imaging times to improve count statistics.

3.7.3.3 Influence of scatter and attenuation corrections on SPECT quantification

The respective quantification results obtained when using Chang correction and DEW-CT correction methods respectively, are consistent with those from literature (Hutton et al., 2011; Shcherbinin et al., 2008). The application of Chang correction tends to underestimate the quantified activity which may be due to incorrect broad beam attenuation correction. In addition, it was observed that the mean % difference did not vary according to the tumour–liver distance when the Chang correction was used. The differences observed between Chang correction and the DEW-CT correction could be due to use of one calibration factor (i.e. with scatter correction and attenuation correction applied).

The application of the DEW-CT correction will reduce the number of photons/counts within the photo peak marginally as was shown. As mentioned previously the use of ROI-R partially corrected for the PVE for both the Chang and DEW-CT corrections. It was suspected that the inclusion of the spill-out counts in the DEW-CT correction resulted in the overestimation of the quantified activity for tumours I and II when ROI-R was used (Figure 3-10). The DEW-CT quantification accuracy for smaller tumours with the exception of tumour IV at a tumour-liver distance of 0 cm was overestimated. This overestimation can be ascribed to under-correction for scatter since the large scatter window may result in an underestimation of the scatter. (Erlandsson et al., 2012) used model based partial volume correction, while Zeintl et al., (2010) used interpolated recovery coefficients derived from correction tables of various spheres sizes.

These recovery coefficients were used to correct for PVE in the presence of background activity or when the high uptake organ is in close proximity.

The studies performed by Luo et al., (1995), Ljungberg et al., (1990) and Koral et al., (1990), showed that if a constant value of k (k=0.5) was used for the DEW scatter correction (Jaszczak et al., 1984) the quantification accuracy was effected by tumour position, size and the reconstruction algorithm. The other factor to consider is that scatter is spatially varying and asymmetric which will influence the accuracy of quantification (Tsui et al., 1994).

3.7.3.4 Effects of Flash-3D reconstruction parameters on quantification

Tumour II with and without added background and tumour IV showed convergence at 128 MLEM equivalent iterations (Appendix D). However, tumour II convergence was also reached at 64 MLEM equivalent iterations without added background compared to 128 for added background. Brambilla et al., (2005) mentioned that the choice of number of iterations is not entirely obvious but rather the selection must be done on case-by-case basis (i.e. based on mean pixel count, acquisition protocol). Yao et al., (2000) reported an observation of the effect of background activity in their study and attributed this phenomenon to increased noise in the reconstructed images, which slowed down the rate of convergence.

3.8 Conclusion

This evaluation shows that SPECT imaging with ^{99m}Tc can be quantitatively accurate with errors of -3.2% to 9.0% when using ^{99m}Tc. The study shows that the accuracy of CT narrow beam attenuation coefficients for different density materials have acceptable errors (2.5%), except for Polystyrene (82.7%). It was also found that ^{99m}Tc SPECT quantification accuracy improved substantially when DEW-CT correction was applied during reconstruction of SPECT data, while the application of Chang correction resulted in quantification accuracy that underestimated the true activity. The tumour size did play a role in the quantification accuracy while the tumour-liver distance did not play a significant role in quantification accuracy when Chang correction was applied. It was observed that the convergence of Flash-3D reconstruction algorithm did not depend on the tumour size and added background for reconstruction parameters employed in this study. From the results, it is evident that the accuracy of SPECT quantification in phantom images depends on the nature of activity distribution within the SPECT field of view and on the specific choice of iterative reconstruction parameters (MLEM equivalent iterations). In order to further reduce quantification errors, the incorporation of partial volume corrections methods during or after the reconstruction process would further improve the quantification accuracy of SPECT studies.

3.9 References

Brambilla, M., Cannillo, B., Dominietto, M., Leva, L., Secco, C., Inglese, E., 2005. Characterization of ordered-subsets expectation maximization with 3D post-reconstruction Gauss filtering and comparison with filtered backprojection in 99mTc SPECT. Ann. Nucl. Med. 19, 75–82.

density of expanded polystyrene [WWW Document], n.d. Expand. Polystyr. EPS-Therm. Install. URL http://www.thermalinstallations.com.au/imagesDB/wysiyg/TDS_Expanded_Polystyrene.pdf (accessed 11.11.14).

Erlandsson, K., Buvat, I., Pretorius, P.H., Thomas, B.A., Hutton, B.F., 2012. A review of partial volume correction techniques for emission tomography and their applications in neurology, cardiology and oncology. Phys. Med. Biol. 57, R119–159.

Frey, E.C., Humm, J.L., Ljungberg, M., 2012. Accuracy and precision of radioactivity quantification in nuclear medicine images. Semin. Nucl. Med. 42, 208–218.

Hasegawa, B.H., Wong, K.H., Iwata, K., Barber, W.C., Hwang, A.B., Sakdinawat, A.E., Ramaswamy, M., Price, D.C., Hawkins, R.A., 2002. Dual-modality imaging of cancer with SPECT/CT. Technol. Cancer Res. Treat. 1, 449–458.

He, B., Frey, E.C., 2010. The impact of 3D volume of interest definition on accuracy and precision of activity estimation in quantitative SPECT and planar processing methods. Phys. Med. Biol. 55, 3535–3544.

Hofheinz, F., Langner, J., Petr, J., Beuthien-Baumann, B., Oehme, L., Steinbach, J., Kotzerke, J., van den Hoff, J., 2012. A method for model-free partial volume correction in oncological PET. EJNMMI Res. 2, 16.

Hubbell, J.H., 1982. Photon mass attenuation and energy-absorption coefficients. Int. J. Appl. Radiat. Isot. 33, 1269–1290.

Hubbell, J.H., 1977. Photon Mass Attenuation and Mass Energy-Absorption Coefficients for H, C, N, O, Ar, and Seven Mixtures from 0.1 keV to 20 MeV. Radiat. Res. 70, 58–81.

Hutton, B.F., Buvat, I., Beekman, F.J., 2011. Review and current status of SPECT scatter correction. Phys. Med. Biol. 56, R85–112.

IAEA, 2006. Quality Assurance for Radioactivity Measurement in Nuclear Medicine. (Technical report No. 454). International Atomic Energy Agency, Vienna.

Jaszczak, R.J., Greer, K.L., Floyd, C.E., Harris, C.C., Coleman, R.E., 1984. Improved SPECT Quantification Using Compensation for Scattered Photons. J. Nucl. Med. 25, 893–900.

Koral, K.F., Swailem, F.M., Buchbinder, S., Clinthorne, N.H., Rogers, W.L., Tsui, B.M., 1990. SPECT dual-energy-window Compton correction: scatter multiplier required for quantification. J. Nucl. Med. Off. Publ. Soc. Nucl. Med. 31, 90–98.

Ljungberg, M., Msaki, P., Strand, S.-E., 1990. Comparison of dual-window and convolution scatter correction techniques using the Monte Carlo method. Phys. Med. Biol. 35, 1099.

Luo, J.Q., Koral, K.F., Ljungberg, M., Floyd, C.E., Jr, Jaszczak, R.J., 1995. A Monte Carlo investigation of dual-energy-window scatter correction for volume-of-interest quantification in 99Tcm SPECT. Phys. Med. Biol. 40, 181–199.

MSDS G 605 Gypsum plasters Rhinolite Natural Plus [WWW Document], n.d. . MSDS G605 Gypsum Plasters Rhinolite Nat. Plus. URL http://www.gyproc.co.za/media/85845/MSDS%20G%20605%20Gypsum%20plasters%20_Rhinolite%20Natural%20Plus_.pdf (accessed 2.19.15).

Seret, A., Nguyen, D., Bernard, C., 2012. Quantitative capabilities of four state-of-the-art SPECT-CT cameras. EJNMMI Res. 2, 45.

Shcherbinin, S., Celler, A., Belhocine, T., Vanderwerf, R., Driedger, A., 2008. Accuracy of quantitative reconstructions in SPECT/CT imaging. Phys. Med. Biol. 53, 4595–4604.

Shcherbinin, S., Piwowarska-Bilska, H., Celler, A., Birkenfeld, B., 2012. Quantitative SPECT/CT reconstruction for ^{177}Lu and ^{177}Lu/^{90}Y targeted radionuclide therapies. Phys. Med. Biol. 57, 5733–5747.

Shirmohammad, M., Ay, M.R., Sarkar, S., Ghadiri, H., Rahmim, A., 2008. Comparative assessment of different energy mapping methods for generation of 511-keV attenuation map from CT images in PET/CT systems: A phantom study, in: 5th IEEE International Symposium on Biomedical Imaging: From Nano to Macro,

2008. ISBI 2008. Presented at the 5th IEEE International Symposium on Biomedical Imaging: From Nano to Macro, 2008. ISBI 2008, pp. 644–647.

Sjörgreen, K., Ljungberg, M., Strand, S.E., 1996. Parameters influencing volume and activity quantitation in SPECT. Acta Oncol. Stockh. Swed. 35, 323–330.

Tsui, B.M., Frey, E.C., Zhao, X., Lalush, D.S., Johnston, R.E., McCartney, W.H., 1994. The importance and implementation of accurate 3D compensation methods for quantitative SPECT. Phys. Med. Biol. 39, 509–530.

White, D.R., 1977. The formulation of tissue substitute materials using basic interaction data. Phys. Med. Biol. 22, 889–899.

Yao, R., Seidel, J., Johnson, C.A., Daube-Witherspoon, M.E., Green, M.V., Carson, R.E., 2000. Performance characteristics of the 3-D OSEM algorithm in the reconstruction of small animal PET images. Ordered-subsets expectation-maximixation. IEEE Trans. Med. Imaging 19, 798–804.

Zeintl, J., Vija, A.H., Yahil, A., Hornegger, J., Kuwert, T., 2010. Quantitative Accuracy of Clinical 99mTc SPECT/CT Using Ordered-Subset Expectation Maximization with 3-Dimensional Resolution Recovery, Attenuation, and Scatter Correction. J. Nucl. Med. 51, 921–928.

Chapter 4

Quantification of ^{123}I SPECT images

CHAPTER 4 4-1

4.1 INTRODUCTION 4-2
4.2 VERIFICATION OF ATTENUATION COEFFICIENT VALUES OBTAINED FROM CT IMAGES 4-2
4.3 SPECT DATA ACQUISITION 4-3
4.3.1 Acquisition parameters 4-3
4.3.2 SPECT calibration factor 4-4
4.3.3 Different tumour sizes and locations 4-5
4.4 SPECT DATA PROCESSING AND ACTIVITY QUANTIFICATION 4-5
4.4.1 SPECT data reconstruction 4-5
4.4.2 Quantification of the reconstructed SPECT data 4-6
4.4.3 Investigation of selected Flash 3D reconstruction parameters 4-6
4.5 RESULTS 4-7
4.5.1 Verification of attenuation coefficient values obtained from the CT images 4-7
4.5.2 SPECT calibration factor 4-8
4.5.3 SPECT quantification for different tumour sizes and locations 4-8
4.5.3.1 Reconstructed SPECT images 4-8
4.5.3.2 Influence of scatter and attenuation correction on SPECT quantification 4-9
4.5.3.3 Influence of Flash 3D reconstruction parameters on quantification 4-12
4.6 DISCUSSION 4-13
4.6.1 Attenuation coefficient values obtained from the CT images 4-13
4.6.2 SPECT calibration factor 4-13
4.6.3 SPECT quantification for different tumour sizes and locations 4-14
4.6.3.1 Influence of scatter and attenuation corrections on SPECT quantification 4-14
4.6.3.2 Effects of Flash 3D reconstruction parameters on quantification 4-15
4.7 CONCLUSION 4-16
4.8 REFERENCES 4-17

4.1 Introduction

A regularly used radionuclide in NM for tumour detection is ^{123}I with a half-life of 13.2 hours. ^{123}I emits a gamma ray of 159 keV which is useful in imaging with a gamma camera with a NaI(Tl) crystal. The ^{123}I availability is through cyclotron production at iThemba labs based in Cape Town South Africa, with once a week delivery to NM departments. The half-life of ^{123}I makes it ideal for 24 hours distribution studies. Iodine-123 can be labelled to Metaiodobenzylguanidine (mIBG) that localizes in the adrenergic tissue. Thus ^{123}I-mIBG can be used to locate neuro- endocrine tumours and to determine the radiation dose that will be obtained when administering therapeutic ^{131}I-mIBG doses (IAEA, 2008).

The ^{99m}Tc quantification protocol evaluated in chapter 3 will be implemented for ^{123}I SPECT quantification in this chapter. The attenuation coefficient values obtained for ^{123}I using the CT of the SPECT/CT system were validated. The different factors affecting the quantification accuracy of SPECT imaging which were investigated in Chapter 3 were evaluated using the same Abdominal Phantom. These factors include tumour size, the presence of high activity uptake in a nearby organ, the application of the Chang attenuation correction, the application of the TEW scatter correction combined with narrow beam attenuation correction (TEW-CT), and lastly the iterative reconstruction algorithm parameters.

4.2 Verification of attenuation coefficient values obtained from CT images

The method used for verification of the CT attenuation coefficient values for ^{123}I was similar to what was described in section 3.3 for ^{99m}Tc. The Density Phantom (Figure 3-3(A)) was used to evaluate the accuracy of the CT attenuation coefficient values scaled to ^{123}I energy. The calculated density values and the theoretical

attenuation coefficient values of the compounds for ^{123}I are shown in Table 4-1. The data was analysed by following a similar method as described in section 3.3 for calculating the mean percentage difference and standard deviation (SD) values.

Table 4-1: *Calculated density and theoretical attenuation coefficient values (μ) for ^{123}I and the different compounds in the Density Phantom.*

Compound	Density ρ (kgm^{-3})	Theoretical attenuation coefficient values μ (cm^{-1})
Polystyrene	31	4.363 x 10^{-3}
Water	1000	1.471 x 10^{-1}
Bone 1	1153	1.687 x 10^{-1}
Bone 2	1548	2.244 x 10^{-1}
Bone 3	1718	2.483 x 10^{-1}

4.3 SPECT data acquisition

4.3.1 Acquisition parameters

The SPECT data was acquired as explained in section 3.4.1. The data acquisition parameters are shown in Table 4-2. For ^{123}I, the modified TEW scatter correction method (i.e. the scatter windows used were 24 keV wide instead of 3 keV as initially proposed by Ogawa et al., (1991)) and medium energy general purpose (MEGP) collimators were used to acquire the data instead of the DEW scatter correction method and LEHR collimators. The TEW scatter correction was used because ^{123}I emits additional high energy photons (529 keV, 1.4%) which may contaminate the counts in the main photo peak centred at 159 keV. The MEGP collimator was employed because it limits the septal penetration of 159 keV as well as contamination from higher energy photons of ^{123}I and thus improves image contrast (Edwards and Zhuang, 2014; Moore

et al., 2012; Snay et al., 2011). The attenuation correction map was generated from CT image data as explained in section 4.2.

***Table 4-2**: SPECT data acquisition parameters used for ^{123}I.*

Radionuclide	^{123}I
Pixel size	0.48 cm
Matrix size	128 x 128
Zoom	1
Acquisition time per projection (s)	20
Parallel hole collimators	Medium Energy General Purpose
Scatter correction method	Triple Energy Window
Photo peak	159 keV
Photo peak window width (15%)	147 - 171 keV
Lower scatter window width (15%)	123 - 147 keV
Upper scatter window width (15%)	171 – 195 keV

4.3.2 SPECT calibration factor

Similar to the ^{99m}Tc study in chapter 3, the accuracy of the isotope calibrator was determined for ^{123}I. A SPECT calibration factor was calculated to enable the user to convert counts from SPECT images to activity values. The same methods were followed as those described in section 3.4.2. The evaluation of the accuracy of the isotope calibrator for ^{123}I was performed as part of the project mentioned in section 3.4.2.1 (See Appendix B for detailed methods and results). The accuracy was determined using a ^{123}I source that was calibrated by NMISA. A constancy check for the ^{123}I setting was performed using the ^{137}Cs reference source (Appendix C).

A SPECT calibration factor was determined with 158.0 ± 4.1 MBq of ^{123}I mixed with water in the Cylindrical Phantom (Figure 3-3). SPECT data of the Cylindrical Phantom

was acquired using the Siemens Symbia SPECT/CT gamma camera. The data were reconstructed using the Siemens Flash 3D iterative reconstruction method (8 subsets and 16 iterations) by employing the TEW-CT correction method. No post filtering was applied.

4.3.3 Different tumour sizes and locations

The Abdominal Phantom was used with the activities shown in Table 4-3. The Abdominal Phantom contained water with no background activity. Data were acquired by following the method described in section 3.4.3 using the ^{123}I parameters in Table 4-2.

Table 4-3: *^{123}I activity and activity concentration used for the different phantoms.*

Phantom	Activity (MBq)	Concentration (MBq/ml)
Cylindrical Phantom	158	0.02
Tumour I	39.2	0.17
Tumour II	37.6	0.47
Tumour III	18.4	0.80
Tumour IV	12	1.04
Liver	179	0.15

4.4 SPECT data processing and activity quantification

4.4.1 SPECT data reconstruction

The SPECT data were processed using Flash 3D with the two different scenarios discussed in section 3.5.1. In the first scenario, the data were reconstructed using

Chang correction. Secondly, the data were reconstructed with the TEW-CT. No post filtering was applied to the data.

4.4.2 Quantification of the reconstructed SPECT data

Tumour counts were obtained from the reconstructed SPECT images using ROI-R (as defined in section 3.5.2). The ^{123}I SPECT calibration factor was used to convert the image counts from the reconstructed tumour images to activity values. The percentage (%) difference between the quantified activity value (Q) and the true activity value (T) was calculated using equation 3-3. The mean % difference and SD for each quantified tumour activity value were determined. The statistical significance of the mean % difference as a function of a tumour size was tested using the unpaired two tailed t-test and tumour-liver distance using the paired two tailed t-test. As in section 3.5.3, the statistical significance was accepted at $p < 0.05$ and was rejected at $p > 0.05$.

4.4.3 Investigation of selected Flash 3D reconstruction parameters

The acquired SPECT projection data in section 4.3.3 were used for the optimization of the Flash 3D reconstruction algorithm parameters. Data acquired using tumour IV and II at the three different tumour-liver distances were used for this investigation. As mentioned in section 3.5.4, tumour II and IV were used for this investigation because they represented a small (influenced by PVE) and a large sized object (not influenced by PVE). The number of subsets and iterations were varied according to Table 3-4 in section 3.5.4. As in chapter 3 optimum Flash 3D parameters were determined by calculating the % difference between the quantified activity and the true activity according to equation 3-3. Convergence was defined when the value of the quantification difference between two successive MLEM equivalent iterations was less

than 2%. SPECT data acquisition and processing procedures is summarized and given in Table 4-4.

***Table 4-4**: Summary for all SPECT data acquisitions and processing procedures for ^{123}I.*

SPECT Acquisition	**Phantom**	**Tumour**	**Tumour-liver distance**
Calibration factor	Cylindrical	-	-
Tumour size & locations	Abdominal	I, II, III & IV	0 cm, 3 cm & 6 cm
Data processing	**Tumour**	**Reconstruction algorithm**	**ROI Type**
TEW-CT	I, II, III & IV	Flash 3D	ROI-R
Chang correction	I, II, III & IV	Flash 3D	ROI-R
Flash 3D parameters	II & IV	Flash 3D	ROI-R

4.5 Results

4.5.1 Verification of attenuation coefficient values obtained from the CT images

The average measured attenuation coefficient values obtained for ^{123}I are shown in Table 4-5. The measured attenuation coefficient values compared favourably with the theoretical values except for Polystyrene which overestimated the theoretical value (65%). This large % difference was mainly due to the variable density of available polystyrene (“density of expanded polystyrene,” n.d.) as mentioned in section 3.6.1. The remaining differences were smaller than 2% and their associated SD values were less than 1%.

Table 4-5: *Measured CT attenuation coefficient (μ) values as well as theoretical attenuation coefficient (μ) values are listed for ^{123}I. The percentage differences between these values are also given.*

Compound	Measured attenuation coefficient values (cm^{-1})	Theoretical attenuation coefficient values (cm^{-1})	Percentage difference
Polystyrene	$7.220 \times 10^{-3} \pm 10\%$	4.363×10^{-3}	65
Water	$1.470 \times 10^{-1} \pm 0.4\%$	1.471×10^{-1}	0.0
Bone 1	$1.706 \times 10^{-1} \pm 0.3\%$	1.687×10^{-1}	1.1
Bone 2	$2.251 \times 10^{-1} \pm 0.2\%$	2.244×10^{-1}	0.3
Bone 3	$2.474 \times 10^{-1} \pm 0.4\%$	2.483×10^{-1}	-0.3

4.5.2 SPECT calibration factor

The isotope calibrator was found to be underestimating the true activity value for ^{123}I by 5.2% (Appendix B, Isotope calibrator 3). This was however slightly above the uncertainty limit of ±5**%** (IAEA, 2006) and it did not necessitate the use of correction factor. The daily constancy check of the isotope calibrator showed a variation of 0.1% when using the ^{137}Cs reference source at the ^{123}I setting. The average SPECT calibration factor determined for ^{123}I was 10.8 ± 0.3 cpm/kBq. The relative SD of 2.8% showed that the SPECT calibration factors which were determined during the study were reproducible.

4.5.3 SPECT quantification for different tumour sizes and locations

4.5.3.1 Reconstructed SPECT images

Figure 4-1 show SPECT images reconstructed with Flash 3D using 16 iteration and 8 subsets. The correction used was the TEW-CT and no post filtering was applied. The images in Figure 4-1 show similar artifacts in images (A) and (B) as those mentioned in section 3.6.3.1; the unevenness that is due to lack of smoothing/filtering and the edge artifact. As mentioned in section 3.6.3.1 the edge artifact in Figure 4-1(A) and (B) might

be due to the impossibility to recover frequencies whose amplitude are too low. The images (C) and (D) did not show the mentioned artifact due to their size which is close to the gamma camera resolution.

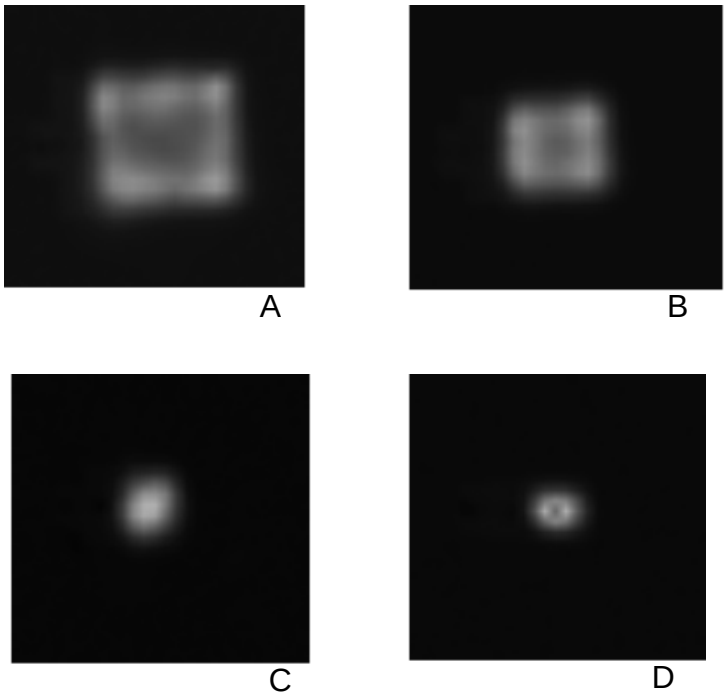

Figure 4-1: Reconstructed SPECT images obtained with Flash 3D and TEW-CT correction method, (A) Tumour I, (B) Tumour II, (C) Tumour III and (D) tumour IV.

4.5.3.2 Influence of scatter and attenuation correction on SPECT quantification

The results obtained with the Chang and the TEW-CT corrections are shown in Figure 4-2.

SPECT activity quantification using the Chang correction

The results obtained with the Chang correction showed a similar trend as was observed in Figure 3-8, where the true activity was underestimated for all tumours sizes and tumour-liver distances. The mean % difference ranged from -23.4% to -3.2% for all tumour sizes and tumour-liver distances (Appendix F, Table F-1). As shown in Figure 4-2, tumour I showed a decrease in quantification accuracy with increase in tumour-liver distance. The paired two tailed t-test indicated a significant difference ($p < 0.05$) for tumour I between the mean % difference at tumour-liver distances of 0 cm *vs* 6 cm as shown in Figure 4-2 (Appendix E, Table E-4). There was no significant difference ($p > 0.05$) in the mean % difference between tumour-liver distances of 3 cm *vs* 6 cm. The other tumours (II, III and IV) showed no significant difference ($p > 0.05$) in mean % difference as function of tumour-liver distance for all paired tumour-liver distances.

The largest SD values for Chang correction for each tumour size as a function of tumour-liver distances were 2.4% (tumour I, 0 cm position), 1.9% (tumour II, 6 cm), 3.5% (tumour III, 6 cm) and 2.7% (tumour IV, 6 cm position) (Appendix F, Table F-1).

SPECT activity quantification using the TEW-CT correction

In Figure 4-2, the mean % difference for TEW-CT ranged from -1.8% to 8.4% for all tumour sizes and tumour-liver distances (Appendix F, table F-2). The paired two tailed t-test show that there was no significant difference ($p > 0.05$) between 0 cm *vs* 6 cm and 3 cm *vs* 6 cm for all tumour-liver distances and all tumour sizes (tumour I, II, III and IV) (Appendix E, Table E-4). The quantification results also showed that tumour I and II overestimated the true activity values with up to 8.4% and 7.3% respectively. Tumour III shows a slight underestimation (maximum underestimation of 1.8% at 3 cm) of the true

activity value. Tumour IV resulted in overestimation of the true value, namely; 3.9% at a tumour-liver distance of 0 cm as compared to tumour III. This was different from what is observed in literature where the largest tumour usually results in the most accurate quantification value in the absence of PVE correction.

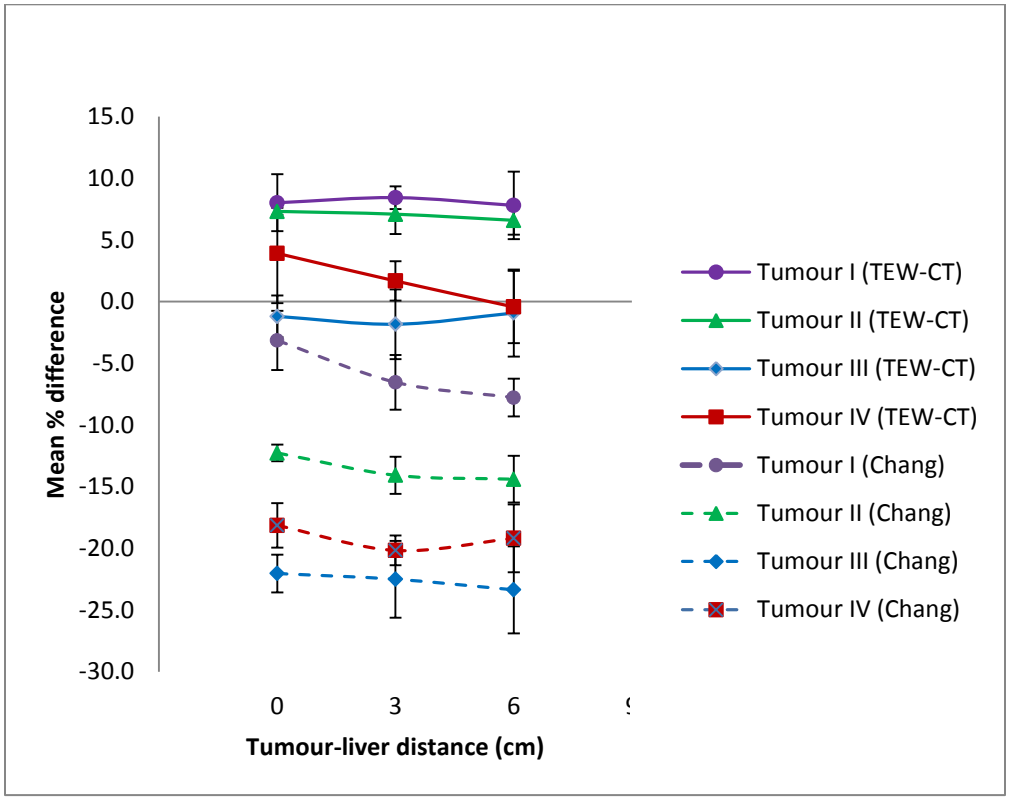

***Figure 4-2**: The mean percentage difference between the quantified and true activity as a function of tumour-liver distance for different tumour sizes. The results are shown for Chang and TEW-CT corrections. ROI-R was used to obtain the counts from SPECT reconstructed images.*

In this study, most of the spill-out counts where included in ROI-R as mentioned previously in chapter 3, that resulted in the overestimation of true activity for the large tumours. The unpaired two tailed t-test indicated no significant differences ($p > 0.05$) in mean % differences as function of tumour size between tumour I *vs* II and tumour III *vs* IV at all tumour-liver distances (Appendix E, Table E-5).

As for the difference in the mean % difference between tumour II and III, there was significant difference ($p < 0.05$) as a function of tumour size for the two tumour-liver distances (0 cm and 3 cm). However, at tumour-liver of 6 cm for tumour II *vs* III there was no significant difference ($p > 0.05$). The smaller range of the mean % difference obtained for the TEW-CT method indicated that the quantification dependence on tumour size was less for the TEW-CT correction method than for the Chang correction method (10.2% *vs* 20.2% Appendix F, Table F-1 and F-2). The largest SD associated with the mean % difference (Figure 4-2) as function of tumour-liver distances were 2.7% (tumour I, 6 cm position), 1.6% (tumour II, 3 cm), 3.5% (tumour III, 6 cm) and 4.0% (tumour IV, 0 cm position) (Appendix F, Table F-2).

4.5.3.3 Influence of Flash 3D reconstruction parameters on quantification

The results for the Flash 3D reconstruction parameters are shown in Figure 4-3(A) and (B) for tumour II and IV respectively. Convergence for tumour II (Appendix F, table F-3) was attained at 128 MLEM iterations at all the different tumour-liver positions. A similar convergence pattern was noticed for tumour IV (Appendix F, table F-4) for all tumour-liver distances.

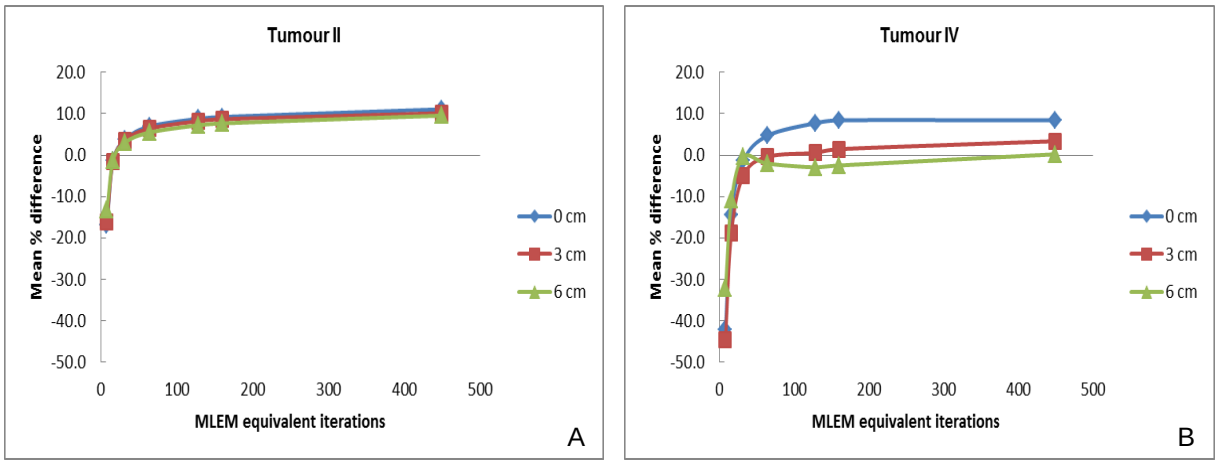

***Figure 4-3**: The mean % difference between the quantified and true activity values as a function of MLEM equivalent iterations at different tumour-liver distances. No background was added to the Abdominal Phantom for (A) Tumour II and (B) Tumour IV.*

4.6 Discussion

4.6.1 Attenuation coefficient values obtained from the CT images

The results shown (Table 4-5) for the % differences obtained between the measured and theoretical attenuation coefficient values for ^{123}I are consistent with those in section 3.6.1 for ^{99m}Tc. The measured attenuation coefficient values for Polystyrene were overestimating the theoretical values and showed a large mean % difference value (65%). This large mean % difference was caused by the density differences between the Polystyrene used in this study and that used by Hubbell, (1982) for the theoretical calculation of the attenuation coefficient values. The other materials used to determine the CT attenuation coefficient values had mean % difference values of less than 1.5 %. This implied that the transformation of Hounsfield units to the appropriate attenuation coefficient values for ^{123}I were accurate.

4.6.2 SPECT calibration factor

It was shown in chapter 3 section 3.6.2.2 that a single SPECT calibration factor value could be used due to the stability of the gamma camera. A calibration factor of 10.8 cpm/kBq was used for all the measurements done with ^{123}I.

4.6.3 SPECT quantification for different tumour sizes and locations

4.6.3.1 Influence of scatter and attenuation corrections on SPECT quantification

The Chang correction for the different tumour sizes resulted in mean % differences that ranged from -23.4% to -3.2%. It is evident from the results that tumour size plays an important role during SPECT quantification when using the Chang correction. This underestimation of the quantified activity was consistent with the results obtained by Soret et al., (2003) in a ^{123}I quantitative brain study when no scatter correction was applied to the data.

The quantification accuracy (Figure 4-2) for all tumour sizes and tumour-liver distances ranged from -1.8% to 8.4% when the TEW-CT correction method was applied. The quantification accuracy recorded in this study was consistent with the phantom studies done by Shcherbinin et al., (2012), Zeintl et al, (2010) and Willowson et al., (2008) using different radionuclide, with scatter and attenuation corrections applied to their data. The comparison between the mean % difference of our study and these studies confirms that the SPECT protocol employed to determine the quantification accuracy is valid.

The advantage of applying the TEW-CT correction was demonstrated. The use of the TEW-CT correction instead of the Chang correction during reconstruction of the SPECT data decreased the range of the mean % difference (-23.4% to -3.2% vs -1.8% to 8.4%) for all the different tumour sizes. The quantification accuracy results obtained with the TEW-CT and Chang corrections are consistent with the results obtained by Soret et al.,(2003) in a brain phantom study done with ^{123}I. As mentioned previously in section 3.7.3.1, in our study the effect of spill-out counts was partially compensated for by using ROI-R.

4.6.3.2 Effects of Flash 3D reconstruction parameters on quantification

The effect of varying Flash 3D reconstruction parameters (number of MLEM equivalent iterations) was shown (Figure 4-3). As mentioned in section 2.5.1.2, Tsui et al., (1994) and Meikle et al., (1994) have shown that stopping rules are not entirely obvious. In these studies the authors showed that the mean square error used provided inconclusive stopping points for different tumour sizes while their signal to noise ratio approach required modifications as a stopping criterion. The results of our study indicated that the use of 128 MLEM equivalent iterations used in this study achieved consistent results for both tumour sizes. However, as demonstrated by Liow and Strother, (1993) the convergence of a smaller object was slow and reported that the stopping rules lead to unknown object dependent precision and accuracy trade-offs. The difference in object size used in this study (2.7 cm and 4.3 cm diameter) as compared to the object size (0.5 cm to 2.5 cm diameter) used by Liow and Strother, (1993) may have played a role in the convergence rate of our two tumour sizes being the same.

The main focus of the study was to determine the SPECT quantification accuracy. The SPECT data were obtained as function of tumour size and tumour-liver distance, in close proximity to an organ with high activity uptake. It was shown (section 3.4.4 and 3.5.2.) in this study that the type of ROI and the selected imaging matrix size have an influence on the accuracy of SPECT quantification. The partial volume effect was partially corrected for by drawing a ROI-R which includes most of the image counts. This ROI which included most of the spill-out counts is not ideal when background activity and an organ with high activity uptake are in close proximity of the tumour. The inconsistency in the reproducibility of the tumours, due to their orientation inside the phantom, was a limiting factor in this study. The inconsistent alignment of tumours during different SPECT acquisitions resulted in different size ROIs used for the different studies. In spite of these limitations, this study has reasonably shown that acceptable

SPECT quantification accuracy can be achieved with ^{123}I when a systematic approach of basic corrections is applied to the SPECT data.

4.7 Conclusion

The accuracy of attenuation coefficient values for the different materials used in this study was found to be good except for polystyrene which resulted in large errors. The cause for these large errors was the variable density of commercially available Polystyrene. In this study we found that the use of the TEW-CT correction improved the quantification accuracy of ^{123}I SPECT when compared to the results obtained with the Chang correction. The study also supports the idea that the tumour size played an important role in SPECT quantification accuracy. Lastly the study showed that Flash-3D reconstruction parameters used in this study were independent on the tumour size.

4.8 References

density of expanded polystyrene [WWW Document], n.d. . Expanded Polystyrene (EPS) Thermal installa tions. URL http://www.thermalinstallations.com.au/images DB/wysiwyg/TDS_Expanded_Polystyrene.pdf (accessed 11.11.14).

Edwards, K., Zhuang, H., 2014. Medium energy general purpose collimators (MEGP) are superior over low energy high resolution (LEHR) collimators for I123 imaging. J NUCL MED MEETING ABSTRACTS 55, 2622.

Hubbell, J.H., 1982. Photon mass attenuation and energy-absorption coefficients. The International Journal of Applied Radiation and Isotopes 33, 1269–1290.

IAEA, 2006. Technical reports series no. 454: Quality Assurance for Radioactivity Measurement in Nuclear Medicine.

IAEA, 2008. Clinical Applications of SPECT/CT: New Hybrid Nuclear Medicine Imaging System (IAEA-TECDOC-1597). Vienna, Austria.

Liow, J.S., Strother, S.C., 1993. The convergence of object dependent resolution in maximum likelihood based tomographic image reconstruction. Phys Med Biol 38, 55–70.

Meikle, S.R., Hutton, B.F., Bailey, D.L., Hooper, P.K., Fulham, M.J., 1994. Accelerated EM reconstruction in total-body PET: potential for improving tumour detectability. Phys Med Biol 39, 1689–1704.

Moore, C., Barrington, M., DeLoatch, N., Farrow, J., 2012. Improving image quality for I-123 whole body images using medium-energy vs. low-energy collimators. Society of Nuclear Medicine Annual Meeting Abstracts 53, 2738.

Ogawa, K., Harata, Y., Ichihara, T., Kubo, A., Hashimoto, S., 1991. A practical method for position-dependent Compton-scatter correction in single photon emission CT. IEEE Trans Med Imaging 10, 408–412.

Shcherbinin, S., Piwowarska-Bilska, H., Celler, A., Birkenfeld, B., 2012. Quantitative SPECT/CT reconstruction for ^{177}Lu and ^{177}Lu/^{90}Y targeted radionuclide therapies. Physics in Medicine and Biology 57, 5733–5747.

Snay, E.R., Treves, S.T., Fahey, F.H., 2011. Improved quality of pediatric 123I-MIBG images with medium-energy collimators. J Nucl Med Technol 39, 100–104.

Soret, M., Koulibaly, P.M., Darcourt, J., Hapdey, S., Buvat, I., 2003. Quantitative accuracy of dopaminergic neurotransmission imaging with (123)I SPECT. J. Nucl. Med. 44, 1184–1193.

Tsui, B.M., Frey, E.C., Zhao, X., Lalush, D.S., Johnston, R.E., McCartney, W.H., 1994. The importance and implementation of accurate 3D compensation methods for quantitative SPECT. Phys Med Biol 39, 509–530.

Willowson, K., Bailey, D.L., Baldock, C., 2008. Quantitative SPECT reconstruction using CT-derived corrections. Physics in Medicine and Biology 53, 3099–3112.

Zeintl, J., Vija, A.H., Yahil, A., Hornegger, J., Kuwert, T., 2010. Quantitative Accuracy of Clinical 99mTc SPECT/CT Using Ordered-Subset Expectation Maximization with 3-Dimensional Resolution Recovery, Attenuation, and Scatter Correction. J Nucl Med 51, 921–928.

Chapter 5

Conclusion

CHAPTER 5 5-1

5.1 INTRODUCTION 5-2
5.2 ABDOMINAL PHANTOM DESIGN 5-2
5.3 CT ATTENUATION COEFFICIENTS VERIFICATION 5-2
5.4 QUANTIFICATION OF ^{99M}TC 5-3
5.4.1 Isotope calibrator 5-3
5.4.2 SPECT calibration factor 5-3
5.4.3 SPECT data processing and quantification 5-3
5.5 QUANTIFICATION OF ^{123}I 5-4
5.6 RECOMMENDATION FOR FUTURE RESEARCH 5-5

5.1 Introduction

The overall aim of this study was to evaluate the influence of the geometry of a radionuclide distribution on SPECT quantification accuracy for ^{99m}Tc and ^{123}I isotopes in an Abdominal Phantom. Accurate quantification of SPECT studies is essential in the dose calculation for treatment of certain tumours and to ascertain the treatment response after therapy. The study sought to determine the SPECT quantification accuracy for ^{123}I in an in-house build Abdominal Phantom for the SPECT/CT system in the NM department. In this study the SPECT acquisition and processing were first established for ^{99m}Tc and then applied to ^{123}I data. The objectives used to fulfil the aim were in brief; the design of an Abdominal Phantom, verification of the accuracy of CT attenuation coefficient values, determination of the isotope calibrator accuracy and to obtain a SPECT calibration factor. The influence of scatter correction, tumour size and tumour location relative to a high uptake organ liver on quantification accuracy of SPECT studies was also assessed. Finally, the investigation of the selected OSEM parameters influence on quantification protocol.

5.2 Abdominal Phantom design

A fully functional Abdominal Phantom was designed and manufactured to assess the quantification accuracy of the different tumour sizes and tumour positions.

5.3 CT attenuation coefficients verification

The CT attenuation coefficients values of five different compounds were measured and compared to the theoretical values for the energies of ^{99m}Tc and ^{123}I respectively. The accuracy of the measured CT attenuation coefficient values were acceptable for both radionuclides energies, except for Polystyrene. This gave confidence about the application of the attenuation map applied during the reconstruction of the SPECT data.

5.4 Quantification of ^{99m}Tc

5.4.1 Isotope calibrator

The accuracy of the isotope calibrator used in this study was a prerequisite for determining a SPECT calibration factor and for quantification accuracy of SPECT studies. The isotope calibrator accuracy was found to be within the acceptable limits for all the radionuclides used in this study.

5.4.2 SPECT calibration factor

The conversion of SPECT image counts to absolute activity values was done by using a single value for the SPECT calibration factor. A single value for the SPECT calibration factor was used during this study because it was shown that the calibration factor was reproducible with small variations during the different experimental measurements.

5.4.3 SPECT data processing and quantification

It was found that the use of a 256 matrix size had better quantification accuracy than a 128 matrix size. However, due to the presence of low count statistics in a clinical environment the 128 matrix size is the matrix size of choice for clinical studies.

The ROI-R was adopted throughout the study as the ROI of choice. The main advantage of ROI-R was that most of the spill-out counts or activity was recovered and therefore compensating for the loss of image counts due to the PVE.

The influence of DEW-CT and TEW-CT scatter and attenuation corrections on the accuracy of SPECT quantification was clear from the results. The SPECT quantification accuracy obtained with these corrections were better than with the Chang correction which confirms the results from the literature.

The size of the tumour played a role in determining the quantification accuracy that can be achieved whether using the DEW-CT correction or the Chang correction. The large tumours i.e. greater than 3 times FWHM of the point spread function produce better quantification accuracy than the smaller tumours that are less than 3 times FWHM. The study showed no significant difference in the quantified value was obtained when the tumour-liver distance was varied for all tumours, when the DEW-CT correction was applied to the ^{99m}Tc SPECT data.

The influence of Flash-3D reconstruction parameters on quantification indicated that slight difference in convergence for different tumour sizes and in the presence of background. The benefit being that the same reconstruction parameters can be used for a given tumour size at all tumour distance relative to an organ of high activity uptake. The results indicated that even when the different reconstruction parameters were used, good accuracy was attained provided that a sufficient number of iterations were used.

5.5 Quantification of ^{123}I

The ^{123}I quantification accuracy of different tumour sizes and tumour-liver distances were similar to those attained with ^{99m}Tc. The TEW-CT correction method improved quantification accuracy as compared to the Chang correction. The quantification accuracy was not influenced by the tumour-liver distance, but was influenced by tumour size when TEW-CT correction was applied during reconstruction with Flash 3D. The convergence the Flash 3D when different reconstruction parameters were used, was attained at the 128 MLEM equivalent iterations for both tumours used.

There was a difference in the convergence of tumour II with ^{99m}Tc and to that with ^{123}I.

5.6 Recommendation for future research

It is recommended that more realistic human phantoms with more organ inserts to mimic the real patients be used for future studies. The use of the measured recovery coefficients or model based recovery coefficients needs to be included to correct for PVE. The problem of ROI definition is an ongoing problem in SPECT quantification. Monte Carlo simulations can also be used to investigate some of the above problems associated with the SPECT quantification measurements.

The general overestimation that was observed in the ^{99m}Tc and ^{123}I quantified activity values indicated that the scatter correction techniques (DEW and TEW) should be optimised further. However, quantification accuracy results for both isotopes were comparable to literature values. This study showed that the quantification protocol for ^{99m}Tc and ^{123}I SPECT can be used with confidence in the NM department at Universitas Hospital.

Abstract

A review of Single Photon Emission Tomography (SPECT) quantification shows that different protocols and phantoms are available to evaluate SPECT quantification accuracy. This study was necessitated by the lack of standardized protocols and the widespread use of a variety of non-standard phantoms. The aim of this work was to evaluate the influence of the geometry of a radionuclide distribution on SPECT quantification accuracy for ^{99m}Tc and ^{123}I isotopes in an abdominal phantom. In order to achieve the aim, the following steps were taken: The preparatory phase of the study was to design and construct an abdominal phantom, verify the accuracy of the attenuation coefficients obtained with the Computed Tomography (CT) scanner, determine the accuracy of the source calibrator used in this study and then obtain a calibration factor in order to convert image counts to activity. During the quantification phase SPECT data were acquired, the influence of not applying scatter correction explicitly was evaluated and the final quantification was performed using the proposed standard clinical reconstruction protocols. The influence of different tumour sizes and locations in the abdominal phantom relative to a high uptake organ on the quantification accuracy was evaluated. Finally, parameters in the Ordered Subset Expectation Maximization (OSEM) reconstruction protocol were altered in order to investigate the influence of number of subsets and iterations on the quantified data.

The non-standard Density Phantom with five different compounds was used for the verification of the ^{99m}Tc and ^{123}I attenuation coefficients. The percentage difference between the measured and theoretical attenuation coefficients values were < 3%, except for Polystyrene (85% and 65% respectively). The SPECT calibration factor was determined for both ^{99m}Tc (11.0 ± 1.3 cpm/kBq) and ^{123}I (10.8 ± 0.3 cpm/kBq) using the Cylindrical Phantom. The in-house built Abdominal Phantom was used to evaluate the tumour activity quantification accuracy. The quantification accuracy of ^{99m}Tc and ^{123}I was found to change significantly ($p < 0.05$) as a function of tumour size after corrections for “spill out” counts due to the partial volume effect, scatter and attenuation

were applied. On the other hand, there was no significant difference in the quantification accuracy ($p > 0.05$) for each tumour at different tumour-liver distances when appropriate scatter and attenuation corrections were applied. The influence of OSEM parameters showed no dependence on the tumour-liver distance and no significant difference ($p > 0.05$) between quantification with background activity as compared to no background activity.

In conclusion, the study showed that the quantification accuracy for ^{99m}Tc and ^{123}I was comparable to other published studies. It was found that the tumour quantification accuracy is not influenced by proximity of high uptake organs when appropriate correction factors were applied. Tumour size influenced the accuracy of SPECT quantification for both radionuclides. The results of this study also showed that at least 128 Maximum Likelihood Expectation Maximization (MLEM) equivalent iterations were needed during iterative reconstruction to achieve convergence and consistent SPECT quantification accuracy. Finally, it is recommended that the evaluated quantification protocol may be used in our nuclear medicine clinic for ^{99m}Tc and ^{123}I quantification.

Keywords: Computed Tomography, Single Photon Emission Computed Tomography, Quantification, Ordered Subset Expectation Maximisation.

Opsomming

‘n Oorsig van Gerekenariseerde Enkel Foton Emissie Tomografie (GEFET) kwantifisering wys dat verskillende protokolle en fantome beskikbaar is om die akkuraatheid van GEFET kwantifisering mee te evalueer. Hierdie studie was genoodsaak deur ‘n tekort aan gestandardiseerde protokolle en die algemene gebruik van ‘n verskeidenheid van nie-standaard fantome. Die doel van hierdie studie was om die invloed van die geometrie van radionuklied verspreiding vir GEFET kwantifisering akkuraatheid te evalueer vir ^{99m}Tc en ^{123}I radionukliede in ‘n abdominale fantoom. Om hierdie doel te bereik is die volgende stappe gevolg: Die voorbereidingsfase van hierdie studie was die ontwerp en konstruksie van ‘n abdominale fantoom, die verifiëring van die akkuraatheid van die attenuasie koeffisiënte wat verkry is met ‘n Rekenaar Tomografie skandeerder, bepaling van die akkuraatheid van die bronkalibreerder wat in hierdie studie gebruik is en die verkryging van ‘n kalibrasiefaktor om beeldtellings om te skakel na aktiwiteit. Gedurende die kwantifiseringsfase is GEFET data versamel, die uitwerking van geen verstrooiïngskorreksie was geëvalueer en die finale kwantifisering was uitgevoer deur gebruik te maak van die voorgestelde standaard kliniese rekonstruksie protokolle. Die invloed van verskillende tumor groottes en posisies in die abdominale fantoom relatief tot ‘n orgaan met hoë radioaktiewe opname op die akkuraatheid van die kwantifisering was ook geëvalueer. Laastens was parameters in die OSEM (“Ordered Subset Expectation Maximization”) rekonstruksie protokol verander om die invloed van verskillende aantal substelle en iterasies op die gekwantifiseerde data te ondersoek.

Die nie-standaard Digtheid Fantoom met vyf verskillende digtheid samestellings was gebruik vir die verifikasie van die ^{99m}Tc en ^{123}I attenuasie koeffisiënte. Die persentasie verskille tussen die gemete en teoretiese attenuasie koeffisiënt waardes was < 3%, behalwe vir Polystyrene (85% en 65% onderskeidelik). Die GEFET kalibrasie faktor was bepaal vir beide ^{99m}Tc (11.0 ± 1.3 cpm/kBq) en ^{123}I (10.8 ± 0.3 cpm/kBq) deur die

Silindriese Fantoom te gebruik. Die inhuis vervaardigde Abdominale Fantoom was gebruik om die akkuraatheid van die tumor aktiwiteit kwantifisering te evalueer. Die kwantifiseringsakkuraatheid van ^{99m}Tc en ^{123}I het betekenisvol verskil ($p < 0.05$) as ‘n funksie van tumor grootte na die korreksies vir “misplaasde” tellings as gevolg van die parsiële volume effek, , verstrooiïng en attenuasie aangebring is. Daarteenoor was daar geen betekenisvolle verskil in die kwantifiseringsakkuraatheid ($p > 0.05$) vir elke tumor by die verskillende tumor-lewer afstande wanneer die gepaste verstrooiing en attenuasie korreksies toegepas was nie. Die invloed van OSEM parameters het geen afhanklikheid van tumor-lewer afstande getoon nie en geen betekenisvolle verskil ($p > 0.05$) tussen kwantifisering met agtergrond aktiwiteit in vergelyking met geen agtergrond aktiwiteit nie.

Ter samevatting het hierdie studie aangetoon dat die kwantifiseringsakkuraatheid vir ^{99m}Tc en ^{123}I vergelykbaar was met ander gepubliseerde studies. Dit is gevind dat tumor kwantifiseringsakkuraatheid nie beïnvloed word deur die nabyheid van hoë opname organe nie, mits die nodige korreksie faktore toegepas word. Tumor grootte beïnvloed die akkuraatheid van GEFET kwantifisering vir beide radionukliede. Die resultate van hierdie studie het ook aangetoon dat ten minste 128 MLEM (“Maximum Likelihood Expectation Maximization”) ekwivalente iterasies nodig was gedurende iteratiewe rekonstruksie om konvergensie en bestendige GEFET kwantifisering akkuraatheid te behaal. Laastens word dit aanbeveel dat die geëvalueerde kwantifiseringsprotokol gebruik mag word in ons kerngeneeskunde kliniek vir ^{99m}Tc en^{123}I GEFET kwantifisering.

Sleutelwoorde: Rekenaar Tomografie, Gerekenariseerde Enkel Foton Emissie Tomografie, Kwantifisering, "Ordered Subset Expectation Maximisation".

Glossary

ADC: Analogue to Digital Converter

CDR: Collimator Detector Response

CT: Computed Tomography

DEW: Dual Energy Window

DEW-CT: Dual Energy Window scatter correction and narrow beam attenuation correction method

FBP: Filtered Back Projection

FWHM: Full Width at Half Maximum

LEHR: Low Energy High Resolution

MEGP: Medium Energy General Purpose

MLEM: Maximum Likelihood Expectation Maximization

MSE: Mean Square Error

NM: Nuclear Medicine

OSEM: Ordered Subset Expectation Maximum.

PMT: Photomultiplier Tube

PVE: Partial Volume Effect

RC: Recovery Coefficient

ROI: Region of Interest

SPECT: Single Photon Emission Computed Tomography

TEW: Triple Energy Window

TEW-CT: Triple Energy Window scatter correction and narrow beam attenuation correction method

VOI: Volume of Interest

Appendix A

Siemens Symbia gamma camera uniformity results performed according to NEMA standards. The uniformity was acquired with 40 million counts, count rate: 20 kcounts/sec, matrix size 1024 x 1024. Results are related to section 3.4.1.

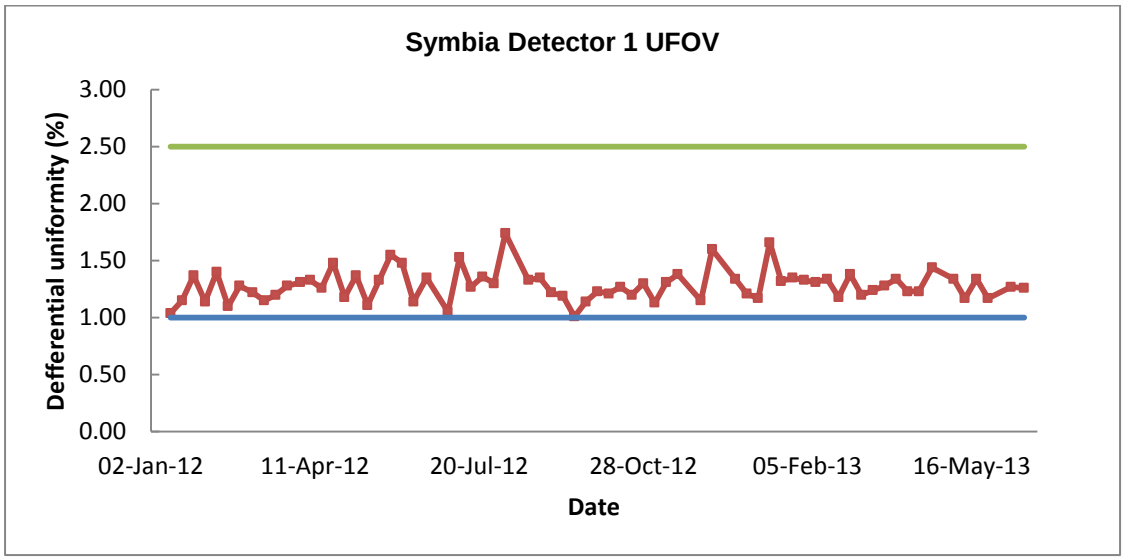

Figure A-1: *Differential uniformity for the Symbia gamma camera detector 1.*

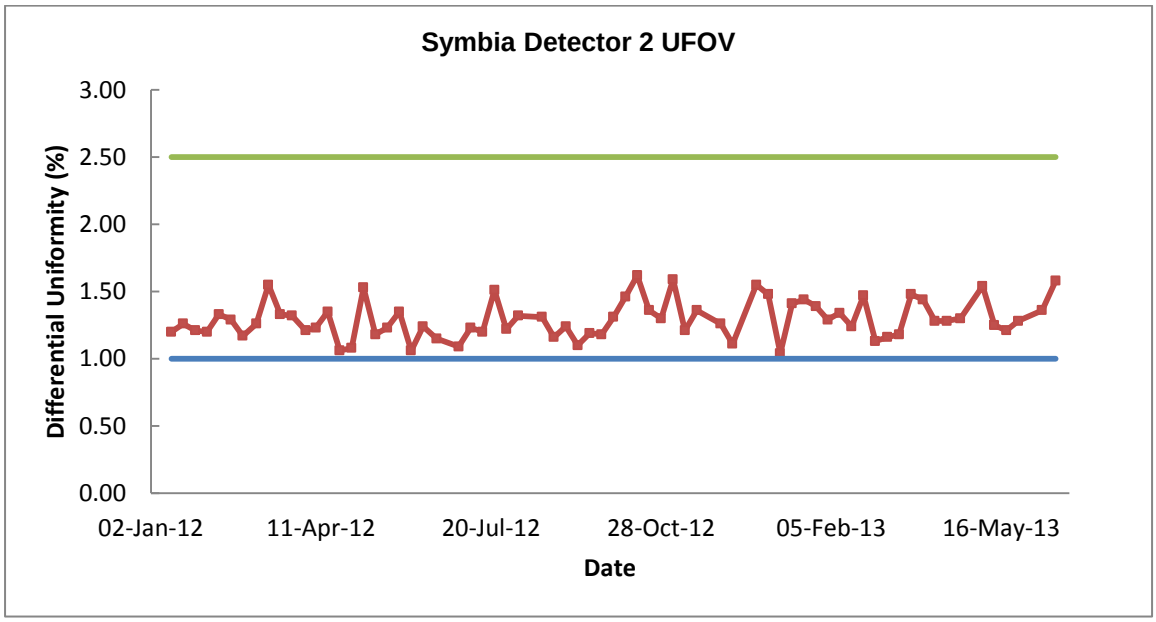

Figure A-2: *Differential uniformity for the Symbia gamma camera detector 2.*

Appendix B

Poster presentation results for isotope calibrator accuracy related to section 3.4.2.1 and 4.3.2. The poster was presented at faculty health science forum of the University of the Free State, 2011.

Intercomparison of Nuclear Medicine Isotope Calibrators in Bloemfontein Area.

Mongane M, Boom K, van Staden J, du Raan H
Department of Medical Physics, University of the Free State, Bloemfontein

Introduction

Isotope calibrator (figure 3) is widely used to measure the activity of radiopharmaceuticals for administration to nuclear medicine patients for diagnostic or therapeutic purposes. The determination of the accuracy of the dose calibrator is essential for correct radioactivity measurement to avoid giving the incorrect radiation dose to patients. It also plays a vital role in accurate quantitation of radioactive uptake and thus radiation dosimetry. Routinely used radioisotopes in nuclear medicine namely: Tc-99m, Ga-67, I-123 and I-131 were used for intercomparison of isotope calibrators.

Material and Methods

The accuracy of seven dose calibrators (Five Capintec CRC-15R and two Capintec 10W) in Bloemfontein hospitals were evaluated using 4 different radionuclides. The radionuclides used were standard solutions of I-131, I-123, Ga-67 and Tc-99m. On one source calibrator only I-131 measurement were obtained. The radionuclides were placed in standard flame sealed ampoules after the mass of each solution had been determined. All measurements were repeated five times. The samples were sent for traceable calibration to NMISA in Cape Town. The NMISA results were compared with the measurements obtained using the isotope calibrators in the hospitals. This procedure is expensive and cannot be easily repeated, instead a moderately long half life radioisotope Cs-137 was used to evaluate the long term stability and reproducibility of the isotope calibrators.

Results

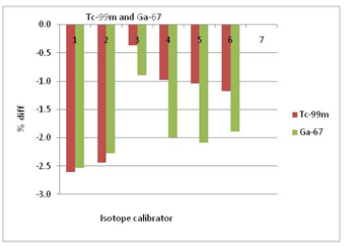

Fig 1: results for Tc-99m and Ga-67 from different isotope calibrators.

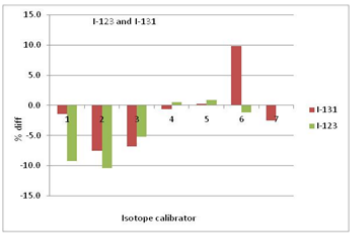

Fig 2: results for I-123 and I-131 from different isotope calibrators.

Most isotope calibrators are underestimating the calibrated activity for all four radionuclides (fig 1 & 2). The maximum percentage differences were as follows: I-131 (9.8%), I-123 (– 10.4%), Ga-67 (– 2.5%) and Tc-99m (– 2.6%). In particular isotope calibrator no. 1 and 2 gave highest % difference for I-123, and the calibrator no. 6 for I-131. These were communicated through to the nuclear medicine department concerned for further investigations. According to IAEA TECDOC differences of +/-10% are acceptable for diagnostic imaging as well as for therapeutic purposes. If isotope calibrator measurements are to be used for dosimetry purposes, corrections should be applied to correct for these discrepancies. The reproducibility on all seven calibrators was acceptable. The largest percentage standard deviation on 5 measurements was 1.3% for isotope calibrator no. 7.

Conclusion

Six isotope calibrators in the hospitals were found to be within 10% of the measured activity at the calibration laboratories and only one was above the limit. This cross calibration against a standards laboratory gives us confidence in all the isotope activity measurements done in the Bloemfontein area, and allows meaningful quantitative dosimetry. Continued quality control should be carried out on all the calibrators using all appropriate radionuclide settings with a standard, moderately long half life, source (i.e. Cs-137) to ensure long term stability of the accuracy of the radioactivity measurements.

References

1. IAEA International Atomic Energy Agency, Quality Control of Nuclear Medicine Instruments, IAEA-TECDOC-602, Vienna,1991

Acknowledgements

We would like to acknowledge the staff of the Departments of Nuclear Medicine in the Bloemfontein area for their assistance. In this study.

Fig 3: Capintec isotope calibrator used in nuclear medicine (Capintec Inc. Pittsburgh, USA).

Departement Mediese Fisika • Department Medical Physics
UNIVERSITEIT VAN DIE VRYSTAAT • UNIVERSITY OF THE FREE STATE • YUNIVESITHI YA FREISTATA
Tel (051) 405 3156 • E-mail: MonganeMS@ufs.ac.za • www.ufs.ac.za

Appendix C

Capintec Isotope calibrator constancy results with ^{137}Cs reference source for ^{99m}Tc and ^{123}I settings respectively. Results are related to section 3.4.2.1 and 4.3.2.

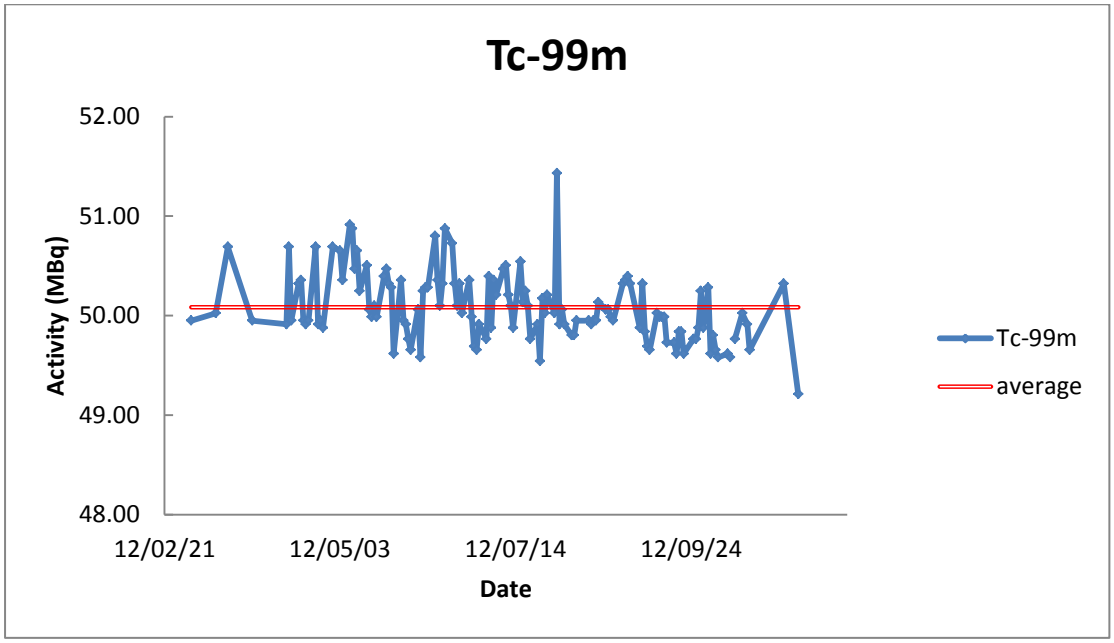

***Figure 3**: Isotope calibrator constancy check results with ^{137}Cs reference source for ^{99m}Tc setting.*

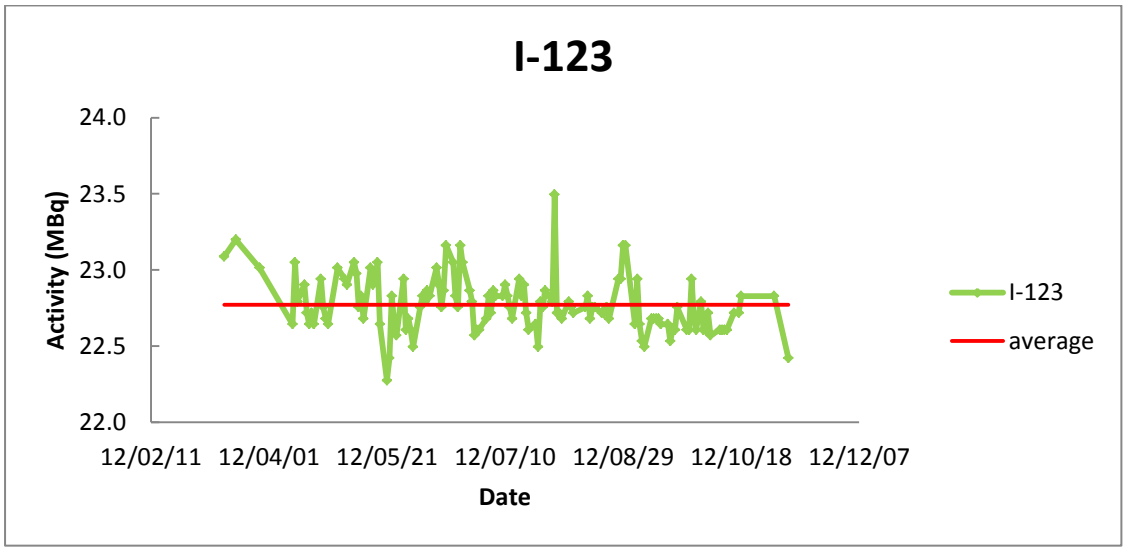

***Figure 4**: Isotope calibrator constancy check results with ^{137}Cs reference source for ^{123}I setting.*

Appendix D : Results for ^{99m}Tc quantification accuracy related to section 3.6.3.

Table D-1*: Mean % difference and associated SD obtained using ROI-R as a function of tumour size and tumour-liver distance of the SPECT data reconstructed using Flash 3D reconstruction and Chang correction. Three data sets were used for each tumour size and tumour-liver distance.*

Tumour-liver distance (cm)	0	3	6
Tumour I	-14.3 ± 1.9%	-14.9 ± 1.4%	-16.5 ± 0.7%
Tumour II	-20.1 ± 1.0%	-22.4 ± 1.5%	-22.8 ± 0.8%
Tumour III	-25.3 ± 0.6%	-27.0 ± 3.4%	-26.1 ± 1.5%
Tumour IV	-30.7 ± 0.3%	-29.4 ± 0.1%	-30.5 ± 0.6%

Table D-2: *Mean % difference and associated SD obtained using ROI-R as a function of tumour size and tumour-liver distance of the SPECT data reconstructed using Flash 3D reconstruction and DEW-CT correction. Three data sets were used for each tumour size and tumour-liver distance.*

Tumour-liver distance (cm)	0	3	6
Tumour I	9.0 ± 0.9%	9.1 ± 1.3%	9.4 ± 0.8%
Tumour II	5.9 ± 2.0%	5.2 ± 1.8%	5.3 ± 0.8%
Tumour III	0.1 ± 1.8%	-0.1 ± 1.1%	0.0 ± 1.8%
Tumour IV	-3.1 ± 2.1%	-0.6 ± 0.7%	-0.3 ± 0.6%

Table D-3*: Mean % difference and associated SD obtained using ROI-C as a function of tumour size and tumour-liver distance of the SPECT data reconstructed using Flash 3D reconstruction and DEW-CT correction. Three data sets were used for each tumour size and tumour-liver distance.*

Tumour-liver distance (cm)	0	3	6
Tumour I	2.5 ± 1.8%	3.9 ± 1.8%	3.0 ± 1.2%
Tumour II	-3.3 ± 1.4%	-3.1 ± 1.5%	-2.4 ± 2.1%
Tumour III	-13.7 ± 0.5%	-12.5 ± 3.0%	-13.6 ± 2.9%
Tumour IV	-13.8 ± 6.8%	-8.1 ± 2.4%	-10.0 ± 2.7%

***Table D-4**: Influence of matrix size on tumour III activity quantification when the Abdominal Phantom was shifted from 0 cm to 2 cm relative to the gamma camera detectors. ROI-R, Flash 3D and DEW-CT were used.*

Matrix size	**256**		**128**	
Phantom shift position (cm)	0	2	0	2
Decay corrected count rate (cpm)	187228	186828	176513	171132
Svol (cpm/kBq)	11.1	11.1	11.1	11.1
Measured activity image (kBq)	16867	16831	15902	15417
True tumour volume (ml)	23	23	23	23
True activity in tumour (kBq)	17723	17723	17723	17723
% difference between measured and true activity	-4.8%	-5.0%	-10.3%	-13.0%

***Table D-5**: Results of quantification accuracy when two background activities were present in the Abdominal Phantom for tumour II.*

Background activity	**0.5%**		**0.9%**	
Tumour-liver distance (cm)	0	6	0	6
Decay corrected count rate (cpm)	409445	411250	406755	401009
Svol (cpm/kBq)	11.1	11.1	11.1	11.1
Measured activity image (kBq)	36887	37050	36645	36127
True tumour volume (ml)	80	80	80	80
True activity in tumour (kBq)	35076	35076	35076	35076
% difference between measured and true activity	5	6	4	3
Mean % difference	5.3 ± 0.4%	5.1 ± 1.2%	4.1 ± 1.3%	4.2 ± 1.1%

***Table D-6**: Results that show convergence obtained when Flash 3D and DEW-CT correction were used. The differences between two consecutive quantification values (% difference) of the MLEM equivalent iterations for tumour II are shown. ROI-R was used and no background activity was added.*

MLEM equivalent iterations	Tumour-liver distance (cm)		
	0	**3**	**6**
8			
16	9	8	7
32	3	2	2
64	1	1	1
128	1	1	1
160	0	0	0
450	0	0	0

***Table D-7:** Results that show convergence obtained when Flash 3D and DEW-CT correction were used. The differences between two consecutive quantification values (% difference) of the MLEM equivalent iterations for tumour IV are shown. ROI-R was used and no background activity was added.*

MLEM equivalent iterations	Tumour-liver distance (cm)		
	0	**3**	**6**
8			
16	14	11	9
32	5	4	3
64	4	2	2
128	2	2	2
160	0	0	0
450	2	2	1

***Table D-8:** Results that show convergence obtained when Flash 3D and DEW-CT correction were used. The differences between two consecutive quantification values (% difference) of the MLEM equivalent iterations for tumour IV are shown. ROI-R was used and 0.9% background activity was added.*

MLEM equivalent iterations	Tumour-liver distance (cm)	
	0	**6**
8		
16	13	10
32	4	3
64	3	2
128	2	1
160	0	0
450	**1**	**0**

Appendix E Statistical analysis using the t-test for SPECT data.

***Table E-1**: Paired two tailed t-test values for Chang and DEW-CT correction as function tumour-liver distance (^{99m}Tc).*

Correction method	Chang		DEW-CT	
Tumour-liver distance (cm)	0 *vs* 6	3 vs 6	0 *vs* 6	3 vs 6
Tumour size				
Tumour I	0.129	0.192	0.246	0.761
Tumour II	*0.002*	0.370	0.629	0.950
Tumour III	0.249	0.519	0.187	0.748
Tumour IV	0.423	0.275	0.096	0.343

Highlighted and italicized values indicate $p < 0.05$, significant difference.

***Table E-2**: P-values obtained using the unpaired two tailed t-test values for Chang and DEW-CT correction as function tumour size (^{99m}Tc).*

Correction method	Chang			DEW-CT		
Tumour size	I vs II	II vs III	III vs IV	I vs II	II vs III	III vs IV
Tumour-liver distance						
0 cm	0.093	*0.005*	*0.001*	*0.036*	*0.021*	0.069
3 cm	*0.003*	0.121	0.329	*0.036*	*0.022*	0.591
6 cm	*0.001*	*0.045*	*0.022*	*0.004*	*0.020*	0.806

Highlighted and italicized values indicate $p < 0.05$, significant difference.

***Table E-3**: P-values obtained using the paired two tailed t-test values for tumour II. The 0% background activity data used as a reference to compare with 0.5% and 0.9% background activities respectively (^{99m}Tc).*

Background activity	0% *vs* 0.5%	0% *vs* 0.9%
Tumour-liver distance		
0 cm	0.684	0.291
6 cm	0.886	0.250

Highlighted and italicized values indicate $p < 0.05$, significant difference.

***Table E-4**: P-values obtained using the paired two tailed t-test values for Chang and TEW-CT correction as function tumour-liver distance (^{123}I).*

Correction method	**Chang**		**TEW-CT**	
Tumour-liver distance (cm)	0 *vs* 6	3 vs 6	0 *vs* 6	3 *vs* 6
Tumour I	0.018	0.209	0.529	0.728
Tumour II	0.208	0.913	0.184	1.000
Tumour III	0.494	0.136	1.000	0.423
Tumour IV	0.652	0.627	0.268	0.225

Highlighted and italicized values indicate $p < 0.05$, significant difference.

***Table E-5**: P-values obtained using the unpaired two tailed t-test values for Chang and TEW-CT correction as function tumour size (^{123}I).*

Correction method	Chang			TEW-CT		
Tumour size	I *vs* II	II *vs* III	III *vs* IV	I *vs* II	II *vs* III	III *vs* IV
Tumour-liver distance						
0 cm	0.027	0.002	0.046	0.676	0.014	0.141
3 cm	0.004	0.028	0.312	0.348	0.016	0.129
6 cm	0.019	0.034	0.180	0.699	0.078	0.826

Highlighted and italicized values indicate $p < 0.05$, significant difference.

Appendix F Results for ^{123}I quantification accuracy

***Table F-1**: Mean % difference and associated SD obtained using ROI-R as a function of tumour size and tumour-liver distance of the SPECT data reconstructed using Flash 3D reconstruction and Chang correction.*

Tumour-liver distance (cm)	0	3	6
Tumour I	-3.2 ± 2.4%	-6.5 ± 2.2%	-7.8 ± 1.5%
Tumour II	-12.3 ± 0.7%	-14.1 ± 1.5%	-14.4 ± 1.9%
Tumour III	-22.0 ± 1.5%	-22.5 ± 3.1%	-23.4 ± 3.5%
Tumour IV	-18.1 ± 1.8**%**	-20.2 ± 1.2**%**	-19.2 ± 2.7**%**

***Table F-2:** Mean % difference and associated SD obtained using ROI-R as a function of tumour size and tumour-liver distance of the SPECT data reconstructed using Flash 3D reconstruction and TEW-CT correction.*

Tumour-liver position (cm)	0	3	6
Tumour I	8.0 ± 2.3%	8.4 ± 0.9%	7.8 ± 2.7%
Tumour II	7.3 ± 0.3%	7.1 ± 1.6%	6.6 ± 1.2%
Tumour III	-1.2 ± 1.7%	-1.8 ± 2.8%	-0.9 ± 3.5%
Tumour IV	3.9 ± 4.0**%**	1.7 ± 1.6**%**	-0.4 ± 2.9**%**

***Table F-3**: Results that show convergence obtained when Flash 3D and TEW-CT correction were used. The differences between two consecutive quantification values (% difference) of the MLEM equivalent iterations for tumour II are shown. ROI-R was used and no background activity was added.*

MLEM equivalent iterations	Tumour-liver distance (cm)		
	0	3	6
8			
16	15.5	14.6	11.9
32	5.2	5.2	4.4
64	3.1	2.8	2.4
128	1.8	1.8	1.7
160	0.5	0.5	0.5
450	1.8	1.4	1.9

***Table F-4**: Results that show convergence obtained when Flash 3D and TEW-CT correction were used. The differences between two consecutive quantification values (% difference) of the MLEM equivalent iterations for tumour IV are shown. ROI-R was used and no background activity was added.*

MLEM equivalent iterations	**Tumour-liver distance (cm)**		
	0	3	6
8			
16	27.8	25.8	21.4
32	13.0	13.9	10.5
64	6.1	4.6	1.6
128	3.0	0.9	0.9
160	0.7	0.9	0.4
450	0.0	1.9	2.7